






3D Mapping Reveals a Complex and Transient Interstitial Matrix During Murine Kidney Development

Sarah N. Lipp ^{1,2} Kathryn R. Jacobson ³ David S. Hains ⁴
Andrew L. Schwarzer ⁴ and Sarah Calve ^{1,3,5}

Due to the number of contributing authors, the affiliations are listed at the end of this article.

ABSTRACT

Background The extracellular matrix (ECM) is a network of proteins and glycosaminoglycans that provides structural and biochemical cues to cells. In the kidney, the ECM is critical for nephrogenesis; however, the dynamics of ECM composition and how it relates to 3D structure during development is unknown.

Methods Using embryonic day 14.5 (E14.5), E18.5, postnatal day 3 (P3), and adult kidneys, we fractionated proteins based on differential solubilities, performed liquid chromatography–tandem mass spectrometry, and identified changes in ECM protein content (matrisome). Decellularized kidneys were stained for ECM proteins and imaged in 3D using confocal microscopy.

Results We observed an increase in interstitial ECM that connects the stromal mesenchyme to the basement membrane (TNXB, COL6A1, COL6A2, COL6A3) between the embryo and adult, and a transient elevation of interstitial matrix proteins (COL5A2, COL12A1, COL26A1, ELN, EMID1, FBN1, LTBP4, THSD4) at perinatal time points. Basement membrane proteins critical for metanephric induction (FRAS1, FREM2) were highest in abundance in the embryo, whereas proteins necessary for integrity of the glomerular basement membrane (COL4A3, COL4A4, COL4A5, LAMB2) were more abundant in the adult. 3D visualization revealed a complex interstitial matrix that dramatically changed over development, including the perinatal formation of fibrillar structures that appear to support the medullary rays.

Conclusion By correlating 3D ECM spatiotemporal organization with global protein abundance, we revealed novel changes in the interstitial matrix during kidney development. This new information regarding the ECM in developing kidneys offers the potential to inform the design of regenerative scaffolds that can guide nephrogenesis *in vitro*.

JASN 32: 1649–1665, 2021. doi: <https://doi.org/10.1681/ASN.2020081204>

The increasing incidence of ESKD represents a worldwide public-health crisis.¹ Although the preferred treatment of ESKD is transplant, there are long wait times, indicating a critical need for additional organs.¹ Tissue engineers aim to supplement the transplant pool by designing artificial kidneys that use polymer networks to provide an external scaffold for kidney cells.² Current efforts have led to incomplete differentiation *in vitro*.³ Therefore, engineered networks may not provide the same environmental cues as the extracellular matrix (ECM), the native scaffold that integrates disparate cells into a functional kidney.

The ECM is a network of proteins and glycosaminoglycans that influences cellular behavior *via*

biologic and mechanical signaling in developing, homeostatic, and diseased tissues.⁴ ECM in the kidney can be divided into the interstitial matrix and basement membrane (Supplemental Figure 1).⁵ The interstitial matrix is a loose network comprised

Received August 20, 2020; Accepted February 20, 2021.

Published online ahead of print. Publication date available at www.jasn.org.

Correspondence: Prof. Sarah Calve, Paul M. Rady Department of Mechanical Engineering, University of Colorado Boulder, 1111 Engineering Drive, Boulder, CO 80309. Email: sarah.calve@colorado.edu

Copyright © 2021 by the American Society of Nephrology

of fibril-forming ECM, which is found between individual kidney tubules and includes elastin, fibrillins (FBNs), collagens, proteoglycans, and glycoproteins that maintain mechanical integrity and growth-factor sequestration.⁵ The basement membrane, a dense meshwork of macromolecules that directly surrounds the nephron tubules, is critical for kidney development and physiology.^{4,6} Due to the complexity of these networks, little is known regarding how the interstitial and basement membrane matrices are assembled during nephrogenesis, generating a roadblock in implementing the appropriate microstructure and biochemical properties of the native ECM into bioengineered scaffolds.^{2,7}

Traditional analyses of the ECM (e.g., gene expression, Western blotting, immunohistochemistry [IHC], knockout models, human-mutation case studies) only focus on a few proteins within each study. A more comprehensive analysis of ECM proteins, termed the matrisome, can be achieved by proteomics using liquid chromatography–tandem mass spectrometry (LC-MS/MS).⁵ Recently, fractionation techniques were developed to isolate the matrisome using increasingly stringent solutions to solubilize cellular proteins and characterize the matrix in diverse tissues,⁸ including fetal and adult kidneys.^{9–20} Despite these reports, there has yet to be a study that interrogates ECM dynamics across murine embryonic, fetal, and adult kidney development.

In addition to identifying ECM proteins present in the kidney, it is critical to know how these proteins are spatially distributed. Correlating protein-abundance changes with nephron structure in 3D can provide insight into potential roles for different ECM proteins. The recent development of techniques to visualize the ECM of intact tissues has provided information not apparent from 2D sections for visceral organs,^{21–23} including the kidney,^{24–26} and no reports focus on the interstitial matrix at the nephron level. We previously demonstrated that coupling immunofluorescence staining and confocal imaging with decellularization provided new insight into ECM patterning of the embryo²⁷; however, this technique has not been applied to the kidney. In this study, we combined tissue fractionation, LC-MS/MS, and 3D imaging to investigate the ECM in kidneys from the embryo to the homeostatic adult and found that the composition and organization of the interstitial matrix dramatically changed during development. A scaffold tailored to mimic the composition and organization of the developing ECM identified in this study will better guide the engineering of functional kidney tissue.

METHODS

Wild-type C57BL/6 mice were obtained from The Jackson Laboratory. Experimental protocols complied with, and were approved by, either the Purdue Animal Care and Use Committee (PACUC; protocol #1209000723) or the University of Colorado Boulder Institutional Animal Care and Use

Significance Statement

ESKD is increasing in incidence and a limited number of organs are available for transplantation. Therefore, researchers have focused on understanding how cellular signaling influences kidney development to expand strategies to rebuild a kidney. However, the extracellular matrix (ECM), another critical component that biomechanically regulates nephrogenesis, has been largely neglected. Proteomics and 3D imaging of the murine kidney resolved previously undescribed dynamics of the interstitial matrix in the cortex and corticomedullary junction during development. Combined with cells and growth factors, scaffolds modeled after the composition and organization of the developmental ECM have the potential to improve engineered models of the kidney.

Committee (IACUC; #2705). PACUC and IACUC assessed that university researchers and all procedures and facilities are compliant with regulations of the US Department of Agriculture, US Public Health Service, Animal Welfare Act, and Institutional Animal Welfare Assurance. Embryonic day 14.5 (E14.5) to adult kidneys were collected as described in Supplemental Appendix 1.

Proteomics

Tissue Fractionation

Kidneys were isolated from E14.5, E18.5, postnatal day 3 (P3), and male adult (P56) mice. To obtain enough protein for analysis, kidneys from multiple animals and/or litters were pooled for the earlier time points (Supplemental Table 1). Both male and female embryos and pups were used. Proteins from the different cellular compartments were isolated using the protocol developed by the Hynes laboratory, modified for embryonic tissue using solutions of varying detergent and ionic strengths (detailed protocol provided in the Supplemental Appendix 1) following Naba *et al.*²⁸ and Saleh *et al.*,²⁹ and analyzed using MaxQuant.³⁰ The same enrichment method was used for all tissues, and the same mass of tissue was injected (1 µg) for LC-MS/MS. E14.5 kidney data were compared with E14.5 whole-embryo, forelimb, and brain data from Jacobson *et al.*³¹(preprint) These data were from a different LC-MS/MS run, which may limit conclusions from this comparison.

LC-MS/MS Analysis

Protein groups were filtered using Microsoft Excel (2019) to exclude proteins identified by less than two unique and razor peptides, reverse hits, or identified as potential contaminants (with the exception of keratins, THBS1, LUM, TPM2, PFN1, and COMP). Intensities for proteins identified in only one of the three biologic replicates were removed. Proteins were annotated on the basis of matrisome-category and cellular-compartment classifications (Supplemental Tables 1 and 2).^{29,32} Functional characterization of matrisome proteins as “basement membrane,” “interstitial matrix,” and “other” was determined on the basis of Byron *et al.*,⁵ Lennon *et al.*,¹³ and Tsutsui *et al.*,³³(preprint) with additional reannotations made

according to review of histology in the literature for the proteins observed in this study (Supplemental Table 2). For the manual annotations, proteins were defined on the basis of kidney histology or the Immunogold staining pattern in transmission electron microscopy from published literature (Supplemental Table 1). If unavailable, annotations were determined using tissues with a similar morphology and clearly defined epithelial and connective tissue layers (e.g., skin, gastrointestinal tract). Specifically, the text describing the staining, and the staining morphology observed in the figures (e.g., fibers or linear staining indicating enrichment in the interstitial matrix or basement membrane, respectively), were considered when manually annotating the ECM classifications. Although proteins were classified as basement membrane or interstitial matrix on the basis of where they were enriched morphologically, proteins were not necessarily exclusive to these compartments. Proteins were indicated as part of the "elastin-microfibril axis" on the basis of literature studies (Supplemental Figure 1, Supplemental Tables 1 and 2).

The percentage of the matrisome identified in the insoluble (IN) fraction varied over kidney development and between kidney and whole embryo at E14.5. To enable comparison between time points and with E14.5 embryos, "scaled label free quantification (LFQ)" values were used (Jacobson *et al.*³¹(preprint); Equation 1), where i =protein.

$$\text{scaled LFQ}_i = \frac{\text{LFQ}_i}{\left(\sum [\text{LFQ}_{\text{matrisome}}] / \sum [\text{LFQ}_{\text{proteome}}] \right)} \quad (1)$$

GraphPad Prism (version 8.4.2) was used to visualize the data, including manually clustered heatmaps, on the basis of the scaled intensity or z-score (Equation 2), where i =protein, j =sample, and S =SD.

$$z\text{-score}_i = \frac{\text{LFQ}_{ij} - \overline{\text{LFQ}_{ij}}}{S} \quad (2)$$

Gene Ontology (GO) analyses of proteins significantly elevated or exclusive for the IN fraction for the E14.5 kidney versus whole embryo (Supplemental Table 3), or over the kidney time course (Supplemental Table 1), were analyzed using g:profiler.³⁴ The *Mus musculus* and *Homo sapiens* databases were used to ensure complete GO analysis annotations (e.g., laminin 11 was not found in the *M. musculus* database), using a setting of $P < 0.05$. Groupings were modified and redundant terms were removed with REVIGO, using the following setting similarity: medium (0.7), whole UniProt.³⁵ The Venn diagram and figures were compiled using Adobe Illustrator.

When a list of matrisome proteins identified was available, the components in previously published studies of the adult kidney,^{9–12} fetal kidney,¹² adult glomerular tissue,^{13–17} renal artery,¹⁸ and kidney culture models,^{36,37} were compared with this study using a combined human and mouse matrisome list (Supplemental Table 4).³²

Imaging

IHC

IHC was performed using standard methods described in the Supplemental Appendix 1. Antibody sources and dilutions are listed in Supplemental Table 5.

3D Imaging of Decellularized Kidneys

Kidneys were decellularized in low-concentration SDS and imaged using 3D confocal microscopy using protocols modified from Acuna *et al.*,²⁷ as described in the Supplemental Appendix 1. Antibody sources and dilutions are listed in Supplemental Table 5.

SeeDB Clearing of Kidneys

Whole mount–stained kidneys were cleared by equilibrating the tissue in concentrated fructose solutions to increase the refractive index of the medium using a protocol modified from Ke *et al.*,³⁸ as described in the Supplemental Appendix 1. Antibody sources and dilutions are listed in Supplemental Table 5.

Statistical Analyses

Kidney, whole-embryo, and other E14.5 tissue data were collected with $n=3$ biologic replicates and analyzed using Prism (version 8.4.2; GraphPad). The effect of tissue and developmental time was studied using t tests or ANOVA with subsequent Tukey or Sidak multiple comparisons tests or t test. A detailed description is provided in the Supplemental Appendix 1.

RESULTS

Proteomic Analysis Showed Dynamic Changes in Matrisome Composition of the Developing Murine Kidney

To resolve ECM changes during nephrogenesis, E14.5, E18.5, P3, and adult mouse kidneys were sequentially fractionated and analyzed using LC-MS/MS (Figure 1A).^{28,29} Proteins in the cytoskeletal and IN fractions were normalized using LFQ in MaxQuant to allow for comparisons between samples.^{30,39} The matrisome was significantly enriched in the IN fraction and varied on the basis of the developmental time point (Figure 1B, Supplemental Figure 2). Of the 110 ECM proteins identified, 35% were found at all stages, of which 18 were interstitial matrix and 13 were basement membrane proteins (Figure 1C). The 110 matrisome components found *via* LC-MS/MS were similar compared with prior studies, which ranged from 13 to 139 ECM proteins, with a large overlap in specific proteins identified (Supplemental Table 4). Because 63 of 69 of the interstitial matrix and basement membrane proteins identified were either exclusively found in the IN fraction or were at greater intensity compared with the cytoskeletal fraction (Supplemental Table 1, Supplemental Figure 3), the IN fraction was the focus for subsequent analyses.

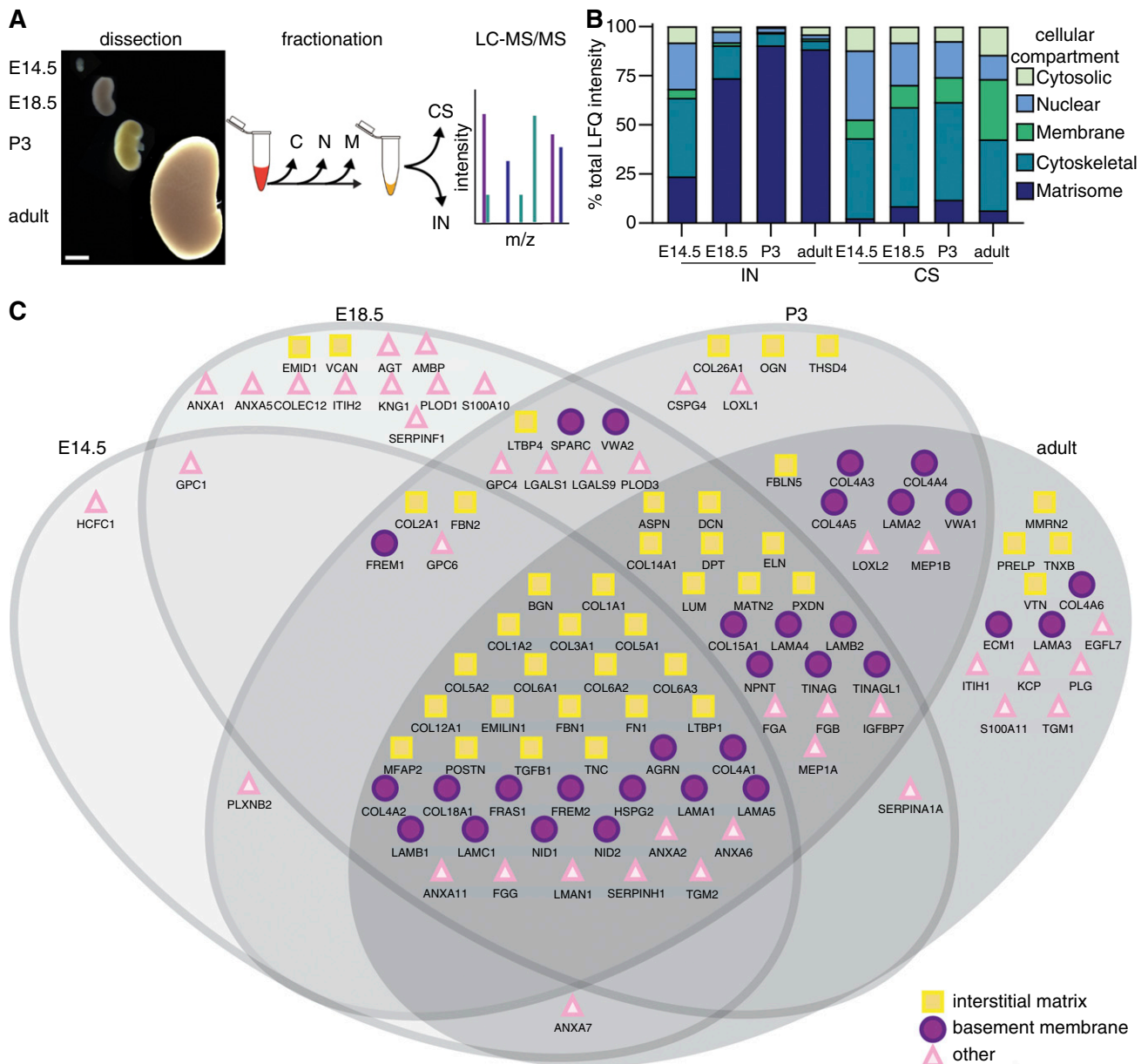


Figure 1. The matrisome of the murine kidney dynamically changed during development. (A) E14.5, E18.5, P3, and adult kidneys were sequentially fractionated in cytosolic (C), nuclear (N), and membrane (M) buffers to isolate the insoluble (IN) and cytoskeletal (CS) fractions. Scale bar, 2 mm. (B) Comparison of total LFQ intensity of different cellular compartments showed the percentage of matrisome significantly varied on the basis of developmental stage and fraction analyzed. Two-way ANOVA indicated developmental stage, fraction, and interaction were significant ($P < 0.001$); Tukey multiple comparisons for IN fraction were significant for all comparisons ($P < 0.001$), except for P3 versus adult. (C) ECM proteins found in CS and IN fractions varied between E14.5 and adult kidneys. Proteins were included if identified in $n \geq 2$ biologic replicates per time point, with $n = 3$ biologic replicates per time point.

The Kidney Basement Membrane Matrisome was Specialized by E14.5

The matrisome of E14.5 kidneys was compared with the whole embryo to assess if the ECM of individual tissues were already distinct by this early time point. A significantly greater amount of basement membrane proteins were found in the kidney, correlating with the unique “basement membrane” GO term (Figure 2, A–C, Supplemental Table 3). Comparing the kidney

with the E14.5 brain and forelimb, the composition of basement membrane proteins was unique to the kidney. The kidney basement membrane was enriched in a Fraser complex protein (FREM1). In contrast, type IV collagen $\alpha 5$ (COL4A5) and COL4A6 were elevated in the brain (Figure 2D), which correlated with COL4A6 localization to the basement membrane of the meninges.⁴⁰ Weak expression of COL4A6 was previously described in the developing Bowman’s capsule basement

membrane^{41–43}; however, it was below the detection level of LC-MS/MS in this study. These differences highlight the specification of the basement membrane proteins in different tissues.

The Composition of Murine Kidney Interstitial Matrix and Basement Membrane Proteins Significantly Changed with Development

To visualize how the relative amounts of interstitial matrix, basement membrane, and ECM-associated proteins changed with development, the proteins were plotted as a z-score heatmap or bar graphs (Figure 3, Supplemental Figures 3–7, Supplemental Table 1). Some proteins decreased with development, including the Fraser complex proteins (FRAS1, FREM2), FN1, FBN2, and type II collagen (COL2A1). There was a general increase in basement membrane components, COL6A1–3, TNXB, and small leucine-rich proteoglycans (SLRPs; ASPN, BGN, DCN, LUM, PRELP, OGN). Interestingly, several interstitial matrix proteins were significantly elevated (COL5A2, COL12A1, FBN1, FBLN5, ELN), trended toward a transient increase (POSTN), or were exclusively found at the perinatal time points (COL26A1, EMID1, LTBP4, THSD4), including components of the elastin-microfibril axis.^{44–46}

Overall, there was a significant decrease in interstitial matrix and a significant increase in basement membrane components over development (Figure 4A). For example, the basement membrane proteins LAMA5 and NID1 were significantly increased at P3 compared with E14.5 (circles, Figure 4B), with an increase in additional basement membrane proteins (COL4A3–5, LAMB2, TINAG) when comparing the adult to P3 (Figure 4C). Notably, at P3, elastin-microfibril axis proteins were enriched compared with the adult (green text).

GO Analysis and IHC Confirmed Dynamic Changes in Matrisome Abundance

GO analysis of IN fraction proteins generated time point-specific terms (Figure 5A, Supplemental Table 1). E14.5 kidneys were ascribed GO terms that included “embryonic development” and “microfibril.” Terms assigned to E18.5 and P3 included “microfibril,” “sequestration of TGF β ,” and “anchoring collagen complex.” “Elastic fibers” and basement membrane-related terms were assigned only to the P3 and adult kidney.

To validate the proteomic trends (Supplemental Figures 3–7), cryosections of kidneys were stained with antibodies against type IV collagen (COL4) and type V collagen (COL5), and dolichos biflorus agglutinin (a collecting duct marker) (Figure 5B, Supplemental Figure 8).⁴⁷ LC-MS/MS analysis indicated COL5A2 significantly varied over development with a peak at P3 (Supplemental Figure 4). COL5 was visualized around tubules at E14.5. At perinatal time points, COL5 fibers were observed around the medullary rays, referred to as “medullary ray sheath fibers” (* in Figure 5B; Supplemental Table 6 includes nonstandard terms defined in this publication); however, in the adult, COL5 was less prevalent

and was interspersed between the tubules. In contrast, the number of COL4-positive nephron elements significantly increased with time compared with interstitial space (Figure 5B).

3D Visualization of the Developing Kidney Revealed Intricate Architecture of the Interstitial Matrix

By decellularizing developing murine forelimbs, we previously identified 3D ECM structures that were not revealed by standard 2D IHC.²⁷ Therefore, to gain insight into the 3D structure of the ECM, kidneys were decellularized, stained to identify proteins of interest, and imaged using confocal microscopy (Figure 6, Supplemental Figure 9). At E14.5, when the corticomedullary junction was forming, fibers positive for COL5 surrounded the developing nephron (COL4, HSPG2, FREM2) or ran parallel to blood vessels (open arrowhead), but did not form bundles (Figure 7, A–C, Supplemental Figures 10–12, Supplemental Videos 1–3). Fibers also circumferentially surrounded the developing ureter (Supplemental Videos 1–3). By E18.5 and P3, the interstitial matrix (COL1, COL5, COL6, POSTN) coalesced into medullary ray sheath fiber bundles (* in Figure 7) surrounding the tubules (COL4, HSPG2, FREM2; Figure 7, D–I', Supplemental Figures 10–12, Supplemental Videos 1–5). These fibers appeared continuous with the kidney calyx, pelvis, and ureter, and subdivided the medullary rays at cortical points (Supplemental Videos 1–5). The medullary ray sheath fibers were also observed using SeeDB, a clearing method that enhances light penetration of intact tissues (including cells), indicating the structures were not an artifact of the decellularization process (Supplemental Figure 13).

Fibers at E14.5 emanated from, and ran parallel to, the subcapsular tubules to the capsule. At E18.5 and P3, COL5+ and COL1+ fibers ran parallel to the tubules, which we term “vertical fibers” (arrow in Figure 8, A, C, and E, Supplemental Figures 14, 15, 17, and 18, Supplemental Table 6). Vertical fibers were observed from the base of the medullary ray sheath fibers to the nephrogenic cortex, where the vertical fibers intertwined at the POSTN+ capsule (Figures 7 and 8, Supplemental Figure 18, Supplemental Videos 6 and 7). In contrast to the cortex, fibers in the medulla were perpendicular to the tubules in a “rungs-of-a-ladder” configuration (closed arrowhead in Figure 8, B, D, and F, Supplemental Figures 16–18). In the adult, bulk accumulation of fibers or clear cortical or medullary patterning was not observed, but rungs-of-a-ladder structures were detected (Supplemental Figure 19). The 3D imaging revealed dynamic structures of the interstitial ECM that have not been previously described in the cortex and corticomedullary junction at perinatal time points (Supplemental Table 6).

DISCUSSION

The paucity of information about the interstitial matrix in the kidney was noted >20 years ago.⁴⁸ Whereas components,

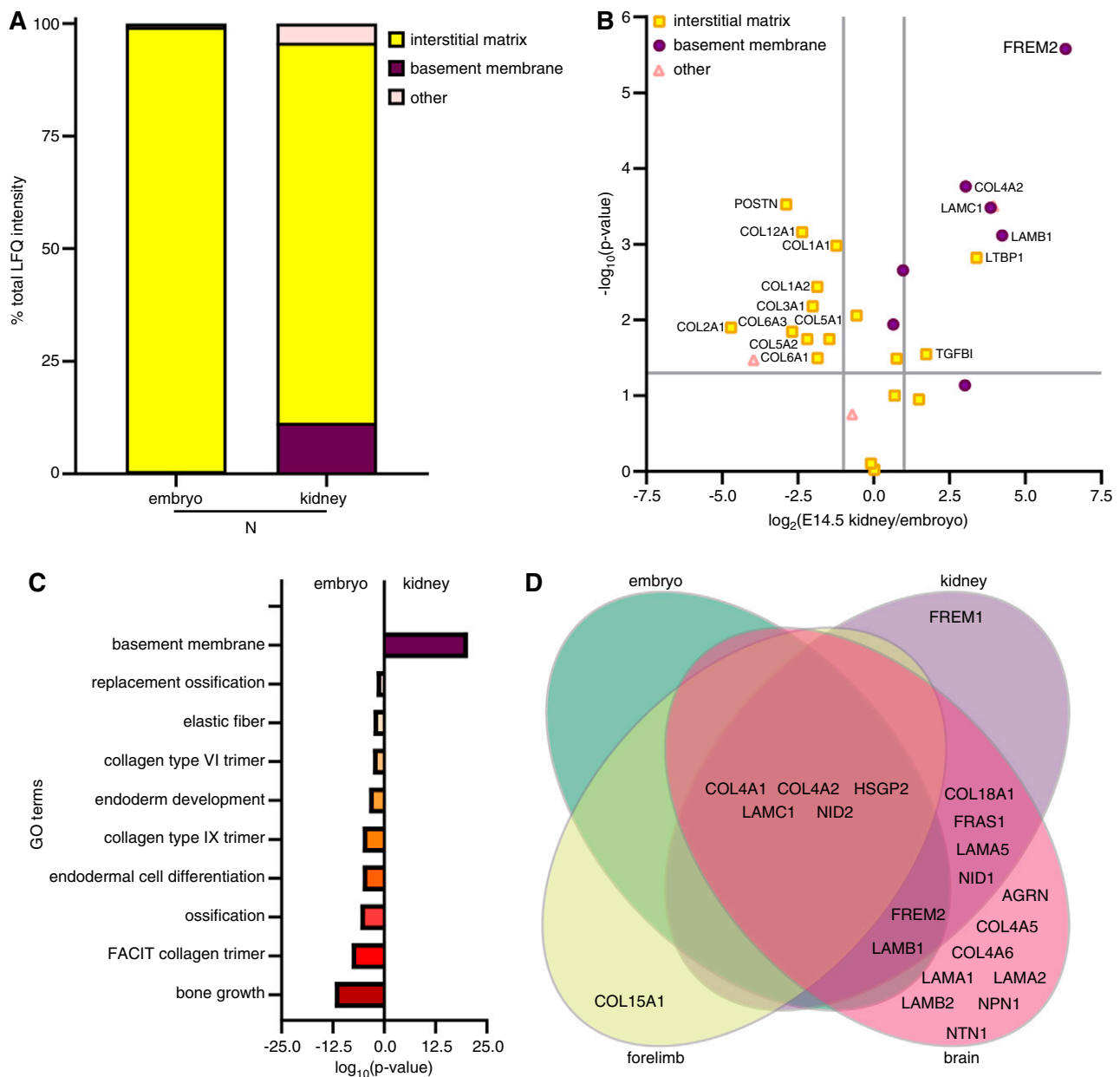


Figure 2. The kidney basement membrane matrisome was specialized by E14.5. (A) There was a significant decrease in interstitial matrix and increase in the basement membrane (unpaired, two-tailed t test $P < 0.001$ for both) in the E14.5 kidney compared with the embryo. (B) Volcano plot comparison of log₂-scaled LFQ values for the IN fraction of the E14.5 whole embryo and kidney. Significance was based on $P < 0.05$ and $|\text{fold change}| > 2$ (gray lines). (C) GO analysis terms generated using proteins significantly elevated or exclusively found in the IN fractions indicate the matrisome of the kidney was specialized by E14.5 when compared with the whole embryo. (D) Basement membrane from the IN fractions varied between different E14.5 tissues. Proteins were included if identified in $n \geq 2$ biologic replicates per time point, with $n = 3$ biologic replicates per time point (embryo, forelimb, and brain). FACIT, fibril-associated collagens with interrupted triple helices.

such as FN1 and FBN1, were shown to be critical for normal branching morphogenesis in explant cultures in the intervening years,^{49,50} the role of the interstitial matrix in kidney development *in vivo* is still unclear. To begin to address this gap in knowledge, we combined proteomic analyses and 3D imaging to map ECM dynamics during kidney development.⁵¹

The Composition and Structural Arrangement of the Interstitial Matrix Dynamically Changed over Development

Overall, we observed a global decrease in interstitial matrix proteins in the adult, as determined by mass spectrometry (Figure 4). FN1 and FBN2, glycoproteins with a role in

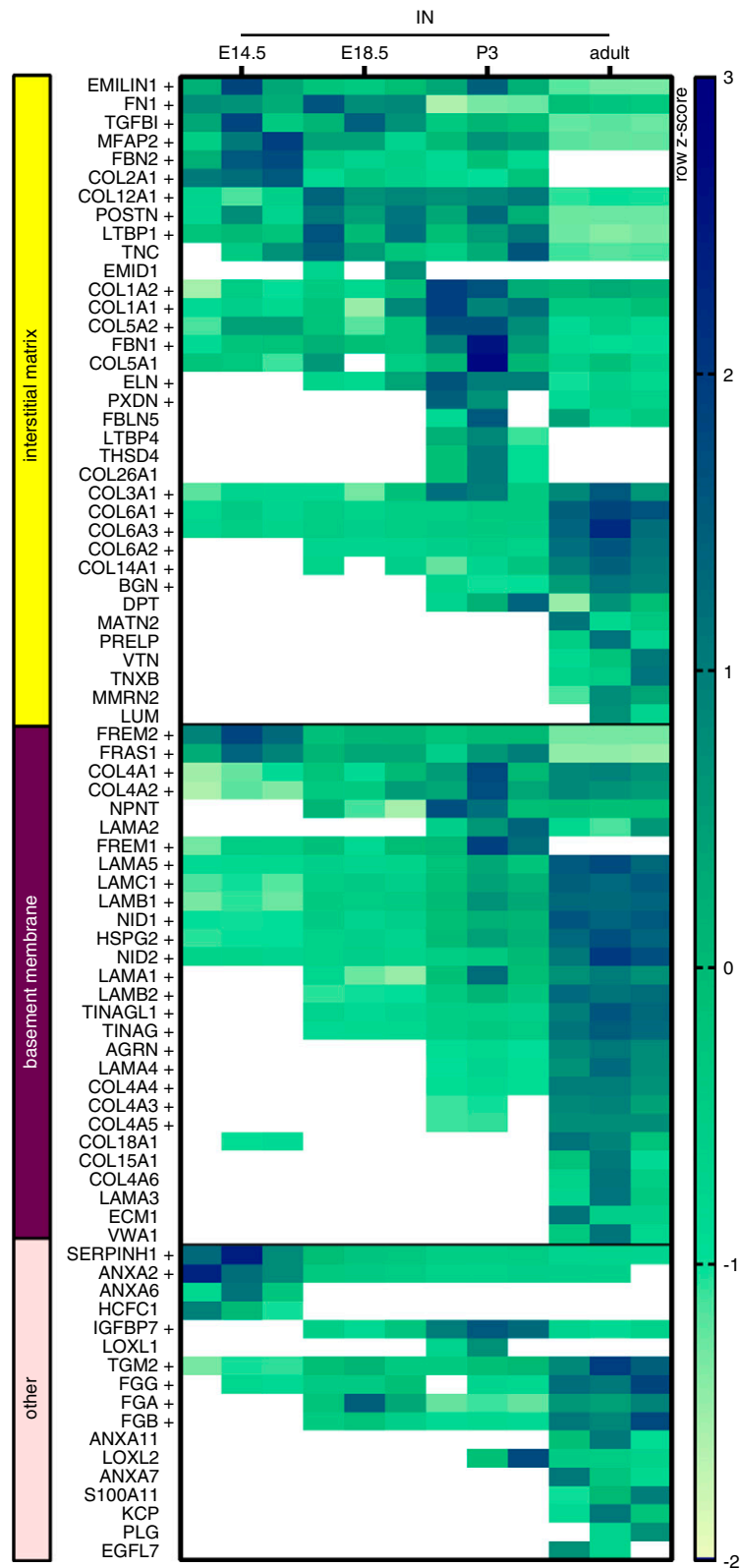


Figure 3. The composition of murine kidney interstitial matrix and basement membrane proteins significantly changed with development. Row z-score heatmap of matrisome components, based on scaled LFQ intensity, was manually grouped as interstitial matrix, basement membrane, and other ECM associated proteins for the IN fraction. + indicates $P < 0.05$ based on one-way ANOVA (identified in three to four time points) or unpaired, two-tailed t test (identified in two time points). Proteins identified in $n \geq 2$ biologic replicates per time point were included in the heatmap analysis. White boxes signify zero intensity values.

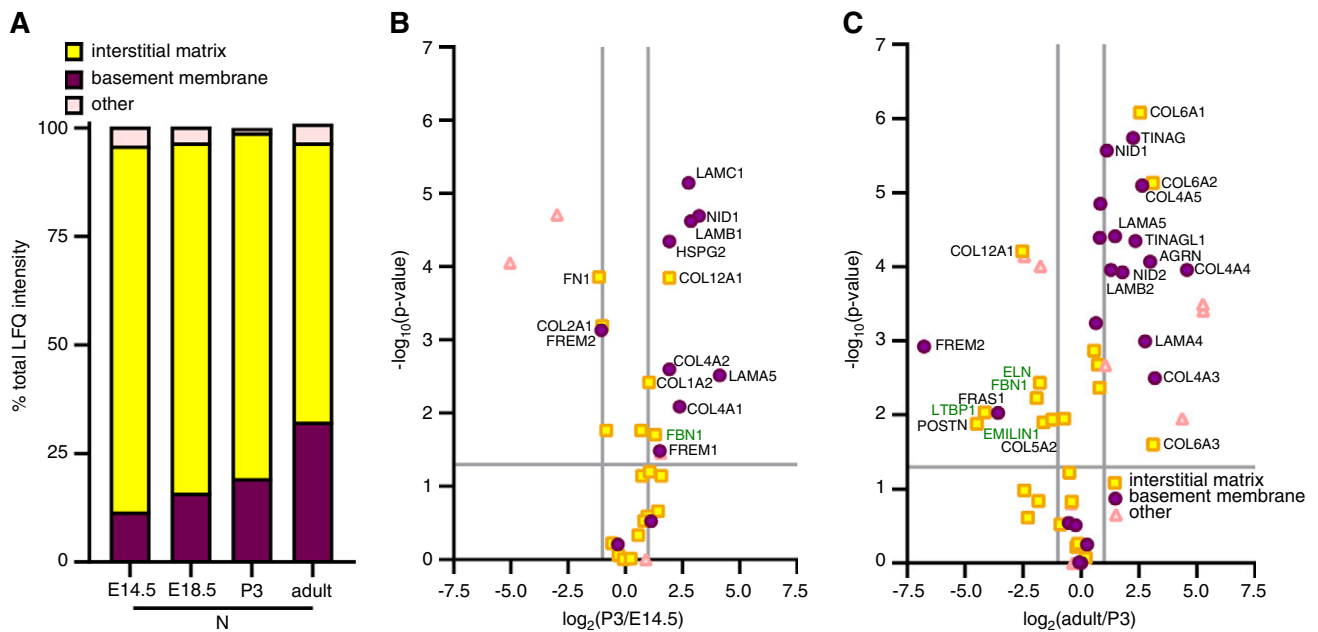


Figure 4. The relative composition of murine kidney interstitial matrix and basement membrane significantly changed with development. (A) There was a significant decrease in interstitial matrix and increase in basement membrane proteins identified in the IN fraction over development. One-way ANOVA ($P < 0.001$) and Tukey test between E14.5 and adult ($P < 0.001$) were significant for both interstitial matrix and basement membrane. (B and C) Volcano plots comparing proteins found in (B) P3 and E14.5 or (C) adult and P3 IN fractions. Green protein names indicate elastin-microfibril axis proteins. Significance was based on $P < 0.05$ and $|\text{fold change}| > 2$ (gray lines; $n = 3$ biologic replicates per time point).

orchestrating ECM assembly⁵² and acting as a scaffold, were enriched at early time points (Figure 3). The elevation in FN1 correlated with the critical role in promoting branching in explant cultures.⁴⁹ COL2A1, classically associated with cartilage formation,⁵³ was also elevated in the developing kidney (Figure 3). COL2A1 polymerizes into fibrils that provide strength in tension and may support the developing kidney epithelium by enhancing the attachment to the underlying mesenchyme.⁵⁴

In the E14.5 kidney, our 3D analysis showed COL5+ fibers circumferentially surrounding the ureteric bud (Supplemental Video 1) in a similar pattern to the layers of primary stromal mesenchyme.⁵⁵ COL5 is critical for COL1 fibrillogenesis⁵⁶ and forms fibrils that provide resistance to tensile forces.⁵⁷ When COL5 assembly was specifically disrupted in other tissues (e.g., tendon, cornea), COL1 fibers were abnormally enlarged and disorganized, suggesting COL5 also modulates COL1 assembly in the kidney. Vertically aligned fibers, containing COL5, were found in the cortex of E14.5 to P3 kidneys running parallel to the nephron, extending perpendicular from the corticomedullary junction fibers to intertwine within the capsule (Figures 7 and 8, Supplemental Figure 15, Supplemental Videos 1 and 6). Although we observed a few fibers connecting the collecting duct ampule to the capsule, as previously described,⁵⁸ the majority envelop the nephron elements in vertical fibers. Like the ampule fibers, we hypothesize the vertical fibers regulate tissue stability and maintain the radial growth of the collecting duct due to

connection with the capsule. Fibers bridging the collecting duct and loop of Henle in the medulla were observed from E18.5 to adult (Figure 8, Supplemental Figures 16–19), similar to the rungs-of-a-ladder orientation of stromal cells previously described.⁵⁹ We hypothesize the COL5+ ECM structures are involved in maintaining the tubular arrangement to facilitate concentrating filtrate in the medulla.⁶⁰

At E14.5, ECM fibers ran parallel to blood vessels, which may remodel into the interconnected rings of medullary ray sheath fibers at the perinatal time points (Figure 7). We hypothesize these COL1+, COL5+, and POSTN+ interstitial matrix structures provided bundling structural support of the loop of Henle considering the role of COL1 in tissue strength. Maturation of collagen fibers involves COL5 and POSTN, an ECM glycoprotein that activates lysyl oxidase-mediated collagen crosslinking. Specifically, POSTN was increased in mechanically stressed kidneys and was required to maintain tensile strength in other tissues (e.g., cardiac tissue), suggesting the medullary ray sheath fibers provided kidney tissue integrity. The location of the medullary ray sheath fibers correlated with the distribution of primary stromal mesenchymal cells. Over the course of development, the stromal cells become restricted to areas between the medullary rays,^{61–63} and the space is filled by the radial outgrowth of the nephron cascade.^{59,61,64–66} However, it is unclear if the medullary ray sheath fibers are remodeled into the perivascular fibers or are degraded.

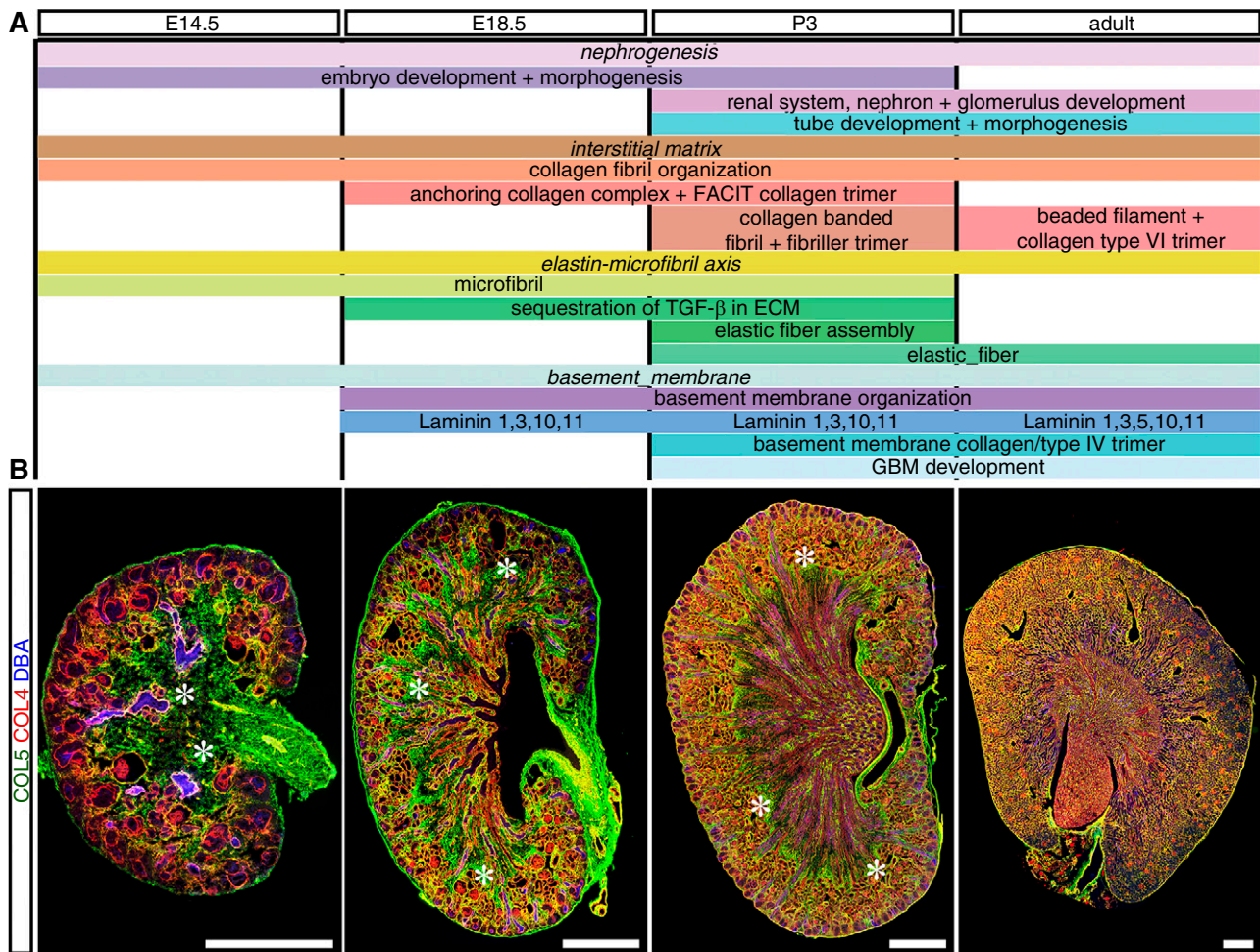


Figure 5. Dynamic changes in ECM function identified via GO analysis correlated with IHC. (A) GO analysis of proteins exclusive to, or significantly elevated in, the IN fraction (Supplemental Table 1) generated “biologic process” and “cellular compartment” terms that varied over development grouped into “nephrogenesis,” “interstitial matrix,” “elastin-microfibrils axis,” and “basement membrane” terms ($P < 0.05$). (B) Cryosections of E14.5 to adult kidneys showed a decrease in interstitial matrix, including medullary ray sheath fibers (*; green, COL5), and a corresponding increase in basement membrane area over development (red, COL4; blue, dolichos biflorus agglutinin [DBA; a collecting duct marker]). Scale bars, 500 μ m. Representative images from $n = 2$ biologic replicates. Individual channels can be found in Supplemental Figure 8. FACIT, fibril-associated collagens with interrupted triple helices; GBM, glomerular basement membrane.

At the same perinatal time points as the medullary ray sheath fibers were observed, LC-MS/MS revealed some interstitial matrix proteins were transiently increased. These included COL5A2, COL12A1, and POSTN (Figure 3).^{67,68} Additional proteins that were transiently upregulated include those associated with the elastin-microfibril axis (Figures 3 and 4C, green). ELN provides tissue compliance and FBNs form microfibrils that resist tensile loads, act as a scaffold for elastic fibril formation, and sequester growth factors.⁶⁹ The perinatal increase in abundance of these collagens and elastin-microfibril axis proteins may provide mechanical integrity by transiently stabilizing the 3D fibrous medullary ray sheath and vertical fibers, and modulating growth-factor availability (Figures 5 and 7). Interestingly, proteins in the elastin-microfibril axis (EMILIN1, FBN1–3, and THSD4)^{44–46}

were also elevated in human fetal kidneys compared with the adult,¹² indicating this axis in the kidney warrants further research.^{45,46}

In contrast with the fibrous structures observed at perinatal time points, relatively little interstitial patterning was observed in the adult after decellularization (Supplemental Figure 19). Complex structures may be resolved in the adult if perfusion decellularization is used, because previous studies showed perivascular fibers and rungs-of-a-ladder fibers near the tubules and capillaries.^{24,70} The organization of the rungs-of-a-ladder fibers correlated with the increase in proteins interacting with the basement membrane we observed in the adult matrisome. TNXB, an ECM glycoprotein implicated in the regulation of collagen fibril spacing,⁷¹ was found only in the adult (Figure 3). The increase in TNXB could provide support related to the increased

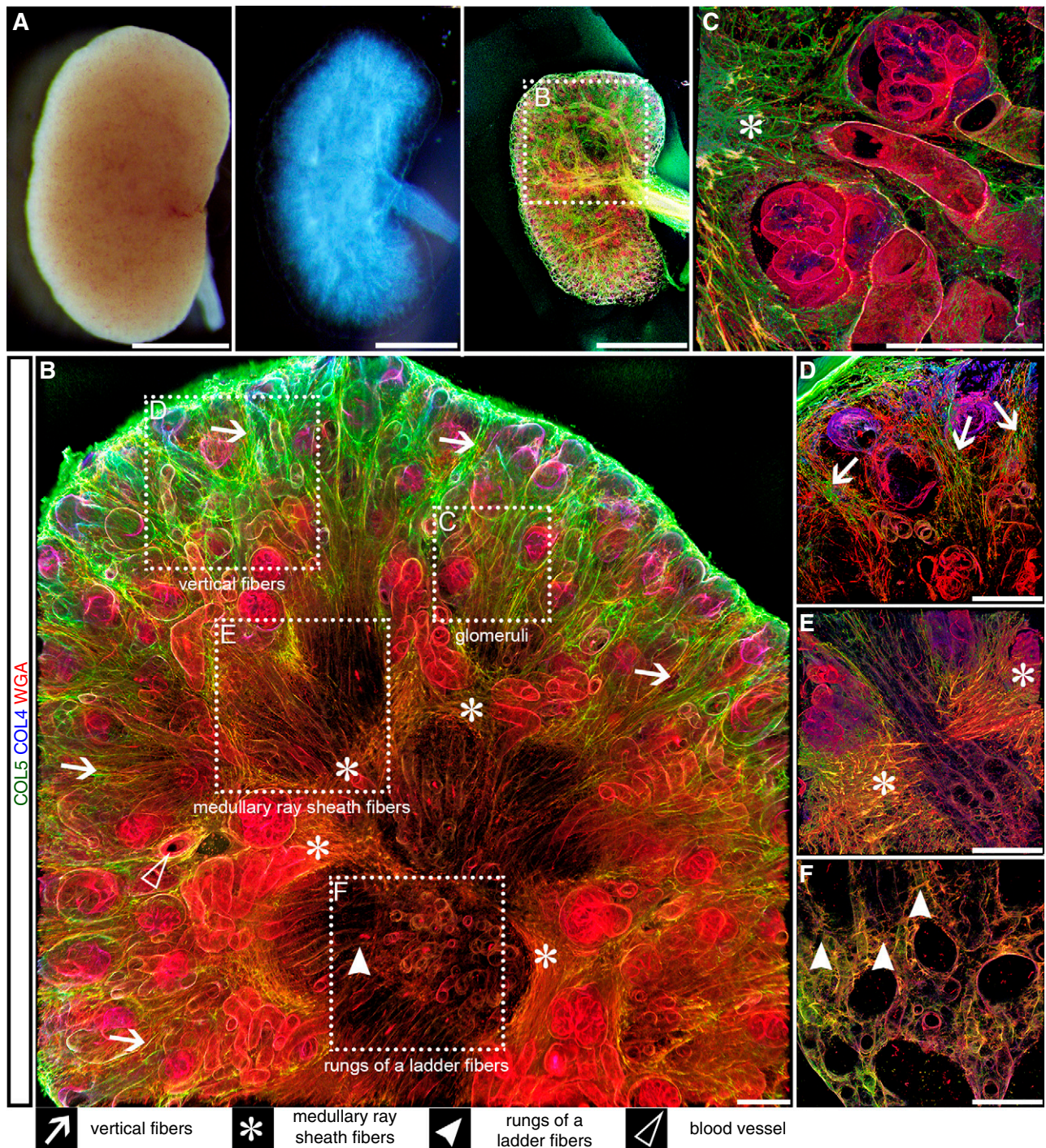


Figure 6. Decellularization revealed a complex 3D arrangement of the ECM during murine kidney development. (A) Freshly harvested kidneys (left) were decellularized in SDS (middle), and then stained for ECM of interest (right; E18.5 kidney). Scale bar, 1 mm. Green, COL5; blue, COL4; red, wheat germ agglutinin [WGA; proteoglycans]. (B) Fibers in the glomeruli, cortex, corticomedullary junction, and blood vessels (open arrowhead) were visualized in 3D within a decellularized E18.5 kidney. Original magnification, $\times 10$. (C–F) Representative confocal images from different areas of the kidney (indicated in [B] with boxes) at higher magnification. (C) Fibrous ECM (*) surrounded glomeruli. Original magnification, $\times 63$. (D) Vertical fibers (arrow) were visualized on the cortical surface. Original magnification, $\times 40$. (E) Medullary ray sheath fibers (*) were observed at the corticomedullary junction. Original magnification, $\times 40$. (F) Fibers with a rungs-of-a-ladder morphology (closed arrowhead) were observed in the medulla. Original magnification, $40\times$. Scale bars in (B–F), $100\ \mu\text{m}$. Confocal z-stack dimensions: $1.42\ \text{mm}\times 1.42\ \text{mm}\times 100\ \mu\text{m}$ ($x\times y\times z$) in (B); $225\times 225\times 37\ \mu\text{m}$ in (C); $354\times 354\times 45\ \mu\text{m}$ in (D and E); $354\times 354\times 11\ \mu\text{m}$ in (F). Representative image of decellularized kidneys from all time points can be found in Supplemental Figure 9.

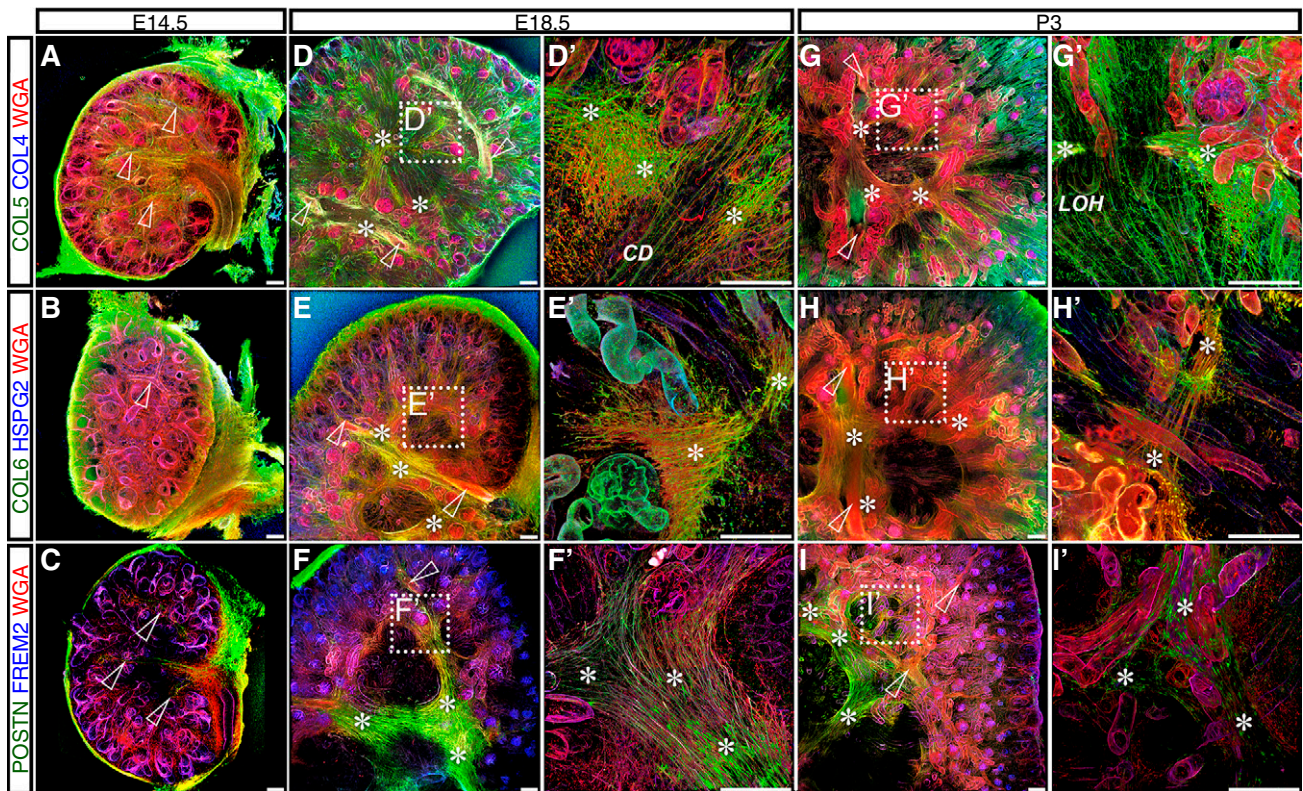


Figure 7. Medullary ray sheath fibers were only found at E18.5 and P3. (A–C) At E14.5, a fibrous ECM (green, COL5, COL6, POSTN) ran parallel to developing blood vessels (open arrowheads) and surrounded tubules (blue, COL4, HSPG2, FREM2; red, wheat germ agglutinin [WGA]). (D–I') Medullary ray sheath fibers (*) surrounded the developing nephron at E18.5 to P3. Boxes indicate where representative inset at a higher magnification was obtained. Scale bars, 100 μ m. Dimensions of confocal z-stacks: 1.42 mm \times 1.42 mm \times 100 μ m (x \times y \times z) in (A), (B), (D), (E), (G), and (H); 1.48 mm \times 1.48 mm \times 148 μ m in (C), (F), and (I); 354 \times 354 \times 45 μ m in (D') and (G'); 354 \times 354 \times 36 μ m in (E') and (H'); 345 \times 345 \times 57 μ m in (F') and (I'). Representative images from $n=3$ biologic replicates. Individual channels can be found in Supplemental Figures 10–12. CD, collecting duct; LOH, loop of Henle. Original magnification, $\times 10$ in A–I; $\times 40$ in D', E', G', and H'; $\times 25$ in F' and I'.

hydrostatic pressure with kidney maturation,⁵¹ as it was suggested that TNXB was necessary for closing the ureterovesical junction during voiding.⁷² Likewise, type VI collagen (COL6), a network-forming collagen made up of COL6A1–3 chains, bridges the interstitial matrix to the basement membrane⁷³ and is significantly increased in the adult (Figure 3). A patient with recurrent hematuria had a mutation in COL6A1, suggesting a disruption of COL6A1 lessened the anchoring of the interstitial matrix to, and increased proteolytic damage of, the basement membrane.⁷⁴ This indicated COL6A1 could be required to withstand the increased pressure found in the mature kidney. SLRPs, which sequester growth factors and connect the interstitial matrix to the basement membrane, were also increased in adult tissue (Figure 3).^{75,76} The increase in SLRPs could be a physiologic response to the increased hydrostatic pressures observed in the adult.⁵¹ This supposition is made on the basis of reports of proteoglycans providing strength in other tissues.⁷⁵ In addition, mice in which the SLRP BGN was knocked out had cystic dilation of tubules in response to increased hydrostatic pressure, potentially resulting from weakened connective tissue integration.^{77–79}

The Basement Membrane Dynamically Changed in Composition with Kidney Development

The basement membrane composition of embryonic kidneys was already specialized by E14.5 when compared with other tissues. The Fraser syndrome complex proteins (FRAS1, FREM2) were elevated in the E14.5 kidney relative to the adult kidney. The change was specific to the developing kidney and not a general elevation with development (Figures 2–4 and 7). Different Fraser complex components are secreted by the ureteric bud and metanephric mesenchyme, together forming a complex that promotes epithelial-mesenchymal interaction and acts as a scaffold for the nephrogenic microenvironment. Mutations in Fraser complex proteins were associated with anomalous nephrogenic signaling and kidney agenesis.^{80,81} The early differentiation of the basement membrane can explain the strong kidney phenotype for patients with Fraser complex protein mutations.⁸²

Overall, the abundance and complexity of the basement membrane matrisome increased in the adult kidney compared with developmental time points (Figures 3–5). The general increase in basement membrane proteins is likely due to the

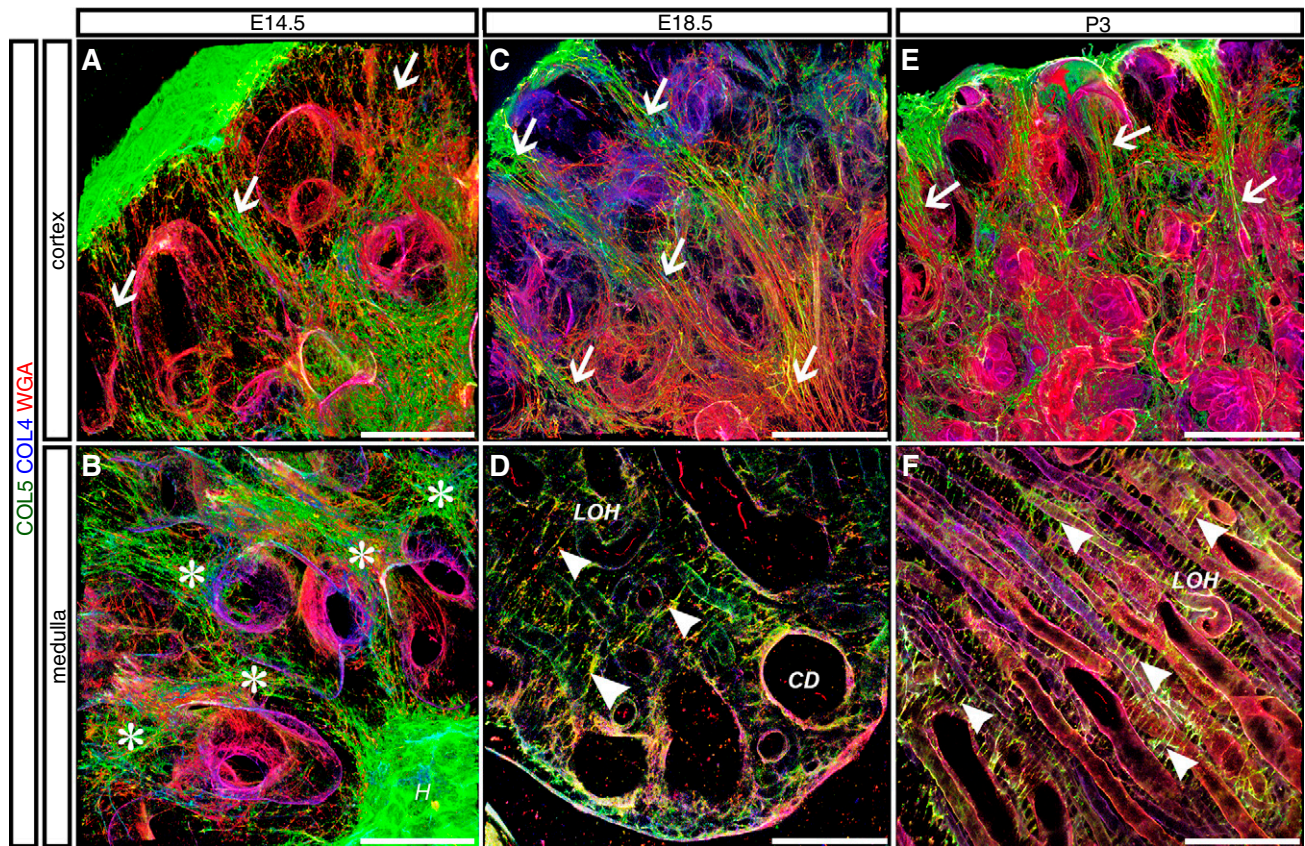


Figure 8. The morphology of interstitial fibers was distinct between the cortex and medulla. (A, C, and E) E14.5, E18.5, and P3 vertical fibers (arrows) ran parallel to, and emanated from, the tubules to the capsule in vertical fibers (green, COL5; blue, COL4; red, wheat germ agglutinin [WGA]). (B) Some E14.5 fibers (*) extended from the developing kidney hilum (H). (D and F) Rungs-of-a-ladder appearance of the interstitial matrix (closed arrowheads) at E18.5 and P3 between loop of Henle (LOH) and collecting duct (CD) tubules. Scale bars, 100 μ m. Dimensions of confocal z-stacks: 354 \times 354 \times 45 μ m (x \times y \times z) in (A), (B), (C), and (E); 354 \times 354 \times 11 μ m in (D) and (F). Representative images from $n=3$ biologic replicates. Individual channels can be found in Supplemental Figures 13 and 14. Original magnification, $\times 40$.

increase in total basement membrane volume as shown in 3D for COL4 and HSPG2 (Supplemental Figures 10 and 11, Supplemental Videos 1 and 2), and the previously described increase in thickness with age.^{83–85} This change in geometry could be a physiologic response to increasing hydrostatic pressure and urine output with development.^{51,86} COL4 and HSPG2 are necessary for basement membrane integrity, because mutations can lead to tubular basement membrane splitting and cysts, glomerulocystic disease, and altered functioning of the glomerular basement membrane.^{87–89} Proteins known to promote glomerular filtration unit stability and maturation,^{90–94} COL4A3–5, LAMA3, LAMA5, and LAMB2, were significantly elevated or exclusive to the adult (Figures 3 and 4C). The increase correlated to the incorporation of these chains into the mature glomerular basement membrane collagen and laminin during the capillary-loop stage of glomerulogenesis.^{93,95} Mutations in *COL4A3–5* can yield Alport syndrome that manifests as glomerular hematuria,⁹¹ whereas mutations in *LAMB2* and *LAMA5* yield nephrotic syndrome.^{92,94}

A Common Kidney Matrisome was Observed Across Multiple Proteomic Studies

We identified 110 ECM proteins and resolved significant differences in the matrisome composition over time. Future proteomic studies with additional digestion steps or increased separation during the liquid-chromatography phase of LC-MS/MS would identify more ECM proteins. Despite the extensive overlap with proteins identified in previous studies,^{9–18,36,37} there were some differences in proteins identified (Supplemental Table 4). Variations could be due to different tissue-fractionation methods and protein abundance. For example, our study did not resolve COL6A4–6 and FBLN1 (Supplemental Table 4).^{96–98} These proteins were potentially extracted in the less-stringent buffers at earlier time points as the ECM was still being incorporated into a cohesive network.^{31(preprint)} This is supported by enzymes involved in ECM crosslinking,^{4,99} including LOXL1, LOXL2, PXDN, TGM1, and TGM2, which increased in abundance in the postnatal and adult kidney (Supplemental Figure 3, Supplemental Table 1).

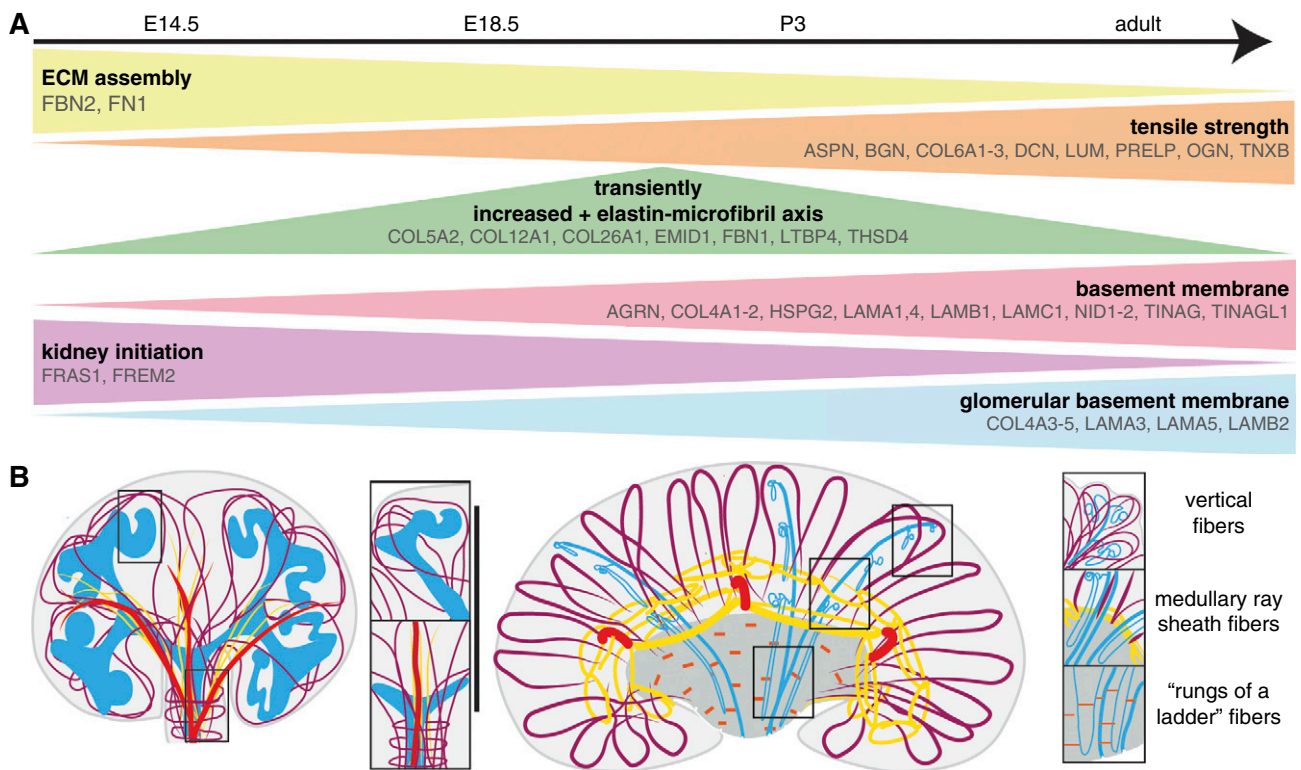


Figure 9. Summary of dynamic changes in interstitial matrix and basement membrane composition and 3D structures during kidney development. (A) LC-MS/MS revealed matrisome components changed dynamically with development, including proteins involved in ECM assembly, tensile strength, elastin-microfibril axis, kidney initiation, basement membrane, and glomerular basement membrane. (B) 3D interstitial matrix was patterned at E14.5 (left) with fibers (purple) circumferentially surrounding the ureteric bud (cyan), extending parallel (yellow) to the blood vessels (red), surrounding the developing nephron (cyan), and connecting to the capsule. At perinatal time points (right), vertical fibers (purple) interconnected at the cortical surface and extended to the corticomedullary junction. At the corticomedullary junction, medullary ray sheath fibers (yellow) surrounded the developing nephron (cyan). In the medulla, fibers in a rungs-of-a-ladder orientation were observed (orange).

By combining proteomics and 3D imaging of decellularized kidneys, we resolved previously undescribed dynamics of the interstitial matrix. We demonstrated that the kidney basement membrane is distinct by E14.5. We also identified the transient presence of vertical and medullary ray sheath fibers in the perinatal kidney. On the basis of the 3D ECM patterning and proteomic data, we generated a map of the ECM during kidney development (Figure 9). We envision tissue-engineering models that incorporate an ECM scaffold based on the native composition and structure, such as Fraser complex proteins and interstitial proteins, will improve cues and growth-factor availability and act as a baseline readout for kidney cell maturation. Outstanding questions remain regarding how interstitial matrix proteins regulate kidney morphogenesis through structural support and growth-factor signaling. Future studies on the role of the interstitial matrix will provide additional insight into kidney development and improve the design of models of nephrogenesis.

DISCLOSURES

All authors have nothing to disclose.

FUNDING

This work was supported by National Center for Complementary and Integrative Health grant DP2 AT009833 (to S. Calve). This publication was made possible with partial support of S.N. Lipp by the National Center for Advancing Translational Sciences Clinical and Translational Sciences Award, *via* grants UL1TR002529 (principal investigator, Dr. Shekhar) and TL1TR002531 (principal investigator, Dr. Hurley).

ACKNOWLEDGMENTS

The authors would like to thank the Purdue Proteomics Facility and members of the Calve laboratory for helpful discussions, assistance with proteomics and mouse husbandry (Mr. Alexander Ocken and Dr. Naagarajan Narayanan), and confocal microscopy (Dr. Yue Leng and Dr. Andrea Acuña). In addition, the authors thank Ms. Jennifer Anderson for help with the development of the perfusion protocol. The authors would like to thank the Purdue Proteomics Facility and members of the Calve laboratory for helpful discussions, assistance with proteomics and mouse husbandry (Alexander Ocken and Dr. Naagarajan Narayanan), and confocal microscopy (Yue Leng and Andrea Acuña). In addition, the authors thank Jennifer Anderson for help with the development of the perfusion protocol.

S.N. Lipp and S. Calve designed the experiments with input from K.R. Jacobson, D.S. Hains, and A.L. Schwaderer; S.N. Lipp performed the

experiments; and S.N. Lipp and S. Calve analyzed and interpreted the data and wrote the manuscript, with input from K.R. Jacobson, D.S. Hains, and A.L. Schwaderer.

DATA SHARING STATEMENT

The data supporting the findings of this study are openly available in the MassIVE repository at MSV000085616. The whole-embryo E14.5 data were derived from Jacobson *et al.*³¹(preprint) and are included in the MassIVE upload.

SUPPLEMENTAL MATERIAL

This article contains the following supplemental material online at <http://jasn.asnjournals.org/lookup/suppl/doi:10.1681/ASN.2020081204/-/DCSupplemental>.

Supplemental Appendix 1. Supplemental Methods.

Supplemental Video 1. 10× medullary ray sheath fibers at E14.5, E18.5, and P3 kidneys stained for COL5, COL4, and WGA.

Supplemental Video 2. 10× medullary ray sheath fibers at E14.5, E18.5, and P3 kidneys stained for COL6, HSPG2, and WGA.

Supplemental Video 3. 10× medullary ray sheath fibers at E14.5, E18.5, and P3 kidneys stained for POSTN, FREM2, and WGA.

Supplemental Video 4. 40× medullary ray sheath fibers at E18.5 and P3 kidneys stained for COL5, COL4, and WGA.

Supplemental Video 5. 25× medullary ray sheath fibers at E14.5, E18.5, and P3 kidneys stained for POSTN, FREM2, and WGA.

Supplemental Video 6. 40× vertical fibers in the cortex of E14.5, E18.5, and P3 kidneys stained for COL5, COL4, and WGA.

Supplemental Video 7. 25× fibers in the capsule of E14.5, E18.5, and P3 kidneys stained for POSTN, FREM2, and WGA.

Supplemental Table 1. Raw data supporting the comparison of the matrisome during kidney development.

Supplemental Table 2. Classifications of proteins based on interstitial matrix, basement membrane, and other.

Supplemental Table 3. Raw data supporting the comparison of the matrisome between E14.5 kidneys and whole embryos.

Supplemental Table 4. A common kidney matrisome was observed across different studies.

Supplemental Table 5. Materials and settings used for imaging the kidney ECM.

Supplemental Table 6. Definition of non-standard terms used in this manuscript.

Supplemental Figure 1. Flow diagram of the functional classification of proteins as interstitial matrix, basement membrane, and other ECM associated proteins for matrisome identified in this study.

Supplemental Figure 2. Proteomic analysis showed high reproducibility between the matrisome for biological replicates.

Supplemental Figure 3. Heat map comparison of the dynamic changes of the matrisome for both the IN and CS fraction.

Supplemental Figure 4. Scaled LFQ intensity values for the IN fraction for interstitial matrix proteins discussed in the manuscript (COL1A1-FBN1).

Supplemental Figure 5. Scaled LFQ intensity values for the IN fraction for interstitial matrix proteins discussed in the manuscript (FBN2-POSTN).

Supplemental Figure 6. Scaled LFQ intensity values for the IN fraction for basement membrane proteins discussed in the manuscript (AGRN-LAMA2).

Supplemental Figure 7. Scaled LFQ intensity values for the IN fraction for basement membrane proteins discussed in the manuscript (LAMA4-TINAGLI).

Supplemental Figure 8. Spatiotemporal change of COL5 and COL4 in murine developing kidney.

Supplemental Figure 9. Representative image of decellularized kidneys from E14.5, E18.5, P3, and adult.

Supplemental Figure 10. Medullary ray sheath fibers were only found at E18.5 and P3 and contained COL5.

Supplemental Figure 11. Medullary ray sheath fibers were only found at E18.5 and P3 and contained COL6.

Supplemental Figure 12. Medullary ray sheath fibers were only found at E18.5 and P3 and contained POSTN.

Supplemental Figure 13. COL5+ medullary ray sheath fibers were observed in decellularized and SeeDB-cleared kidneys.

Supplemental Figure 14. Colocalization of COL1 and COL5 in the E18.5 kidney cortex and corticomedullary junction.

Supplemental Figure 15. COL5+ vertical fibers were observed in the cortex.

Supplemental Figure 16. COL5+ “rungs of a ladder” fibers were observed in the medulla.

Supplemental Figure 17. The morphology of interstitial fibers was distinct between cortex and medulla for COL6.

Supplemental Figure 18. The morphology of interstitial fibers was distinct between the cortex and medulla.

Supplemental Figure 19. Interstitial accumulations were not observed in the adult mouse kidney.

REFERENCES

1. United States Renal Data System Annual Data Report: Epidemiology of kidney disease in the United States, 2018. Available at: <https://usrds.org/annual-data-report/previous-adrs>. Accessed May 29, 2020
2. Destefani AC, Sirtoli GM, Nogueira BV: Advances in the knowledge about kidney decellularization and repopulation. *Front Bioeng Biotechnol* 5: 34, 2017
3. Garreta E, Prado P, Tarantino C, Oria R, Fanlo L, Martí E, et al.: Fine tuning the extracellular environment accelerates the derivation of kidney organoids from human pluripotent stem cells. *Nat Mater* 18: 397–405, 2019
4. Bonnans C, Chou J, Werb Z: Remodelling the extracellular matrix in development and disease. *Nat Rev Mol Cell Biol* 15: 786–801, 2014
5. Byron A, Humphries JD, Humphries MJ: Defining the extracellular matrix using proteomics. *Int J Exp Pathol* 94: 75–92, 2013
6. Chew C, Lennon R: Basement membrane defects in genetic kidney diseases. *Front Pediatr* 6: 11, 2018
7. Reint G, Rak-Raszewska A, Vainio SJ: Kidney development and perspectives for organ engineering. *Cell Tissue Res* 369: 171–183, 2017
8. Taha IN, Naba A: Exploring the extracellular matrix in health and disease using proteomics. *Essays Biochem* 63: 417–432, 2019
9. Nakayama KH, Lee CC, Batchelder CA, Tarantal AF: Tissue specificity of decellularized rhesus monkey kidney and lung scaffolds. *PLoS One* 8: e64134, 2013
10. Gessel M, Spraggins JM, Vozyan P, Hudson BG, Caprioli RM: Decellularization of intact tissue enables MALDI imaging mass spectrometry analysis of the extracellular matrix. *J Mass Spectrom* 50: 1288–1293, 2015
11. Liu P, Xie X, Jin J: Isotopic nitrogen-15 labeling of mice identified long-lived proteins of the renal basement membranes. *Sci Rep* 10: 5317, 2020
12. Louzao-Martinez L, van Dijk CGM, Xu YJ, Korn A, Bekker NJ, Brouwhuis R, et al.: A proteome comparison between human fetal and mature renal extracellular matrix identifies EMILIN1 as a regulator of renal epithelial cell adhesion. *Matrix Bio Plus* 4: 100011, 2019
13. Lennon R, Byron A, Humphries JD, Randles MJ, Carisey A, Murphy S, et al.: Global analysis reveals the complexity of the human glomerular extracellular matrix. *J Am Soc Nephrol* 25: 939–951, 2014
14. Hobeika L, Barati MT, Caster DJ, McLeish KR, Merchant ML: Characterization of glomerular extracellular matrix by proteomic analysis of laser-captured microdissected glomeruli. *Kidney Int* 91: 501–511, 2017
15. Randles MJ, Woolf AS, Huang JL, Byron A, Humphries JD, Price KL, et al.: Genetic background is a key determinant of glomerular

- extracellular matrix composition and organization. *J Am Soc Nephrol* 26: 3021–3034, 2015
16. Paunas FTI, Finne K, Leh S, Osman TA-H, Marti H-P, Berven F, et al.: Characterization of glomerular extracellular matrix in IgA nephropathy by proteomic analysis of laser-captured microdissected glomeruli. *BMC Nephrol* 20: 410, 2019
 17. Merchant ML, Barati MT, Caster DJ, Hata JL, Hobeika L, Coventry S, et al.: Proteomic analysis identifies distinct glomerular extracellular matrix in collapsing focal segmental glomerulosclerosis. *J Am Soc Nephrol* 31: 1883–1904, 2020
 18. van Dijk CGM, Louzao-Martinez L, van Mulligen E, Boermans B, Demmers JAA, van den Bosch TPP, et al.: Extracellular matrix analysis of human renal arteries in both quiescent and active vascular state. *Int J Mol Sci* 21: 3905, 2020
 19. Soulet F, Kilarski WW, Roux-Dalvai F, Herbert JM, Sacewicz I, Mouton-Barbosa E, et al.: Mapping the extracellular and membrane proteome associated with the vasculature and the stroma in the embryo. *Mol Cell Proteomics* 12: 2293–2312, 2013
 20. Nagao RJ, Xu J, Luo P, Xue J, Wang Y, Kotha S, et al.: Decellularized human kidney cortex hydrogels enhance kidney microvascular endothelial cell maturation and quiescence. *Tissue Eng Part A* 22: 1140–1150, 2016
 21. Mayorca-Guiliani AE, Madsen CD, Cox TR, Horton ER, Venning FA, Erler JT: ISDoT: In situ decellularization of tissues for high-resolution imaging and proteomic analysis of native extracellular matrix. *Nat Med* 23: 890–898, 2017
 22. Harunaga JS, Doyle AD, Yamada KM: Local and global dynamics of the basement membrane during branching morphogenesis require protease activity and actomyosin contractility. *Dev Biol* 394: 197–205, 2014
 23. Luo Y, Li N, Chen H, Fernandez GE, Warburton D, Moats R, et al.: Spatial and temporal changes in extracellular elastin and laminin distribution during lung alveolar development. *Sci Rep* 8: 8334, 2018
 24. Mayorca-Guiliani AE, Willacy O, Madsen CD, Rafeeva M, Elisabeth Heumüller S, Bock F, et al.: Decellularization and antibody staining of mouse tissues to map native extracellular matrix structures in 3D. *Nat Protoc* 14: 3395–3425, 2019
 25. Randles MJ, Collinson S, Starborg T, Mironov A, Krendel M, Königshausen E, et al.: Three-dimensional electron microscopy reveals the evolution of glomerular barrier injury. *Sci Rep* 6: 35068, 2016
 26. Munro DAD, Hohenstein P, Davies JA: Cycles of vascular plexus formation within the nephrogenic zone of the developing mouse kidney. *Sci Rep* 7: 3273, 2017
 27. Acuna A, Drakopoulos MA, Leng Y, Goergen CJ, Calve S: Three-dimensional visualization of extracellular matrix networks during murine development. *Dev Biol* 435: 122–129, 2018
 28. Naba A, Clauser KR, Hynes RO: Enrichment of extracellular matrix proteins from tissues and digestion into peptides for mass spectrometry analysis. *J Vis Exp* (101): e53057, 2015
 29. Saleh AM, Jacobson KR, Kinzer-Ursem TL, Calve S: Dynamics of non-canonical amino acid-labeled intra- and extracellular proteins in the developing mouse. *Cel Mol Bioeng* 12: 495–509, 2019
 30. Cox J, Mann M: MaxQuant enables high peptide identification rates, individualized p.p.b.-range mass accuracies and proteome-wide protein quantification. *Nat Biotechnol* 26: 1367–1372, 2008
 31. Jacobson KR, Saleh AM, Lipp SN, Ocken AR, Kinzer-Ursem TL, Calve S: Extracellular matrix protein composition dynamically changes during murine forelimb development. *bioRxiv*. 10.1101/2020.06.17.158204 (Preprint posted June 19, 2020)
 32. Naba A, Clauser KR, Ding H, Whittaker CA, Carr SA, Hynes RO: The extracellular matrix: Tools and insights for the “omics” era. *Matrix Biol* 49: 10–24, 2016
 33. Tsutsui K, Machida H, Morita R, Nakagawa A, Sekiguchi K, Miner JH, et al.: Mapping the molecular and structural specialization of the skin basement membrane for inter-tissue interactions. *bioRxiv*. 10.1101/2020.04.27.061952 (Preprint posted April 28, 2020)
 34. Raudvere U, Kolberg L, Kuzmin I, Arak T, Adler P, Peterson H, et al.: g:Profiler: a web server for functional enrichment analysis and conversions of gene lists (2019 update). *Nucleic Acids Res* 47[W1]: W191–W198, 2019
 35. Supek F, Bošnjak M, Škunca N, Šmuc T: REVIGO summarizes and visualizes long lists of gene ontology terms. *PLoS One* 6: e21800, 2011
 36. Hale LJ, Howden SE, Phipson B, Lonsdale A, Er PX, Ghobrial I, et al.: 3D organoid-derived human glomeruli for personalised podocyte disease modelling and drug screening. *Nat Commun* 9: 5167, 2018
 37. Byron A, Randles MJ, Humphries JD, Mironov A, Hamidi H, Harris S, et al.: Glomerular cell cross-talk influences composition and assembly of extracellular matrix. *J Am Soc Nephrol* 25: 953–966, 2014
 38. Ke M-T, Fujimoto S, Imai T: SeeDB: a simple and morphology-preserving optical clearing agent for neuronal circuit reconstruction. *Nature Neuroscience* 16: 1154–1161, 2013
 39. Cox J, Hein MY, Luber CA, Paron I, Nagaraj N, Mann M: Accurate proteome-wide label-free quantification by delayed normalization and maximal peptide ratio extraction, termed MaxLFQ. *Mol Cell Proteomics* 13: 2513–2526, 2014
 40. Urabe N, Naito I, Saito K, Yonezawa T, Sado Y, Yoshioka H, et al.: Basement membrane type IV collagen molecules in the choroid plexus, pia mater and capillaries in the mouse brain. *Arch Histol Cytol* 65: 133–143, 2002
 41. Peissel B, Geng L, Kalluri R, Kashtan C, Rennke HG, Gallo GR, et al.: Comparative distribution of the alpha 1(IV), alpha 5(IV), and alpha 6(IV) collagen chains in normal human adult and fetal tissues and in kidneys from X-linked Alport syndrome patients. *J Clin Invest* 96: 1948–1957, 1995
 42. Lohi J, Korhonen M, Leivo I, Kangas L, Tani T, Kalluri R, et al.: Expression of type IV collagen alpha1(IV)-alpha6(IV) polypeptides in normal and developing human kidney and in renal cell carcinomas and oncocytomas. *Int J Cancer* 72: 43–49, 1997
 43. Visel A, Thaller C, Eichele G: GenePaint.org: An atlas of gene expression patterns in the mouse embryo. *Nucleic Acids Res* 32: D552–D556, 2004
 44. Votteler M, Berrio DAC, Horke A, Sabatier L, Reinhardt DP, Nsair A, et al.: Elastogenesis at the onset of human cardiac valve development. *Development* 140: 2345–2353, 2013
 45. Sterzel RB, Hartner A, Schlötzer-Schrehardt U, Voit S, Hausknecht B, Doliana R, et al.: Elastic fiber proteins in the glomerular mesangium *in vivo* and in cell culture. *Kidney Int* 58: 1588–1602, 2000
 46. Leimeister C, Steidl C, Schumacher N, Erhard S, Gessler M: Developmental expression and biochemical characterization of Emu family members. *Dev Biol* 249: 204–218, 2002
 47. Laitinen L, Virtanen I, Saxén L: Changes in the glycosylation pattern during embryonic development of mouse kidney as revealed with lectin conjugates. *J Histochem Cytochem* 35: 55–65, 1987
 48. Kanwar YS, Carone FA, Kumar A, Wada J, Ota K, Wallner EI: Role of extracellular matrix, growth factors and proto-oncogenes in metanephric development. *Kidney Int* 52: 589–606, 1997
 49. Ye P, Habib SL, Ricono JM, Kim NH, Choudhury GG, Barnes JL, et al.: Fibronectin induces ureteric bud cells branching and cellular cord and tubule formation. *Kidney Int* 66: 1356–1364, 2004
 50. Kanwar YS, Ota K, Yang Q, Kumar A, Wada J, Kashiwara N, et al.: Isolation of rat fibrillin-1 cDNA and its relevance in metanephric development. *Am J Physiol* 275: F710–F723, 1998
 51. Spitzer A, Edelmann CM Jr: Maturation changes in pressure gradients for glomerular filtration. *Am J Physiol* 221: 1431–1435, 1971
 52. Dallas SL, Chen Q, Sivakumar P: Dynamics of assembly and reorganization of extracellular matrix proteins. *Curr Top Dev Biol* 75: 1–24, 2006
 53. Li SW, Prockop DJ, Helminen H, Fässler R, Lapveteläinen T, Kiraly K, et al.: Transgenic mice with targeted inactivation of the Col2 alpha 1 gene for collagen II develop a skeleton with membranous and periosteal bone but no endochondral bone. *Genes Dev* 9: 2821–2830, 1995

54. Kolpakova-Hart E, Nicolae C, Zhou J, Olsen BR: Col2-Cre recombinase is co-expressed with endogenous type II collagen in embryonic renal epithelium and drives development of polycystic kidney disease following inactivation of ciliary genes. *Matrix Biol* 27: 505–512, 2008
55. Alcorn D, Maric C, McCausland J: Development of the renal interstitium. *Pediatr Nephrol* 13: 347–354, 1999
56. Wenstrup RJ, Florer JB, Brunskill EW, Bell SM, Chervoneva I, Birk DE: Type V collagen controls the initiation of collagen fibril assembly. *J Biol Chem* 279: 53331–53337, 2004
57. Malfait F, Francomano C, Byers P, Belmont J, Berglund B, Black J, et al.: The 2017 international classification of the Ehlers-Danlos syndromes. *Am J Med Genet C Semin Med Genet* 175: 8–26, 2017
58. Schumacher K, Strehl R, De Vries U, Groene HJ, Minuth WW: SBA-positive fibers between the CD ampulla, mesenchyme, and renal capsule. *J Am Soc Nephrol* 13: 2446–2453, 2002
59. Maric C, Ryan GB, Alcorn D: Embryonic and postnatal development of the rat renal interstitium. *Anat Embryol (Berl)* 195: 503–514, 1997
60. Dantzer WH, Layton AT, Layton HE, Pannabecker TL: Urine-concentrating mechanism in the inner medulla: Function of the thin limbs of the loops of Henle. *Clin J Am Soc Nephrol* 9: 1781–1789, 2014
61. Speller AM, Moffat DB: Tubulo-vascular relationships in the developing kidney. *J Anat* 123: 487–500, 1977
62. Marxer-Meier A, Hegyi I, Löffing J, Kaissling B: Postnatal maturation of renal cortical peritubular fibroblasts in the rat. *Anat Embryol (Berl)* 197: 143–153, 1998
63. England AR, Chaney CP, Das A, Patel M, Malewska A, Armendariz D, et al.: Identification and characterization of cellular heterogeneity within the developing renal interstitium. *Development* 147: dev190108, 2020
64. Vize PD, Woolf AS, Bard JBL: *The Kidney: From Normal Development to Congenital Disease*, Amsterdam, Elsevier, 2003
65. Koseki C, Herzlinger D, al-Awqati Q: Apoptosis in metanephric development. *J Cell Biol* 119: 1327–1333, 1992
66. Sainio K, Nonclercq D, Saarma M, Palgi J, Saxén L, Sariola H: Neuronal characteristics in embryonic renal stroma. *Int J Dev Biol* 38: 77–84, 1994
67. Zou Y, Zwolanek D, Izu Y, Gandhi S, Schreiber G, Brockmann K, et al.: Recessive and dominant mutations in COL12A1 cause a novel EDS/myopathy overlap syndrome in humans and mice. *Hum Mol Genet* 23: 2339–2352, 2014
68. Chiquet M, Birk DE, Bönemann CG, Koch M: Collagen XII: Protecting bone and muscle integrity by organizing collagen fibrils. *Int J Biochem Cell Biol* 53: 51–54, 2014
69. Godwin ARF, Singh M, Lockhart-Cairns MP, Alanazi YF, Cain SA, Baldock C: The role of fibrillin and microfibril binding proteins in elastin and elastic fibre assembly. *Matrix Biol* 84: 17–30, 2019
70. Lemley KV, Kriz W: Anatomy of the renal interstitium. *Kidney Int* 39: 370–381, 1991
71. Eleftheriou F, Exposito JY, Garrone R, Lethias C: Binding of tenascin-X to decorin. *FEBS Lett* 495: 44–47, 2001
72. Gbadegesin RA, Brophy PD, Adeyemo A, Hall G, Gupta IR, Hains D, et al.: TNXB mutations can cause vesicoureteral reflux. *J Am Soc Nephrol* 24: 1313–1322, 2013
73. Lamandé SR, Bateman JF: Collagen VI disorders: Insights on form and function in the extracellular matrix and beyond. *Matrix Biol* 71–72: 348–367, 2018
74. Bao M, Mao F, Zhao Z, Ma G, Xu G, Xu W, et al.: COL6A1 mutation leading to Bethlem myopathy with recurrent hematuria: A case report. *BMC Neurol* 19: 32, 2019
75. Chen S, Birk DE: The regulatory roles of small leucine-rich proteoglycans in extracellular matrix assembly. *FEBS J* 280: 2120–2137, 2013
76. Bengtsson E, Mörgelin M, Sasaki T, Timpl R, Heinegård D, Aspberg A: The leucine-rich repeat protein PRELP binds perlecan and collagens and may function as a basement membrane anchor. *J Biol Chem* 277: 15061–15068, 2002
77. Schaefer L, Mihalik D, Babelova A, Krzyzankova M, Gröne HJ, Iozzo RV, et al.: Regulation of fibrillin-1 by biglycan and decorin is important for tissue preservation in the kidney during pressure-induced injury. *Am J Pathol* 165: 383–396, 2004
78. Kim EK, Choi ER, Song BG, Jang SY, Ko SM, Choi S-H, et al.: Presence of simple renal cysts is associated with increased risk of aortic dissection: A common manifestation of connective tissue degeneration? *Heart* 97: 55–59, 2011
79. Kaplan BS, Kaplan P, Kessler A: Cystic kidneys associated with connective tissue disorders. *Am J Med Genet* 69: 133–137, 1997
80. van der Ven AT, Vivante A, Hildebrandt F: Novel insights into the pathogenesis of monogenic congenital anomalies of the kidney and urinary tract. *J Am Soc Nephrol* 29: 36–50, 2018
81. Pitera JE, Scambler PJ, Woolf AS: Fras1, a basement membrane-associated protein mutated in Fraser syndrome, mediates both the initiation of the mammalian kidney and the integrity of renal glomeruli. *Hum Mol Genet* 17: 3953–3964, 2008
82. Barisic I, Odak L, Loane M, Garne E, Wellesley D, Calzolari E, et al.: Fraser syndrome: Epidemiological study in a European population. *Am J Med Genet A* 161A: 1012–1018, 2013
83. Vogler C, McAdams AJ, Homan SM: Glomerular basement membrane and lamina densa in infants and children: An ultrastructural evaluation. *Pediatr Pathol* 7: 527–534, 1987
84. Pietilä I, Prunskaitė-Hyryläinen R, Kaisto S, Tika E, van Eerde AM, Salo AM, et al.: Wnt5a deficiency leads to anomalies in ureteric tree development, tubular epithelial cell organization and basement membrane integrity pointing to a role in kidney collecting duct patterning. *PLoS One* 11: e0147171, 2016
85. Nishi S, Ueno M, Karasawa R, Kawashima S, In H, Hayashi H, et al.: Morphometric study of glomerular basement membrane and proximal tubular basement membrane in adult thin basement membrane disease. *Clin Exp Nephrol* 3: 290–295, 1999
86. Takeuchi H, Koyanagi T, Yoshizato T, Takashima T, Satoh S, Nakano H: Fetal urine production at different gestational ages: Correlation to various compromised fetuses in utero. *Early Hum Dev* 40: 1–11, 1994
87. Chen Z, Migeon T, Verpont MC, Zaidan M, Sado Y, Kerjaschki D, et al.: HANAC syndrome Col4a1 mutation causes neonate glomerular hyperpermeability and adult glomerulocystic kidney disease. *J Am Soc Nephrol* 27: 1042–1054, 2016
88. Plaisier E, Gribouval O, Alamowitch S, Mougnot B, Prost C, Verpont MC, et al.: COL4A1 mutations and hereditary angiopathy, nephropathy, aneurysms, and muscle cramps. *N Engl J Med* 357: 2687–2695, 2007
89. Morita H, Yoshimura A, Inui K, Ideura T, Watanabe H, Wang L, et al.: Heparan sulfate of perlecan is involved in glomerular filtration. *J Am Soc Nephrol* 16: 1703–1710, 2005
90. Kalluri R, Shield CF, Todd P, Hudson BG, Neilson EG: Isoform switching of type IV collagen is developmentally arrested in X-linked Alport syndrome leading to increased susceptibility of renal basement membranes to endoproteolysis. *J Clin Invest* 99: 2470–2478, 1997
91. Savige J, Gregory M, Gross O, Kashtan C, Ding J, Flinter F: Expert guidelines for the management of Alport syndrome and thin basement membrane nephropathy. *J Am Soc Nephrol* 24: 364–375, 2013
92. Zenker M, Aigner T, Wendler O, Tralau T, Muntefering H, Fenski R, et al.: Human laminin beta2 deficiency causes congenital nephrosis with mesangial sclerosis and distinct eye abnormalities. *Hum Mol Genet* 13: 2625–2632, 2004
93. Abrass CK, Berfield AK, Ryan MC, Carter WG, Hansen KM: Abnormal development of glomerular endothelial and mesangial cells in mice with targeted disruption of the lama3 gene. *Kidney Int* 70: 1062–1071, 2006
94. Braun DA, Warejko JK, Ashraf S, Tan W, Daga A, Schneider R, et al.: Genetic variants in the LAMA5 gene in pediatric nephrotic syndrome. *Nephrol Dial Transplant* 34: 485–493, 2019
95. Abrahamson DR, St John PL, Stroganova L, Zelenchuk A, Steenhard BM: Laminin and type IV collagen isoform substitutions occur in

- temporally and spatially distinct patterns in developing kidney glomerular basement membranes. *J Histochem Cytochem* 61: 706–718, 2013
96. Gara SK, Grumati P, Squarzone S, Sabatelli P, Urciuolo A, Bonaldo P, et al.: Differential and restricted expression of novel collagen VI chains in mouse. *Matrix Biol* 30: 248–257, 2011
 97. Gao X, Eladari D, Leviel F, Tew BY, Miró-Julià C, Cheema FH, et al.: Deletion of hensin/DMBT1 blocks conversion of beta- to alpha-intercalated cells and induces distal renal tubular acidosis [published correction appears in *Proc Natl Acad Sci U S A* 109: 18625, 2012]. *Proc Natl Acad Sci U S A* 107: 21872–21877, 2010
 98. Kostka G, Giltay R, Bloch W, Addicks K, Timpl R, Fässler R, et al.: Perinatal lethality and endothelial cell abnormalities in several vessel compartments of fibulin-1-deficient mice. *Mol Cell Biol* 21: 7025–7034, 2001
 99. Péterfi Z, Donkó A, Orient A, Sum A, Prókai A, Molnár B, et al.: Peroxidasin is secreted and incorporated into the extracellular matrix of myofibroblasts and fibrotic kidney. *Am J Pathol* 175: 725–735, 2009

See related editorial “Too Little or Too Much? Extracellular Matrix Remodeling in Kidney Health and Disease”. on pages 1541–1543.

AFFILIATIONS

¹Weldon School of Biomedical Engineering, Purdue University, West Lafayette, Indiana

²Medical Scientist/Engineer Training Program, Indiana University, Indianapolis, Indiana

³Interdisciplinary Life Science Program, Purdue University, West Lafayette, Indiana

⁴Department of Pediatrics, School of Medicine, Indiana University, Riley Children’s Hospital, Indianapolis, Indiana

⁵Paul M. Rady Department of Mechanical Engineering, University of Colorado Boulder, Boulder, Colorado

Table of contents for supplemental material

Lipp et al., 3D mapping reveals a complex and transient interstitial matrix during murine kidney development

Supplemental Appendix 1: Supplemental Methods

Videos:

Video S1: 10× medullary ray sheath fibers at E14.5, E18.5, and P3 kidneys stained for COL5, COL4, and WGA.

Video S2: 10× medullary ray sheath fibers at E14.5, E18.5, and P3 kidneys stained for COL6, HSPG2, and WGA.

Video S3: 10× medullary ray sheath fibers at E14.5, E18.5, and P3 kidneys stained for POSTN, FREM2, and WGA.

Video S4: 40× medullary ray sheath fibers at E18.5 and P3 kidneys stained for COL5, COL4, and WGA.

Video S5: 25× medullary ray sheath fibers at E14.5, E18.5, and P3 kidneys stained for POSTN, FREM2, and WGA.

Video S6: 40× vertical fibers in the cortex of E14.5, E18.5, and P3 kidneys stained for COL5, COL4, and WGA.

Video S7: 25× fibers in the capsule of E14.5, E18.5, and P3 kidneys stained for POSTN, FREM2, and WGA.

Tables:

Table S1: Raw data supporting the comparison of the matrisome during kidney development.

Table S2: Classifications of proteins based on interstitial matrix, basement membrane, and other.

Table S3: Raw data supporting the comparison of the matrisome between E14.5 kidneys and whole embryos.

Table S4: A common kidney matrisome was observed across different studies.

Table S5: Materials and settings used for imaging the kidney ECM.

Table S6: Definition of non-standard terms used in this manuscript.

Figures:

Figure S1: Flow diagram of the functional classification of proteins as interstitial matrix, basement membrane, and other ECM associated proteins for matrisome identified in this study.

Figure S2: Proteomic analysis showed high reproducibility between the matrisome for biological replicates.

Figure S3: Heat map comparison of the dynamic changes of the matrisome for both the IN and CS fraction.

Figure S4: Scaled LFQ intensity values for the IN fraction for interstitial matrix proteins discussed in the manuscript (COL1A1-FBN1).

Figure S5: Scaled LFQ intensity values for the IN fraction for interstitial matrix proteins discussed in the manuscript (FBN2-POSTN).

Figure S6: Scaled LFQ intensity values for the IN fraction for basement membrane proteins discussed in the manuscript (AGRN-LAMA2).

Figure S7: Scaled LFQ intensity values for the IN fraction for basement membrane proteins discussed in the manuscript (LAMA4-TINAGL1).

Figure S8: Spatiotemporal change of COL5 and COL4 in murine developing kidney.

Figure S9: Representative image of decellularized kidneys from E14.5, E18.5, P3, and adult.

Figure S10: Medullary ray sheath fibers were only found at E18.5 and P3 and contained COL5.

Figure S11: Medullary ray sheath fibers were only found at E18.5 and P3 and contained COL6.

Figure S12: Medullary ray sheath fibers were only found at E18.5 and P3 and contained POSTN.

Figure S13: COL5+ medullary ray sheath fibers were observed in decellularized and SeeDB-cleared kidneys.

Figure S14: Colocalization of COL1 and COL5 in the E18.5 kidney cortex and corticomedullary junction.

Figure S15: COL5+ vertical fibers were observed in the cortex.

Figure S16: COL5+ “rungs of a ladder” fibers were observed in the medulla.

Figure S17: The morphology of interstitial fibers was distinct between cortex and medulla for COL6.

Figure S18: The morphology of interstitial fibers was distinct between the cortex and medulla.

Figure S19: Interstitial accumulations were not observed in the adult mouse kidney.

Supplemental Appendix 1: Supplemental Methods

Tissue collection.

WT C57BL/6J mice were time mated, where embryonic day (E)0.5 refers to noon of the day when the copulation plug was noted. Adult mice and pregnant dams (E14.5, E18.5) were euthanized by CO₂ inhalation and confirmed via cervical dislocation. E18.5 and P3 pups were euthanized using decapitation. For proteomic analysis, P3 and adult mice were perfused with 1× PBS using a cardiac approach to remove blood. Embryos, P3 pups, and adult kidneys were transferred to chilled PBS on ice for fine dissection of the kidney. The ureter, capsule, and renal vein and artery were removed from the kidneys at all timepoints. Tissues to be analyzed for LC-MS/MS were snap-frozen in liquid nitrogen and stored at -80°C until processed. Kidneys for decellularization were processed immediately after harvest (as described below), and those for cryosectioning were embedded in optimal cutting temperature compound (OCT; Electron Microscopy Sciences) and stored at -80°C until cryosections were collected.

Proteomics.

Proteomic isolation method: The proteome from the different cellular compartments were isolated using the protocol developed by the Hynes lab and modified for embryonic tissue using a Compartment Protein Extraction Kit (Millipore EMD).^{1,2} Halt Protease Inhibitor Cocktail (1×, Thermo Scientific) was added to all buffers and PBS and Benzonase/Nuclease B (EMD Millipore, at 1:1000) was added to the nuclear and membrane buffers. The samples were suspended in ice-cold cytosolic buffer (C) at a ratio of 9.5:1 buffer (μL) to wet weight (mg) and homogenized (TissueRuptor, Qiagen). Samples were nutated for 30 minutes at 4°C, 400 μL of the homogenate was then centrifuged for 20 minutes at 21,100 × g at 4°C. The supernatant (C fraction) was snap-frozen and stored at -80°C. The pellet was resuspended in wash (W) buffer at a buffer (μL) to wet

weight (mg) ratio of 19:1, nutated at 4°C for 5 minutes, centrifuged for 20 minutes at $21,100 \times g$ at 4°C, and the supernatant removed.

The pellet was resuspended in nuclear buffer (N) at a buffer (μL) to wet weight (mg) ratio of 4.75:1, nutated at 4°C for 5 minutes, centrifuged for 20 minutes at $21,100 \times g$ at 4°C, and the supernatant collected (N1), snap-frozen and stored at -80. This process was repeated and the supernatant was collected (N2), snap-frozen and stored at -80. The pellet was resuspended in membrane buffer (M) at a buffer (μL) to wet weight (mg) ratio of 4.75:1, nutated at 4°C for 5 minutes, centrifuged for 20 minutes at $21,100 \times g$ at 4°C, and the supernatant collected, snap-frozen and stored at -80. The pellet was then resuspended in cytoskeletal (CS) buffer at a buffer (μL) to wet weight (mg) ratio of 2.38:1, nutated at (room temperature) RT for 20 minutes and centrifuged for 20 minutes at $21,100 \times g$ at 4°C, and the supernatant collected (CS1) snap-frozen and stored at -80°C. The insoluble pellet was washed with the C buffer at a buffer (μL) to wet weight (mg) ratio of 7.13:1 and centrifuged for 20 minutes at $21,100 \times g$ at 4°C, and the supernatant collected (CS2). The insoluble pellet was washed in PBS at a buffer (μL) to wet weight (mg) ratio of 9.5:1 and centrifuged for 20 minutes at $21,100 \times g$ at 4°C, the supernatant discarded and the insoluble pellet snap-frozen and stored at -80°.

Peptide preparation for LC-MS/MS: The CS buffer supernatants were combined (CS1 + CS2), and protein was precipitated in a solution of methanol, chloroform, and HPLC grade water at a ratio of 8 CS solution: 6 methanol: 3 chloroform: 8 water. The mixture was vortexed then centrifuged for 5 minutes at $18,000 \times g$ at RT. The aqueous and organic phases were decanted, and the pellet was dried at RT. Insoluble pellets from the combined CS fractions and insoluble fractions were resuspended in 8M urea in 100mM ammonium bicarbonate (42.1 mg starting wet weight: 50 μL urea/ammonium bicarbonate) and reduced with dithiothreitol (VWR, final concentration

10mM) for at least 2 hours at 37°C with constant agitation. After equilibrating to RT, samples were protected from light while alkylated with iodoacetamide (VWR, final concentration 25mM) for 30 minutes. Samples were diluted to 2M urea with 100mM ammonium bicarbonate and deglycosylated with chondroitinase ABC (Sigma, final concentration 0.2U/200mL for 2 hours at 37°C with constant agitation). Peptidases were added for protein digestion: Endoproteinase LysC (1mg/200mL; New England Biolabs) for 2 hours, MS-grade trypsin (3mg/200mL; ThermoFisher Scientific) overnight, MS-grade trypsin (1.5mg/200mL) for 2 hours, all conducted at 37°C with constant agitation. Trifluoroacetic acid (final concentration 0.1%) was added to inactivate digestion enzymes.

Removal of peptide contaminants and sample preparation: Detergent contamination was removed using 0.5 mL Pierce Detergent Removal Spin Columns (Thermo Fisher Scientific) and a modified manufacturer's protocol: After removal of the storage solution by centrifugation at $1000 \times g$ for 1 minutes, the columns were prepared by washing with 400 mL of PBS and centrifuging at $1000 \times g$ for 1 minutes, repeated 3 times. The digested sample was added to the column, incubated for 2 minutes, and centrifuged at $1000 \times g$ for 2 minutes. Salts were removed with C-18 MicroSpin columns (The NestGroup, Inc.). Columns were prepared with 1 wash of 100 mL of 100% acetonitrile and 2 washes of 100 mL 0.1% trifluoroacetic acid in HPLC-grade water with centrifugation at $500 \times g$ after each wash. Samples were loaded and spun for 8 minutes at $500 \times g$ and 2 minutes at $750 \times g$ or until flow through was complete. After the addition of 100 mL 0.1% trifluoroacetic acid in HPLC-grade water and centrifugation at $500 \times g$ for 1 minutes, repeated twice, samples were eluted with 50 mL of 80% acetonitrile/25mM formic acid). Peptides were dried at 45°C for 4 hours in a CentriVap vacuum concentrator (Labconoco). To standardize the peptide loading, the peptide concentration was measured at 480 nm using a Pierce Quantitative

Colorimetric Assay (Thermo Fischer Scientific) and Spectra Max M5 (Molecular Devices) and normalized with addition of 3% acetonitrile/0.1% formic acid, to a final concentration of 0.5 mg/mL for CS and IN fractions.

LC-MS/MS analysis: Samples were processed with a Dionex UltiMate 3000 RSLC Nano System coupled to the Q Exactive™ HF Hybrid Quadrupole-Orbitrap Mass Spectrometer (ThermoFisher Scientific). 1 mg of peptide was loaded onto a 300mm i.d. × 5mm C18 PepMap 100 trap column. The peptides were washed for 5 minutes flow rate of 5 mL/minute using 98% purified water/2% acetonitrile/0.01% formic acid. The peptides were then processed using a 75 mm × 50 cm reverse-phase Acclaim C18 PepMap 100 analytical column at 50°C. The peptides were separated on the C18 HPLC system using a 120-minute gradient elution method at a flow rate of 300 nL/minute. Mobile phase A was composed of 0.01% formic acid in water. Mobile phase B comprised of 0.01% formic acid in 80% acetonitrile. Using a linear gradient, the solution was changed from between 2% at time 0, 10% B at 5 minutes, 30% B at 80 minutes, 45% B at 91 minutes, and 100% B at 93 minutes. Between 93 and 98 minutes, the column was held at 100% B. Finally, the solution was changed to 2% B and held for 20 minutes. After HPLC separation, Samples were injected into the Q Exactive HF mass spectrometer through the Nanospray Flex Ion Source fitted with an emission tip (New Objective). With an injection time of 100 ms, the top 20 precursors at 120,000 resolution were monitored.

LC-MS/MS Analyses: Mass spectrometry analysis followed.¹ Peaks from the raw file were analyzed by MaxQuant^{3,4} (version 1.6.7.0) with settings shown in Table S1 against a FASTA database for *Mus musculus* (downloaded 12/06/2019) with canonical variants and contaminants. Fixed modifications of cysteine carbamidomethylation and variable modifications of oxidation of methionine, hydroxylysine, hydroxyproline, deamidation of asparagine, and conversion of

glutamine to pyro-glutamic acid were used.¹⁴ Match-between-runs was used for biological replicates of the same fraction. A decoy database derived from the *Mus musculus* database was used to control the false discovery rate (FDR) to 1%. LFQ was enabled for biological replicates.

Imaging.

Dissection images: A Leica M80 stereomicroscope (Leica Microsystems) was used to acquire wide-field images of dissected kidneys.

Immunohistochemistry (IHC): Cryosections of murine kidneys from E14.5, E18.5, P3, and adult timepoints were acquired at 10 μ m thickness using a Shandon Cryotome FE (Thermo), collected on charged slides, and stored at -20°C until processed for IHC.

Incubations were conducted at RT unless indicated otherwise, and samples were protected from light when fluorescent secondary staining reagents were used. After tissues were equilibrated to RT, kidney sections were encircled with an ImmEdge pen (Vector Laboratories). The samples were rehydrated in PBS for 10-15 minutes, fixed in 4% paraformaldehyde (PFA; Electron Microscopy Sciences) for 5 minutes, and rinsed in PBS. Sections were blocked for 1 hour with IgG blocking buffer from the Mouse on Mouse (MOM) basic kit (Vector Laboratories) following manufacturer's instructions, rinsed 3 \times 2 minutes with PBS, and blocked for 5 minutes with protein diluent from the MOM basic kit. Slides were incubated with primary antibodies (Table S5) in a solution of MOM protein diluent overnight at 4°C, then washed 3 \times 2 minutes with 1 \times PBS. Secondary antibodies, stains, and DAPI (Table S5) were applied to sections in a solution of MOM protein diluent for 45 minutes. Slides were rinsed 3 \times 2 minutes with 1 \times PBS and tissue was mounted using FluoromountG (Electron Microscopy Sciences) and #1.5 coverslips, and sealed using clear nail polish. Slides were stored at 4°C until imaged with a Leica DMI6000 at 20 \times

magnification. Negative controls consisted of the same processing with the exclusion of the primary antibodies. Images are representative of ≥ 2 biological replicates for 2 litters.

3D imaging of decellularized kidneys: Kidneys were processed for 3D imaging of the ECM using protocols modified from.⁵ Depending on the timepoint, dissected kidneys were either directly incubated in SDS solution or embedded in agarose to improve tissue stability (Table S5). The adult timepoint was represented with P28 – P56 kidneys due to more optimum decellularization when the tissues are smaller and as stromal cell accumulations disappear by P28.⁶ Low melt agarose (Sigma Aldrich) was suspended in Milli-Q water with 0.02% sodium azide (see concentrations in Table S5), melted and equilibrated to a 37°C water bath and then used to embed the kidney in a cryomold (Tissue-Tek). After equilibrating and solidifying at RT, the agarose embedded samples were transferred to an SDS solution (concentrations, volumes indicated in Table S5). The samples were gently rocked at RT, with daily changes of the SDS solution. Once decellularized, the samples were washed with 1× PBS for 1 hour at RT with rocking. The samples were fixed for 1 hour in 4% PFA in PBS at RT or overnight at 4°C with rocking and washed with 1× PBS for 1 hour RT or 4°C overnight with rocking. Samples were stored in 1× PBS at 4°C until staining. After excess agarose was removed, the samples were transferred to a 96 well plate (volume 150 μ L), permeabilized and blocked overnight at 4°C with 10% donkey serum (Lampire Biological Laboratories) and 0.02% sodium azide (Sigma Aldrich) in 0.1% PBST (0.1% Triton-X 100 in 1× PBS). The primary antibodies were diluted to concentrations indicated in Table S5 in 0.2% bovine serum albumin (BSA; Sigma Aldrich) and 0.02% sodium azide in 1× PBS and were added to the sample for 48 hours at 4°C with gentle rocking. After washing for 3 \times 30 minutes in 0.1% PBST at RT, the sample was incubated in stains and secondary antibody combinations (Table S5) diluted in 0.2% BSA and 0.02% sodium azide in 1× PBS at 4°C for 48 hours with gentle

rocking while protected from light. To provide a general outline of kidney ECM architecture, samples were counterstained with AF488 or AF647-conjugated wheat germ agglutinin (WGA), which stains a subset of proteoglycans. The samples were washed 3×30 minutes in 0.1% PBST at RT and stored in PBS at 4°C with protection from light until imaged.

SeeDB clearing of kidneys. Fresh kidneys were fixed in 4% PFA in $1 \times$ PBS for 1 hour at RT or overnight at 4°C, washed with PBS with rocking 1 hour at RT or overnight at 4°C, and stored in fresh $1 \times$ PBS. Samples were permeabilized and blocked overnight at 4°C with 10% donkey serum and 0.02% sodium azide in 0.1% PBST. The primary antibodies were diluted to concentrations indicated in Table S5 in 0.2% BSA and 0.02% sodium azide in $1 \times$ PBS and were added to the sample for 48 hours at 4°C with gentle rocking. After washing for 3×30 minutes in 0.1% PBST at RT, samples were incubated in stains and secondary antibody combinations (Table S5) diluted in 0.2% BSA and 0.02% sodium azide in $1 \times$ PBS at 4°C for 48 hours with gentle rocking while protected from light. The samples were washed 3×30 minutes in 0.1% PBST at RT and stored in PBS at 4°C with protection from light. Kidneys were incubated in fructose solutions of increasing concentration diluted in $0.1 \times$ PBS and 0.5% thioglycerol. Specifically, 20%, 40% and 60% fructose (weight /volume) for 4-12 hours each, 80% and 100% for 12-24 hours, and 115% fructose for 24 hours twice. Samples were stored at RT until imaging.

Confocal imaging: For imaging, decellularized kidneys were placed in a dish (Ibidi) and suspended in $1 \times$ PBS at an optimal level that would avoid both dehydration (inverted confocal) and excessive movement or adhered to the bottom of the dish with 1% low melt agarose (upright confocal). SeeDB cleared kidneys were placed in a dish with the 115% fructose solution and covered with a coverslip. Kidneys imaged at $40\times$ and $63\times$ were stabilized by bisecting kidneys and wedging the tissue between blocks of 1% agarose. Kidneys were imaged using a Zeiss LSM 880

inverted confocal microscope (Carl Zeiss Microscopy) with Zen 2.3 SP1 black software (V14.0.2.201) or Leica DM6 CFS stellaris upright confocal (Leica Microsystems) with LAS X software (V4.1.1.23273). Samples were imaged with settings in Table S5. Laser power and gain were optimized for each sample to improve visualization of the ECM. Negative controls consisted of the same process without the addition of the primary antibody and were imaged at the maximum settings for the antibody channels. Images in figures are representative of a minimum of $n = 3$ biological replicates from a minimum of 2 litters.

Image processing: Widefield images and cryosections were processed using FIJI (NIH).⁷ Cryosection image intensity was optimized per time point to improve visualization (Figure 5) or with the same settings across samples (Figure S8). Confocal z-stacks were processed using nearest-neighbor deconvolution in Zen Blue software (V2.3.64.0; Carl Zeiss Microscopy) using fast settings or LAS X software (4.1.1.23273; Leica Microsystems) using default settings with the following changes: global, optimization = 0.1, cut off = 0, regularization = 0.005, smoothing = high, and coverslip thickness = 0 or coverslip thickness = 0.17 mm. In FIJI, cleared tissues were further processed using bleach correction (setting: exponential fit) to increase the signal intensity with depth, if sample intensity decayed.⁸ Kidney z-stacks were visualized using FIJI 3D viewer.⁹ Renderings of wide-field images, cryosections, and decellularized tissue were compiled using Adobe Photoshop and Illustrator.

Statistical analyses: Analysis of ECM sub-cellular compartments included a two-way ANOVA (factors: fraction and tissue type) with and Tukey or Sidak's multiple comparisons test between tissues with a significance cut-off of $\alpha < 0.05$. ECM functional classifications studied the factor of tissue with a one-way ANOVA and subsequent Tukey multiple comparisons test or unpaired, two tailed t-test with a significance cut-off of $\alpha < 0.05$. To determine if individual

proteins in the IN fraction changed over time or with tissue type, one-way ANOVA was performed for data identified in 3-4 timepoints. The data was analyzed using untransformed values if the Brown-Forsythe test for equal standard deviation and the Shapiro Wilk Normality assumptions were met. Log₂ transformed data was used if Brown-Forsythe test for equal standard deviation and the Shapiro Wilk normality assumptions were met when the data were transformed. If assumptions were not met, untransformed data was used.¹⁰ Values identified at 2 timepoints were compared using an un-paired two-tailed student t-test using scaled untransformed data if the F-test for variance and Shapiro Wilk test for normality were met. If the assumptions were not met, the values were log₂ transformed if the F-test for variance and Shapiro Wilk test for normality were met using the log₂ transform data. If both assumptions were not met, untransformed data was used.¹⁰ Significance was determined using a *p* cut-off of $\alpha < 0.05$. For volcano plot comparisons, Tukey comparisons between all timepoints were performed if identified in 3 or 4 timepoints or un-paired two-tailed student t-test if identified in 2 timepoints. The scaled or log₂ transformed data was used based on the assumptions above. Proteins were defined as transiently elevated if a middle timepoint (E18.5 or P3) was significantly higher than an earlier and later timepoint. Imputation was avoided as it negatively affects high abundance proteins in statistical analyses.¹¹

Videos:

Video S1: 10× medullary ray sheath fibers at E14.5, E18.5, and P3 kidneys stained for COL5, COL4, and WGA. 3D renderings and sequential sections of E14.5, E18.5, and P3 kidneys from Figure 7 showed medullary ray sheath fibers. Cortical to the medullary ray sheath fibers were tubules, glomeruli, and the articular artery. 10× confocal z-stacks ($x \times y$) 1.42 mm \times 1.42 mm. 3D rendering: $z = 100 \mu\text{m}$, movies of sequential sections: E14.5, $z = 576 \mu\text{m}$; E18.5 and P3, $z = 384 \mu\text{m}$.

Video S2: 10× medullary ray sheath fibers at E14.5, E18.5, and P3 kidneys stained for COL6, HSPG2, and WGA. 3D renderings and sequential sections of E14.5, E18.5, and P3 kidneys from Figure 7 showed medullary ray sheath fibers. Cortical to the medullary ray sheath fibers were tubules, glomeruli, and the articular artery. 10× confocal z-stacks ($x \times y$) 1.42 mm \times 1.42 mm. 3D renderings: $z = 100 \mu\text{m}$, movies of sequential sections: E14.5, $z = 307 \mu\text{m}$; E18.5 μm and P3, $z = 384 \mu\text{m}$.

Video S3: 10× medullary ray sheath fibers at E14.5, E18.5, and P3 kidneys stained for POSTN, FREM2, and WGA. 3D renderings and sequential sections of E14.5, E18.5, and P3 kidneys from Figure 7 showed medullary ray sheath fibers. Cortical to the medullary ray sheath fibers were tubules, glomeruli, and the articular artery. 10× confocal z-stacks ($x \times y$) 1.48 mm \times 1.48 mm. 3D rendering: $z = 148 \mu\text{m}$, movies of sequential sections: E14.5, $z = 627 \mu\text{m}$; E18.5 and P3, $z = 570 \mu\text{m}$.

Video S4: 40× medullary ray sheath fibers at E18.5 and P3 kidneys stained for COL5, COL4, and WGA. 3D renderings and sequential sections of E18.5 and P3 kidneys from Figure 7 showed medullary ray sheath fibers surrounding the developing loop of Henle and collecting duct. 40×: $354 \times 354 \times 45 \mu\text{m}$ for 3D renderings and movies of sequential sections.

Video S5: 25× medullary ray sheath fibers at E14.5, E18.5, and P3 kidneys stained for POSTN, FREM2, and WGA. 3D renderings and sequential sections of E14.5, E18.5, and P3 kidneys from Figure 7 and S17 showed medullary ray sheath fibers surrounding the developing loop of Henle and collecting duct. 25× confocal z-stacks ($x \times y$) $345 \times 345 \mu\text{m}$. 3D renderings: $z = 57 \mu\text{m}$, movies of sequential sections: E14.5, $z = 230 \mu\text{m}$; E18.5 μm and P3, $z = 57 \mu\text{m}$.

Video S6: 40× vertical fibers in the cortex of E14.5, E18.5, and P3 kidneys stained for COL5, COL4, and WGA. 3D renderings of E14.5, E18.5, and P3 kidneys from Figure 8 showed vertical fibers surrounding the nephrogenic zone. 40×: $354 \times 354 \times 45 \mu\text{m}$ for 3D renderings.

Video S7: 25× fibers in the capsule of E14.5, E18.5, and P3 kidneys stained for POSTN, FREM2, and WGA. 3D renderings and sequential sections of E14.5, E18.5, and P3 kidneys from Figure S17 showed fibers in the capsule stained for POSTN near the nephrogenic zone. 25×: $345 \times 345 \times 57 \mu\text{m}$ for 3D renderings and movies of sequential sections.

Tables:

Table S1: Raw data supporting the comparison of the matrisome during kidney

development. The table includes the following: the number of kidneys isolated for mass spectrometry; MaxQuant settings; proteins identified and calculation of cellular compartment and ECM functional classifications; proteins identified for Venn diagram and heat map values; proteins significantly changed or exclusively found at different timepoints; and GO analysis terms.

Table S3: Raw data supporting the comparison of the matrisome between E14.5 kidneys and

whole embryos. The table includes the following: proteins identified and calculation of cellular compartment and ECM functional classifications; proteins significantly changed or exclusively found in whole embryo or kidney; GO analysis terms; and Venn diagram proteins comparison between kidney, embryo, brain, and forelimb at E14.5.

Table S4: A common kidney matrisome was observed across different studies.

Comparison of matrisome proteins observed in our study to other kidney matrisome studies showed there was a common set of ECM proteins. Some proteins were found only during development, in the glomerulus, renal artery, or kidney culture models.

Table S5: Materials and settings used for imaging the kidney ECM.

The table includes the following: optimized tissue processing for decellularization; antibodies and stains used for immunohistochemistry, decellularization, and SeeDB staining; 3D imaging specifications, settings, and locations; and summary of staining patterns observed in immunohistochemistry and decellularization.

Table S6: Definition of non-standard terms used in this manuscript. Terms in italics refer to single cell –RNA sequencing clusters of kidney stromal cells from the E18.5 mouse kidney determined in *England et al., 2020*¹²

	Description	Stromal cell structure	Tubular structure
vertical fibers	<p>fibers in the cortex originating from the capsule extending into the nephrogenic zone and fibers extending from the medullary rays into the cortex</p> <p>described as interdigitations¹³</p> <p>fibers appear to be distinct from the fibers that connect the ampule the capsule¹⁴</p>	<i>cortical interstitium</i> ¹² <i>nephrogenic interstitium</i> ¹²	nephrogenic zone
medullary ray sheath fibers	<p>fibers near the corticomedullary junction that surround the medullary rays (loop of Henle, collecting duct, vasa recta)</p>	<p>medullary ray sheath/ fascicles¹⁵ embryonic connective tissue⁶ interstitial spaces/ interstitial¹⁶ primary interstitium¹⁷</p> <p><i>proximal tubule interstitium</i>¹² <i>interstitium medullary to proximal tubule (outer medulla)</i>¹² <i>outer stripe of inner medulla interstitium</i>¹²</p>	tubule- vascular units ⁶
“rungs of a ladder” fibers	<p>fibers connecting the loop of Henle, collecting duct and vasa recta in the medulla</p>	<p>“rungs of a ladder” interstitial cells¹⁶</p> <p><i>papillary interstitium</i>¹²</p>	collecting duct and loop of Henle

Figures:

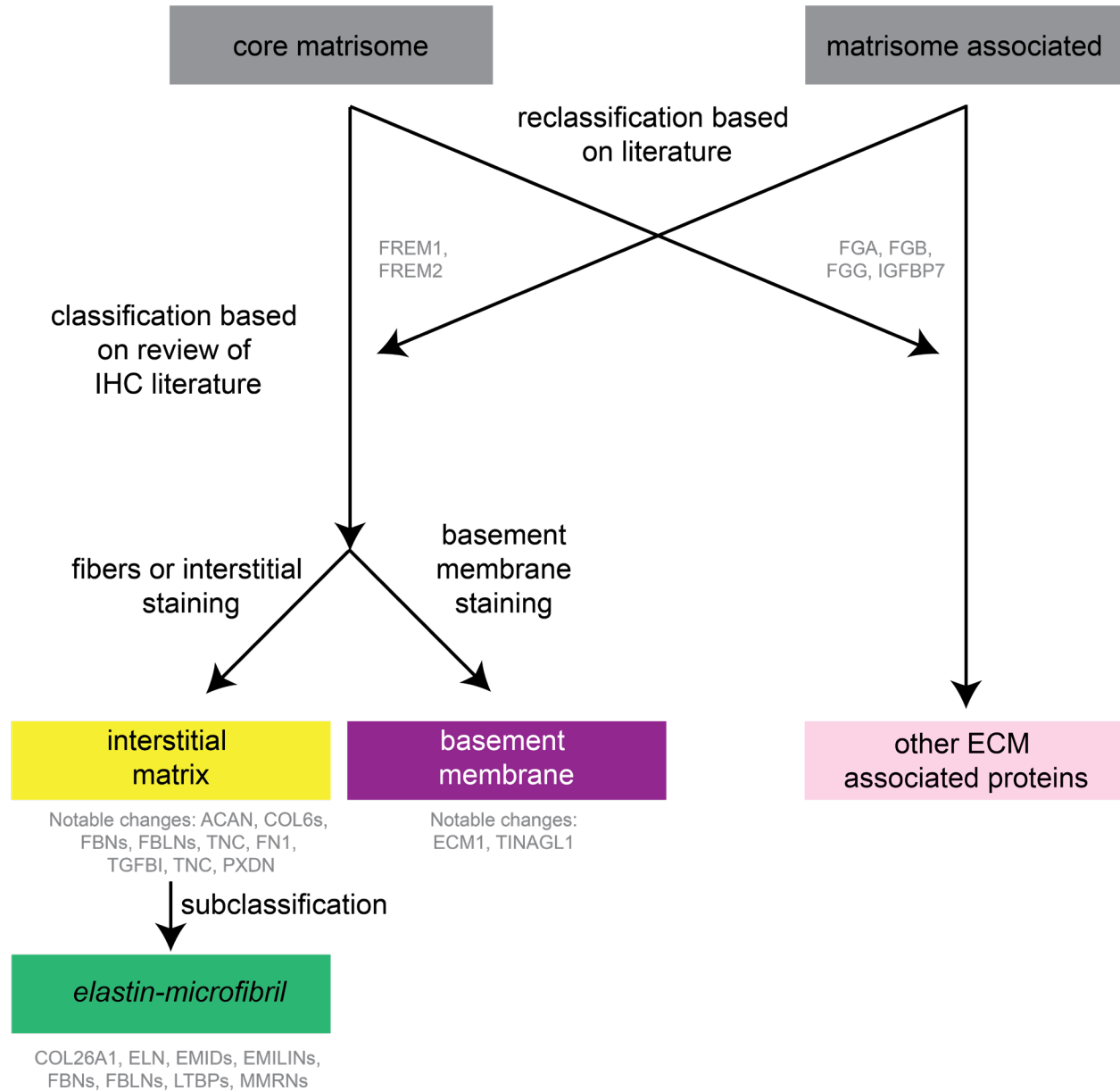


Figure S1: Flow diagram of the functional classification of proteins as interstitial matrix, basement membrane, and other ECM associated proteins for matrisome identified in this study. In general, core matrisome proteins were either classified as interstitial matrix or basement membrane, while matrisome-associated proteins were classified as other except for the reclassification of FREM1 and FREM2 as basement membrane proteins. Baseline classifications

were modified based on review of the literature (Table S2).¹⁸⁻²⁰ If fibers are described (*e.g.* FBN1, TNC, COL6, FN1), the proteins were classified as interstitial matrix (defined as a loose network comprised of fibril-forming ECM found between kidney tubules). The interstitial matrix was subclassified as *elastin-microfibril axis* based on the literature.²¹⁻³³ If described as basement membrane, basement membrane interface, or displayed a linear staining pattern surrounding tubules, the protein was annotated as basement membrane (defined as a dense meshwork surrounding the nephron tubule).

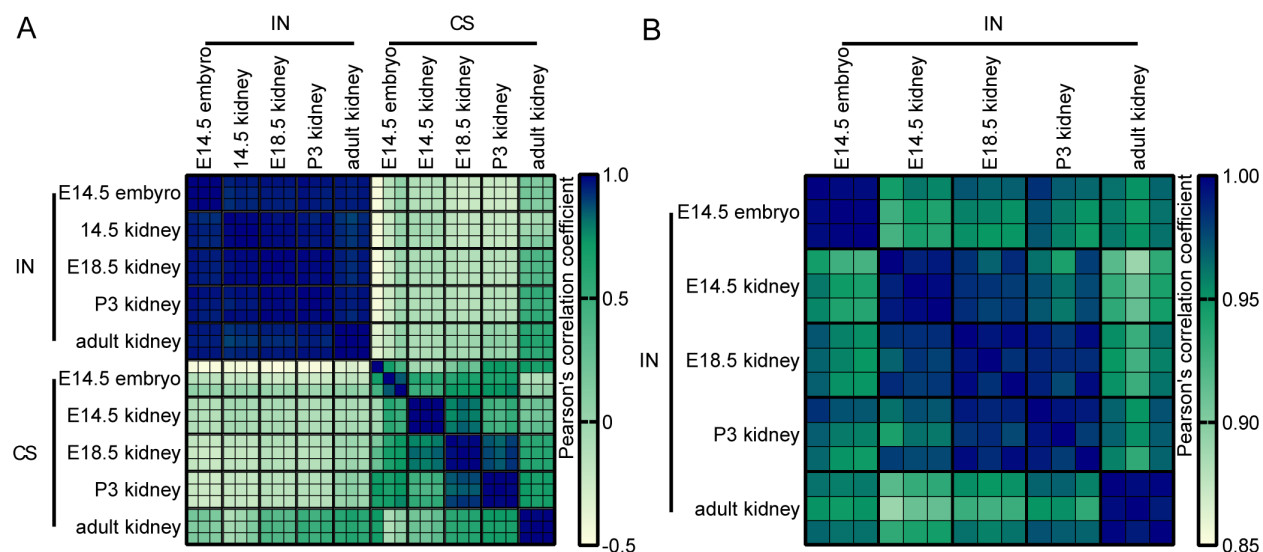
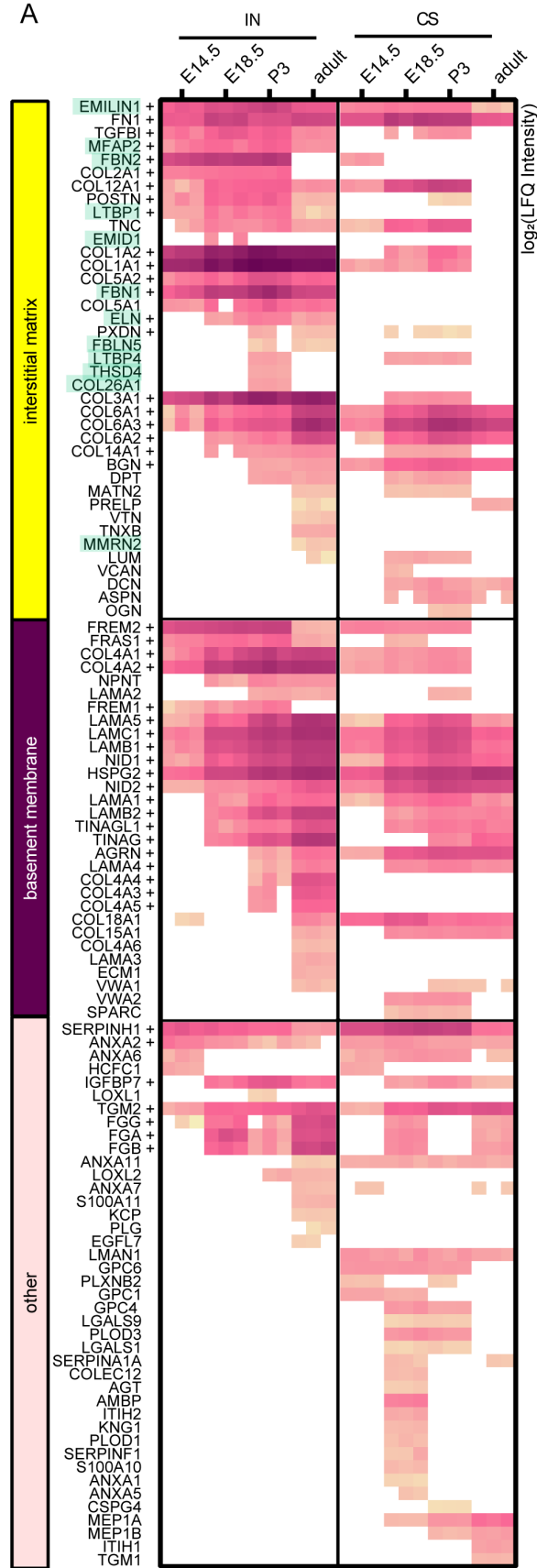


Figure S2: Proteomic analysis showed high reproducibility between the matrisome for biological replicates. (A) Comparison of Pearson's correlation coefficients for E14.5, E18.5, P3, adult murine kidneys, and E14.5 whole embryos using scaled LFQ values for matrisome proteins. (B) Inset of A focusing on the IN fraction ($n = 3$ biological replicates per timepoint). Between biological replicates, the Pearson's correlation coefficients were close to 1, indicating the reproducibility of the method, whereas there was greater variation between timepoints.

A



B

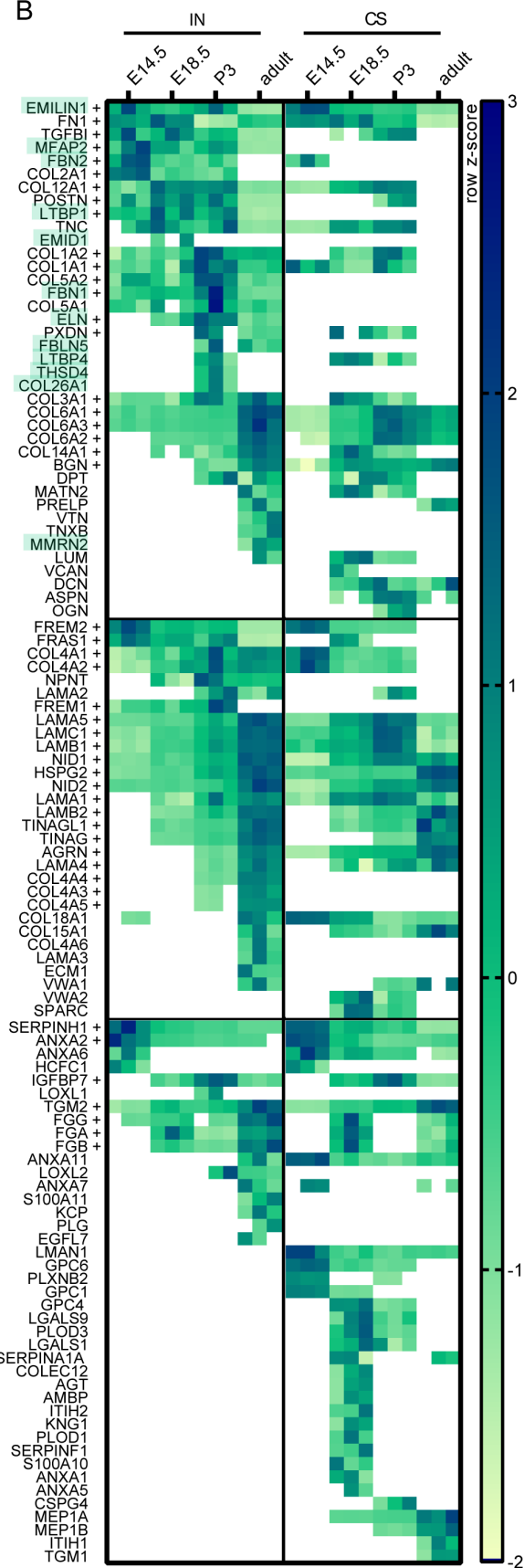


Figure S3: Heat map comparison of the dynamic changes of the matrisome for both the IN and CS fraction. (A) The raw intensity of ECM proteins was higher in the IN compared to the CS fraction. (B) Row z-score heatmap comparison of IN and CS fractions, based on scaled LFQ intensity, showed similar trends in protein expression. Heat maps were manually clustered based on classification as interstitial matrix, basement membrane, or other ECM associated proteins. *Elastin-microfibril axis* proteins are highlighted in green. + indicates $p < 0.05$ for proteins identified in the IN fraction based on one-way ANOVA (identified in 3 - 4 timepoints) or unpaired, two tailed t-test (identified in 2 timepoints). Proteins identified in $n \geq 2$ biological replicates per timepoint were included in the heat map analysis. White boxes signify zero intensity values.

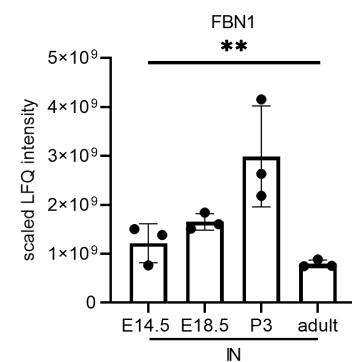
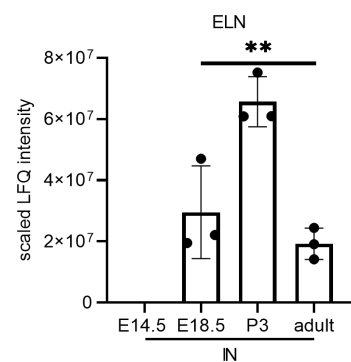
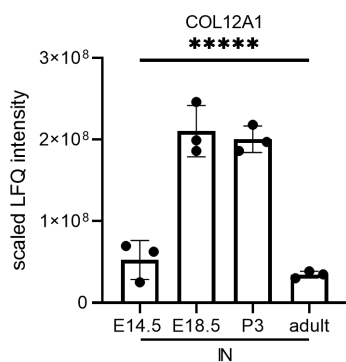
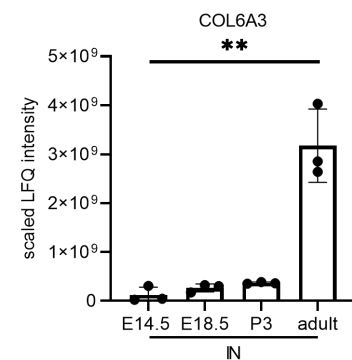
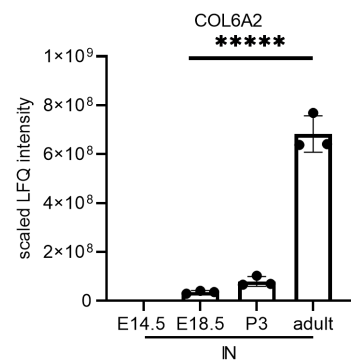
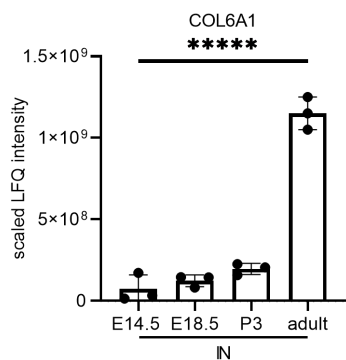
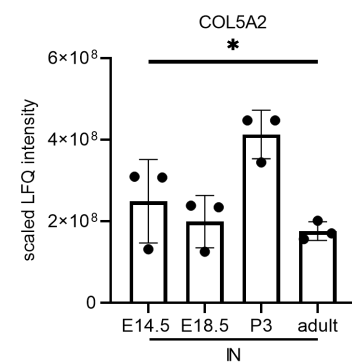
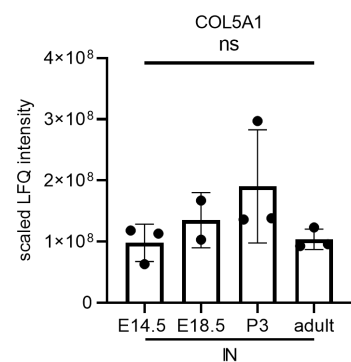
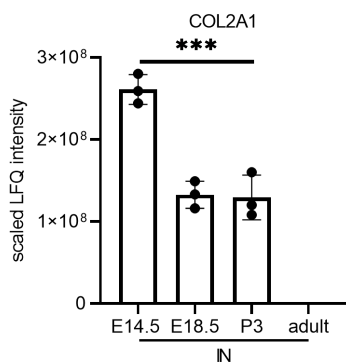
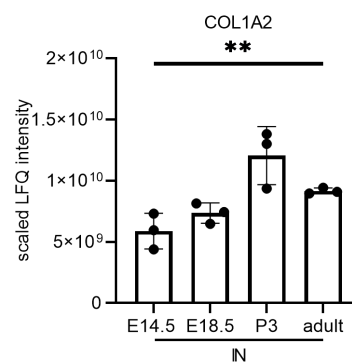
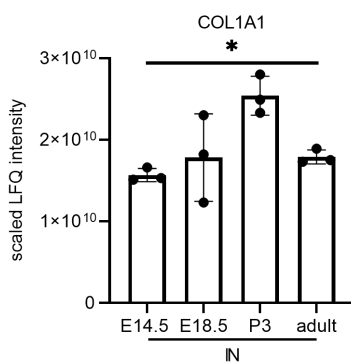
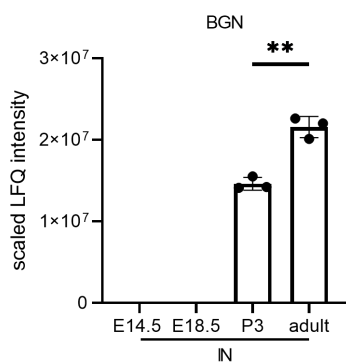


Figure S4: Scaled LFQ intensity values for the IN fraction for interstitial matrix proteins discussed in the manuscript (COL1A1-FBN1). The significance of change in scaled LFQ intensity was determined by one-way ANOVA and is indicated on the graph as follows: $p < 0.05$ = *, $p < 0.01$ = **, $p < 0.001$ = ***, $p < 0.0001$ = ****, $p < 0.00001$ = *****, and non-significant = ns. Tukey comparisons between timepoints are found in Table S1.

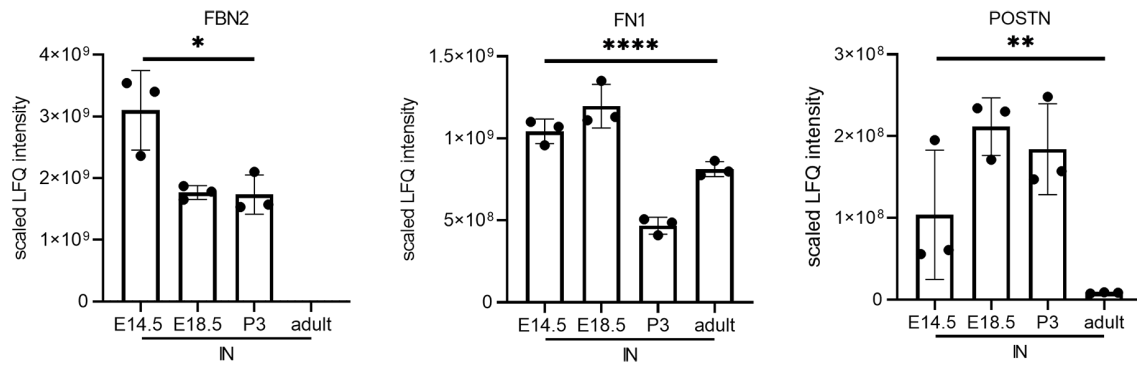


Figure S5: Scaled LFQ intensity values for the IN fraction for interstitial matrix proteins discussed in the manuscript (FBN2-POSTN). The significance of change in scaled LFQ intensity was determined by one-way ANOVA and is indicated on the graph as follows: $p < 0.05$ = *, $p < 0.01$ = **, $p < 0.001$ = ***, $p < 0.0001$ = ****, $p < 0.00001$ = *****, and non-significant = ns. Tukey comparisons between timepoints are found in Table S1.

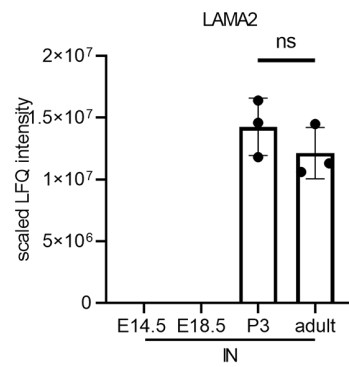
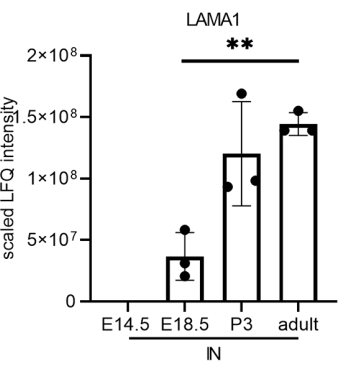
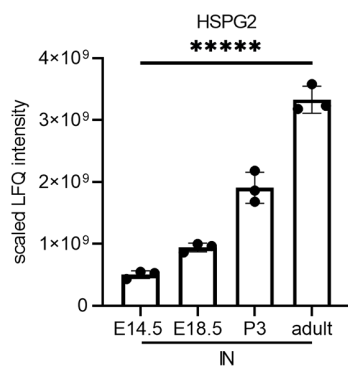
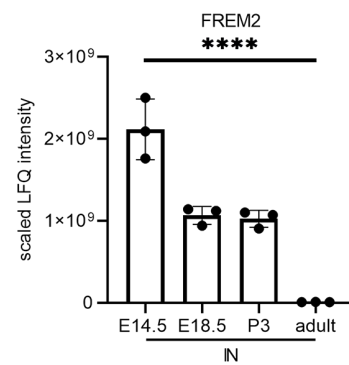
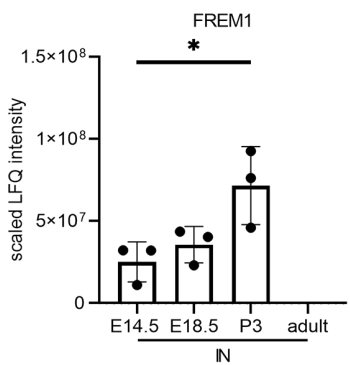
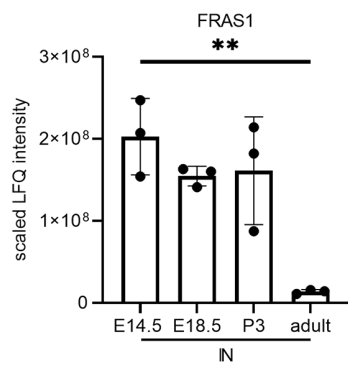
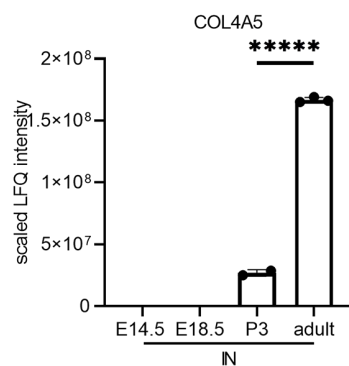
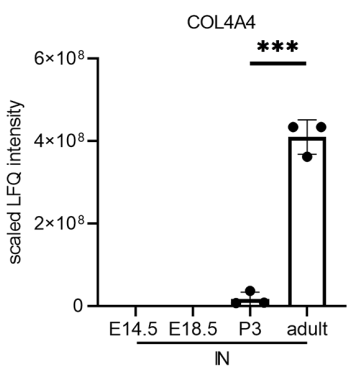
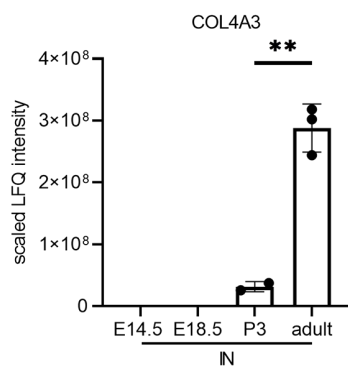
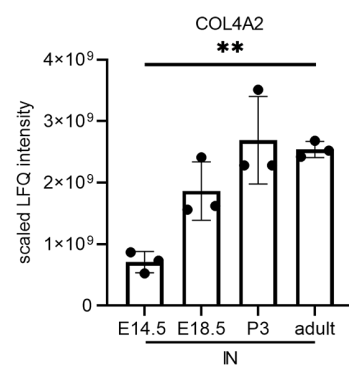
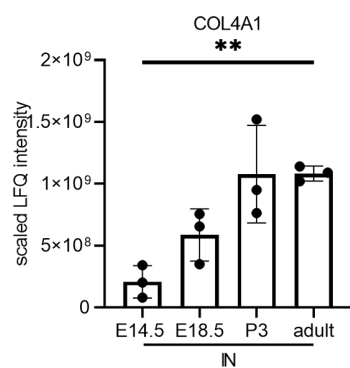
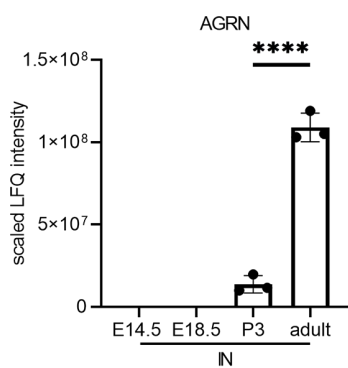


Figure S6: Scaled LFQ intensity values for the IN fraction for basement membrane proteins discussed in the manuscript (AGRN-LAMA2). The significance of change in scaled LFQ intensity was determined by one-way ANOVA and is indicated on the graph as follows: $p < 0.05$ = *, $p < 0.01$ = **, $p < 0.001$ = ***, $p < 0.0001$ = ****, $p < 0.00001$ = *****, and non-significant = ns. Tukey comparisons between timepoints are found in Table S1.

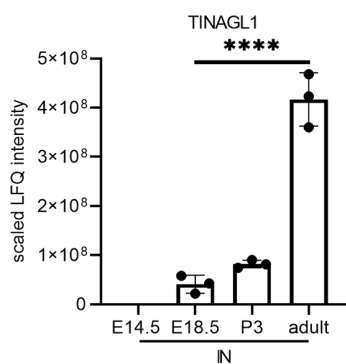
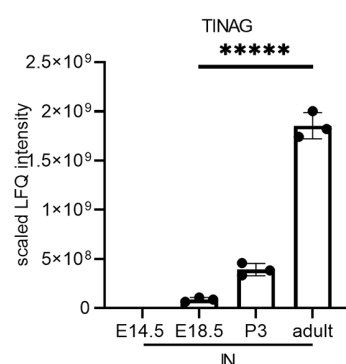
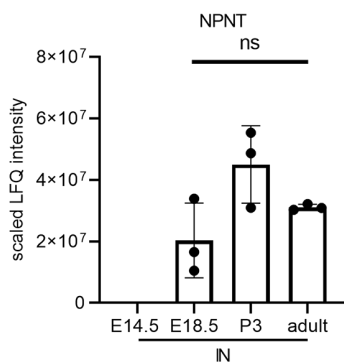
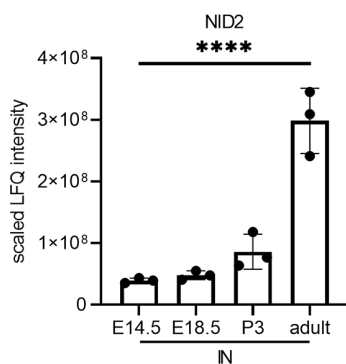
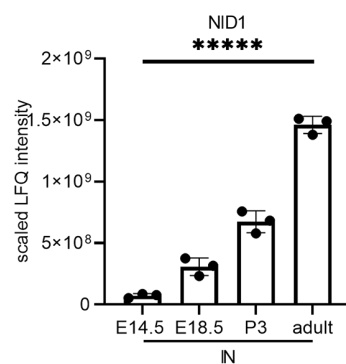
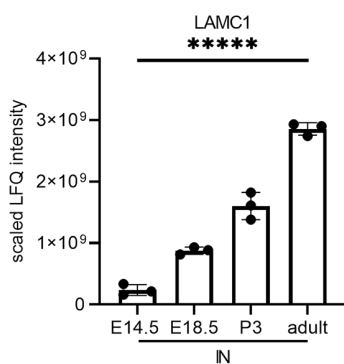
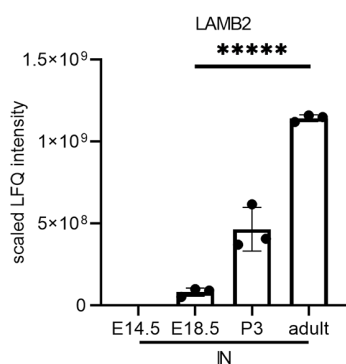
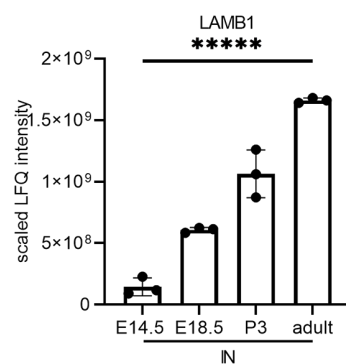
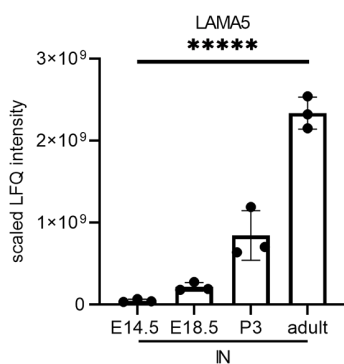
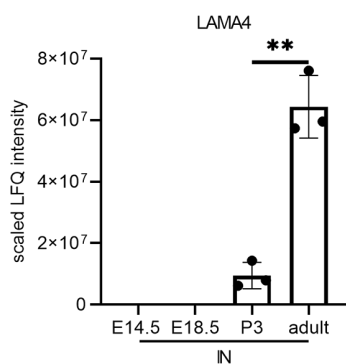


Figure S7: Scaled LFQ intensity values for the IN fraction for basement membrane proteins discussed in the manuscript (LAMA4-TINAGL1). The significance of change in scaled LFQ intensity was determined by one-way ANOVA and is indicated on the graph as follows: $p < 0.05$ = *, $p < 0.01$ = **, $p < 0.001$ = ***, $p < 0.0001$ = ****, $p < 0.00001$ = *****, and non-significant = ns. Tukey comparisons between timepoints are found in Table S1.

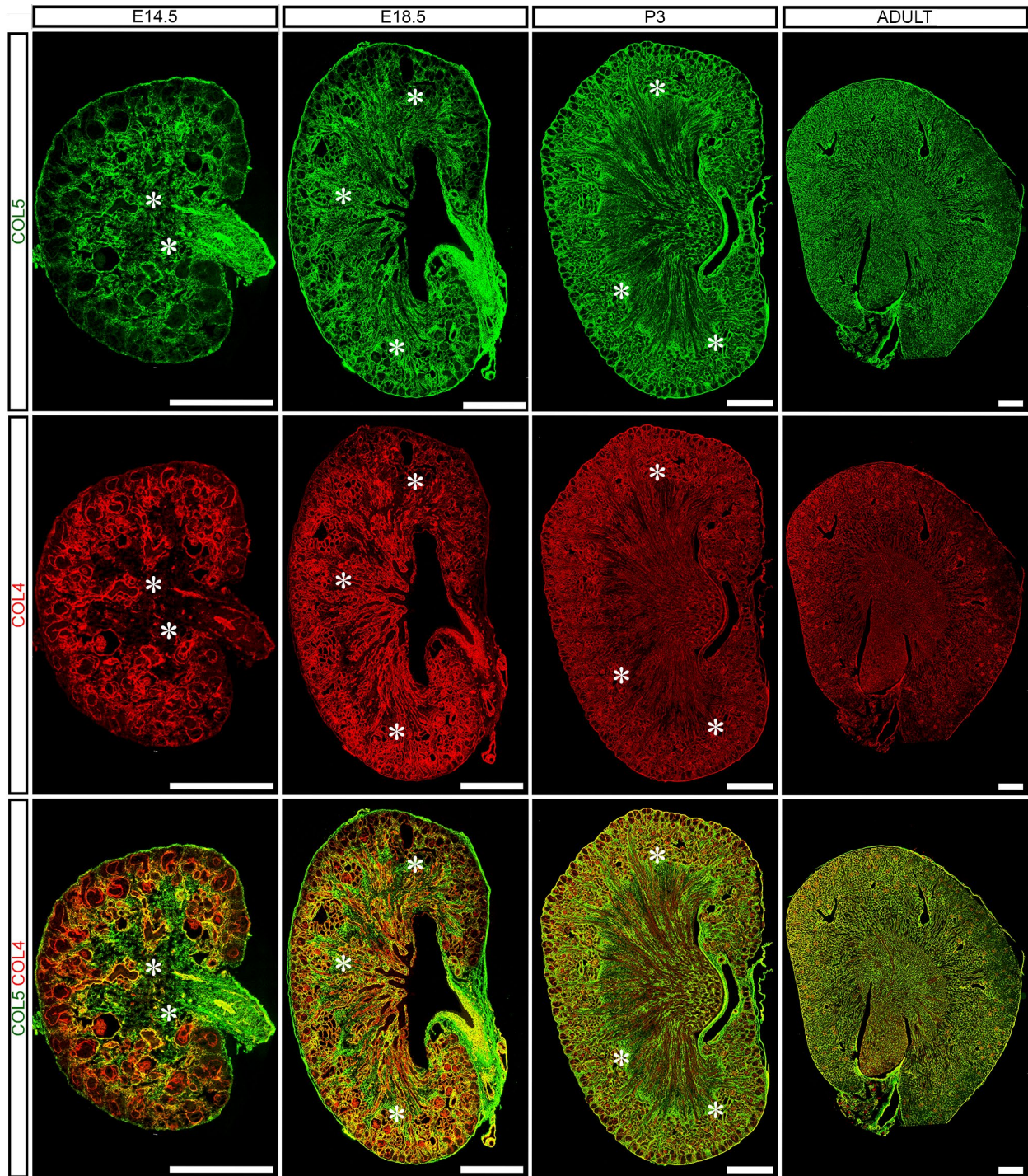


Figure S8: Spatiotemporal change of COL5 and COL4 in murine developing kidney.

Cryosections of E14.5 – adult kidneys showed a decrease in interstitial matrix space and medullary ray sheath fibers (*; green = COL5) and a corresponding increase in basement membrane area (red = COL4). Scale bars = 500 μ m. Representative images from $n = 2$ biological replicates.

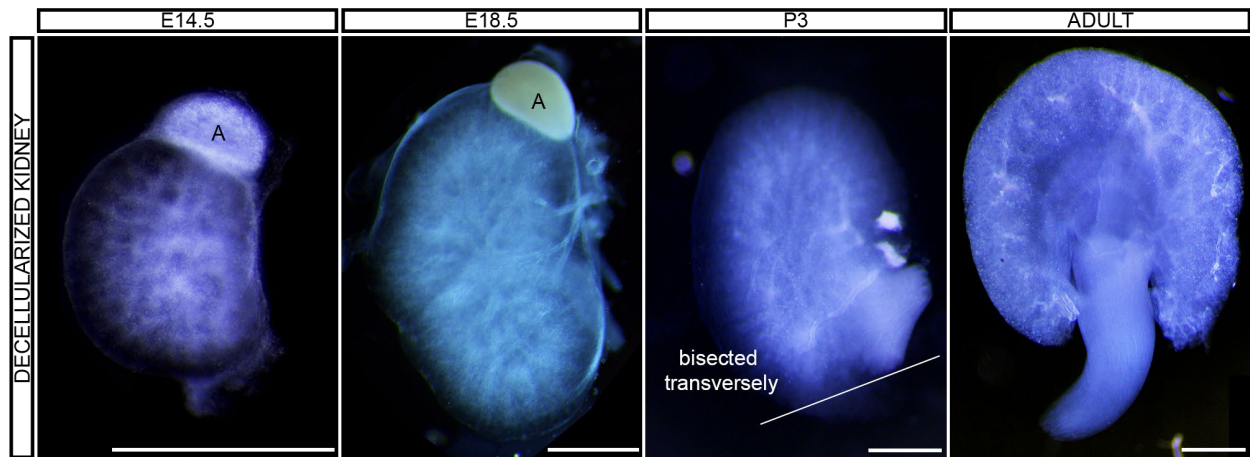


Figure S9: Representative image of decellularized kidneys from E14.5, E18.5, P3, and adult.

A = adrenal gland, Scale bars = 1 mm.

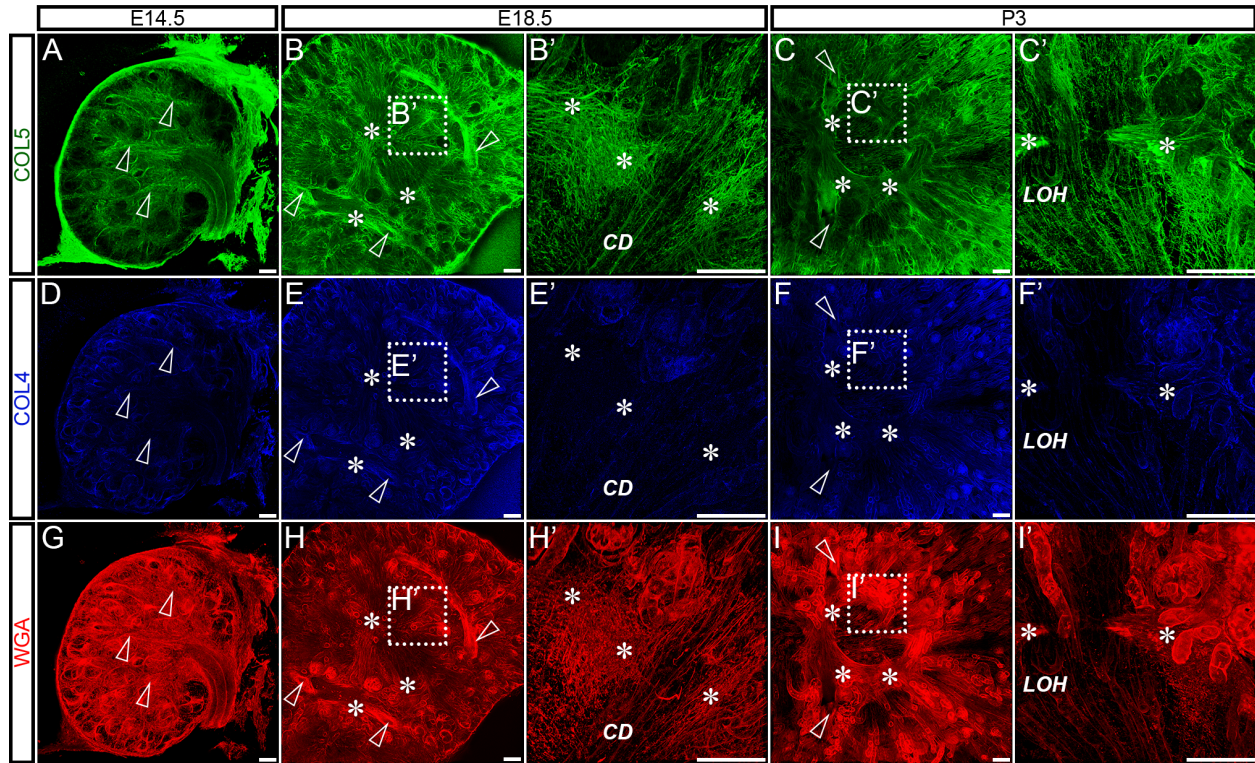


Figure S10: Medullary ray sheath fibers were only found at E18.5 and P3 and contained COL5. (A, D, G) At E14.5, a fibrous ECM (green = COL5) ran parallel to developing blood vessels (open arrowheads) and surrounded tubules (blue = COL4, red = WGA). (B, B', C, C', E, E', F, F', H, H', I, I') Medullary ray sheath fibers (*) surrounded the developing nephron (*CD* = collecting duct, *LOH* = loop of Henle) at E18.5 – P3. Boxes indicate where representative inset at a higher magnification was obtained. Scale bars = 100 μm . Dimensions of confocal z-stacks in A-I (10 \times): 1.42 mm \times 1.42 mm \times 100 μm ($x \times y \times z$); B', C', E', F', H', I' (40 \times): 354 \times 354 \times 45 μm . Representative images from $n = 3$ biological replicates.

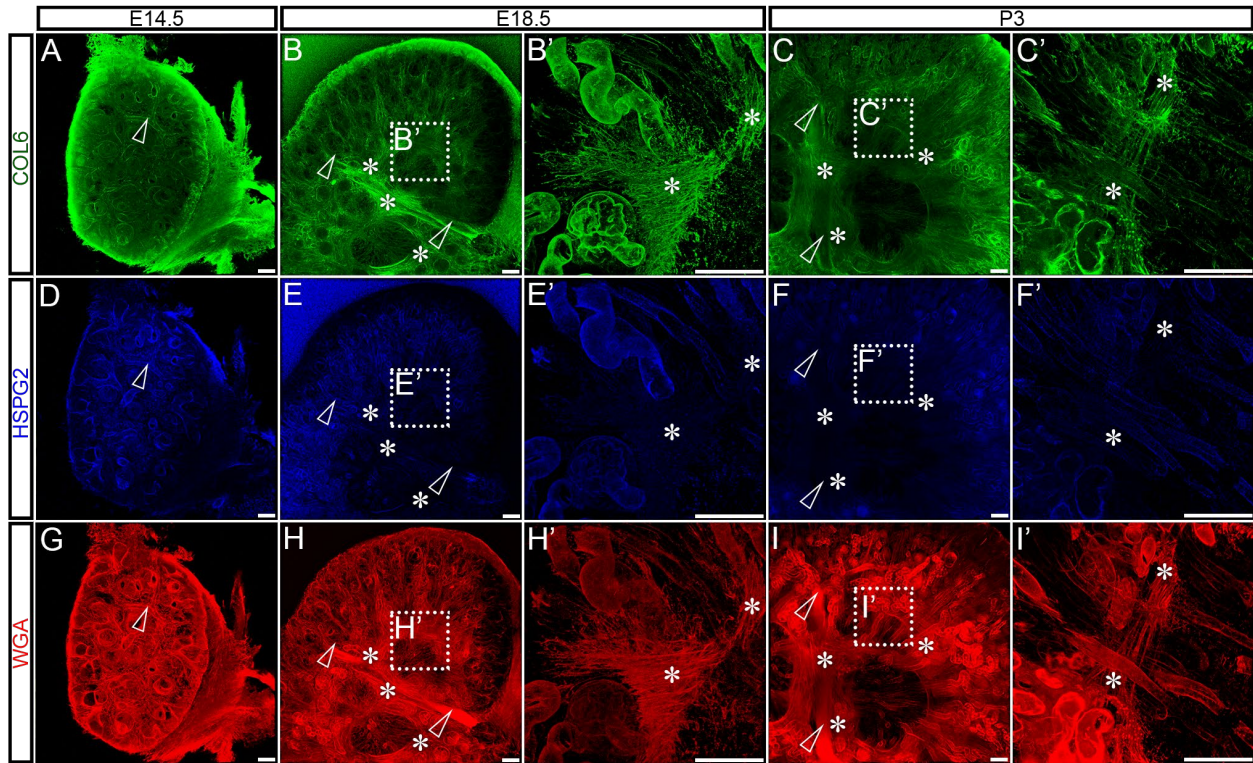


Figure S11: Medullary ray sheath fibers were only found at E18.5 and P3 and contained COL6. (A, D, G) At E14.5, a fibrous ECM (green = COL6) ran parallel to developing blood vessels (open arrowheads) and surrounded tubules (blue = HSPG2; red = WGA). **(B, B', C, C', E, E', F, F', H, H', I, I')** Medullary ray sheath fibers (*) surrounded the developing nephron (*CD* = collecting duct, *LOH* = loop of Henle) at E18.5 – P3. Boxes indicate where representative inset at a higher magnification was obtained. Scale bars = 100 μ m. Dimensions confocal z-stacks in A-I (10 \times): 1.42 mm \times 1.42 mm \times 100 μ m ($x \times y \times z$); B', C', E', F', H', I' (40 \times): 354 \times 354 \times 36 μ m. Representative images from $n = 3$ biological replicates.

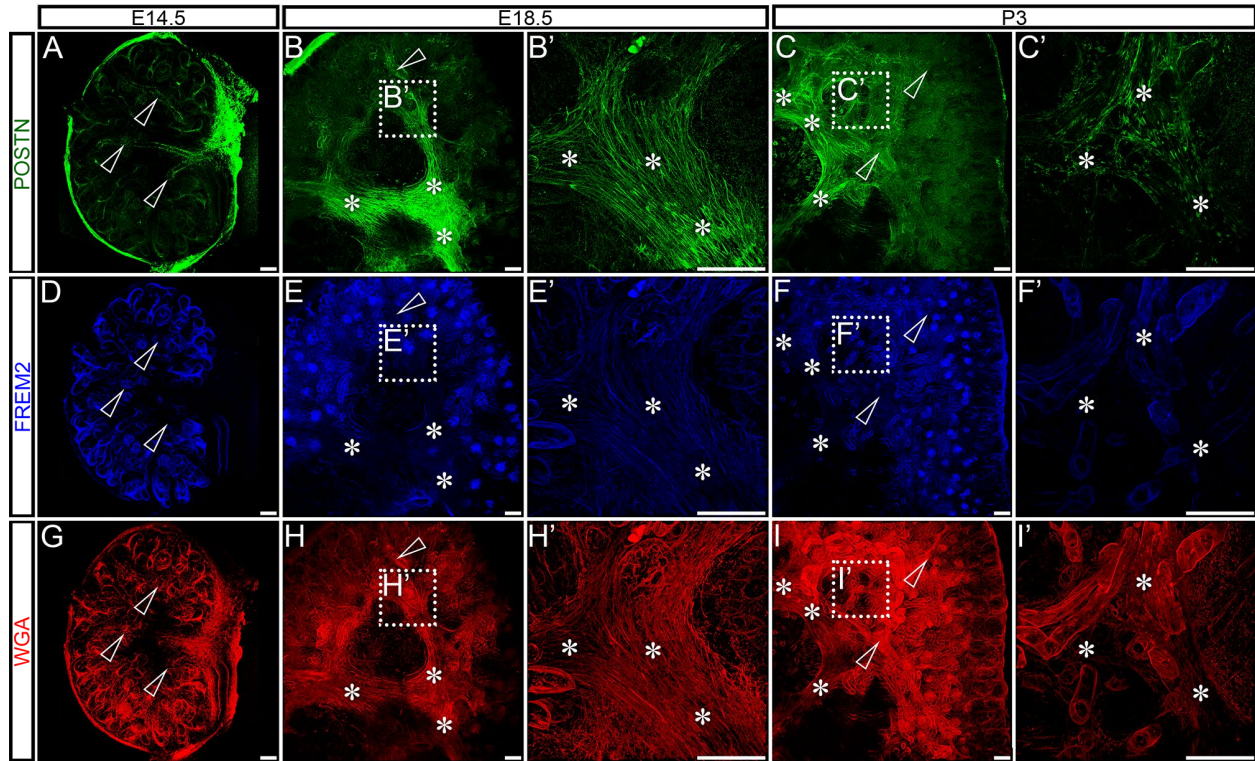


Figure S12: Medullary ray sheath fibers were only found at E18.5 and P3 and contained POSTN. (A, D, G) At E14.5, a fibrous ECM (green = POSTN) ran parallel to developing blood vessels (open arrowheads) and surrounded tubules (blue = FREM2; red = WGA). **(B, B', C, C', E, E', F, F', H, H', I, I')** Medullary ray sheath fibers (*) surrounded the developing nephron (*CD* = collecting duct, *LOH* = loop of Henle) at E18.5 – P3. Boxes indicate where representative inset at a higher magnification was obtained. Scale bars = 100 μm . Dimensions confocal z-stacks in A-I (10 \times): 1.48 mm \times 1.48 mm \times 148 μm ($x \times y \times z$); B', C', E', F', H', I' (40 \times): 345 \times 345 \times 57 μm . Representative images from $n = 3$ biological replicates.

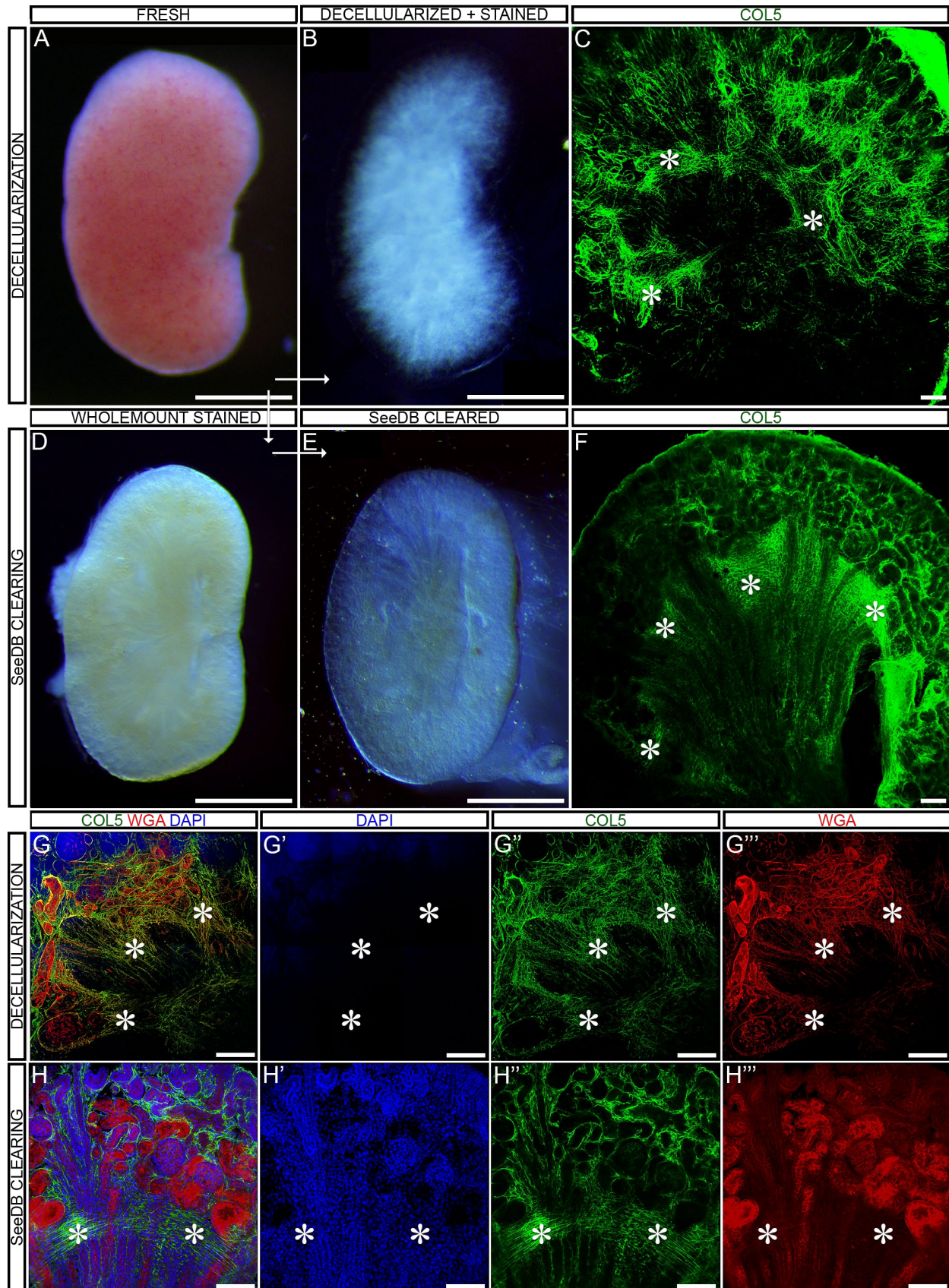


Figure S13: COL5⁺ medullary ray sheath fibers were observed in decellularized and SeeDB-cleared kidneys. (A, B, D, E) Fresh kidneys (A) were decellularized (B) then fixed and stained or fixed and stained (D) and cleared using SeeDB (E). (C, F) In both the decellularized (C) and SeeDB cleared kidneys (F) medullary ray sheath fibers were observed (*). (G - G''') In decellularized kidneys, cells do not remain intact as indicated by the loss of nuclear staining (DAPI = Blue), and WGA (red) co-localized with the interstitial matrix stain of COL5 of the medullary ray sheath fibers. (H - H''') In SeeDB cleared kidneys, the nuclei (DAPI) and tubular structures (WGA) remain intact and are surrounded by the medullary ray sheath fibers (COL5). Scale bar = 1 mm (A, B, D, F) Scale bar = 100 μm (C, F, G - G''', H - H'''), Dimensions of confocal z-stacks in C, F (10 \times): $1480 \times 1480 \times 148 \mu\text{m}$ ($x \times y \times z$); Dimensions of confocal z-stacks in G - G''', H - H''' (25 \times): $590 \times 590 \times 57 \mu\text{m}$. Representative image from $n = 3$ biological replicates.

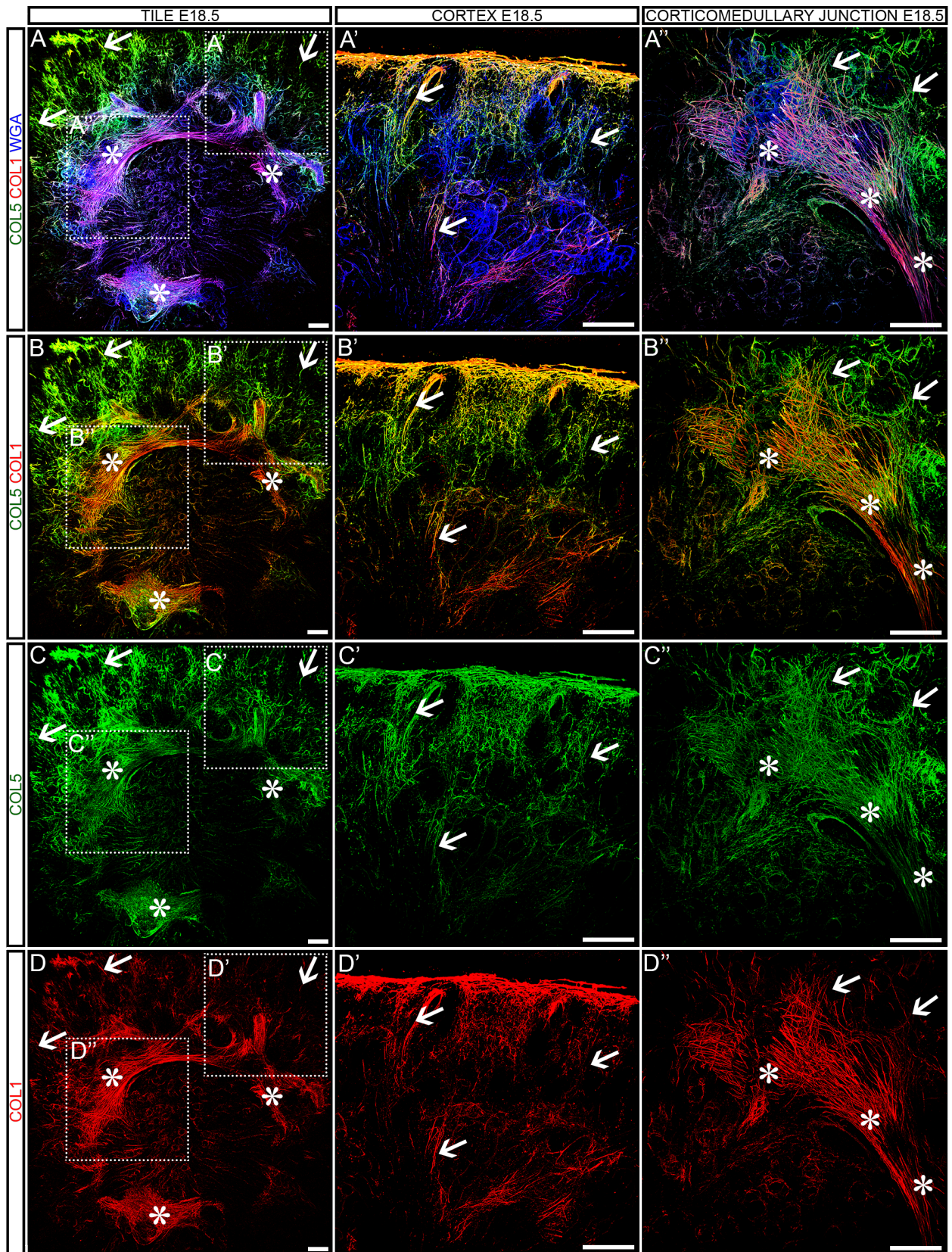


Figure S14: Colocalization of COL1 and COL5 in the E18.5 kidney cortex and corticomedullary junction. (A-D) COL1 and COL5 co-localized. COL1 and COL5 are enriched in the vertical fibers (A' - D') and medullary ray sheath fibers (A'' - D''). Boxes indicate where representative inset at a higher magnification was obtained. Scale bars =100 μm . Dimensions of confocal z-stacks in A-D (10 \times): 1.48 mm \times 1.48 mm \times 148 μm ($x \times y \times z$); A'- D' and A''- D'' (25 \times): 590 \times 590 \times 57 μm . Representative images from $n = 3$ biological replicates.

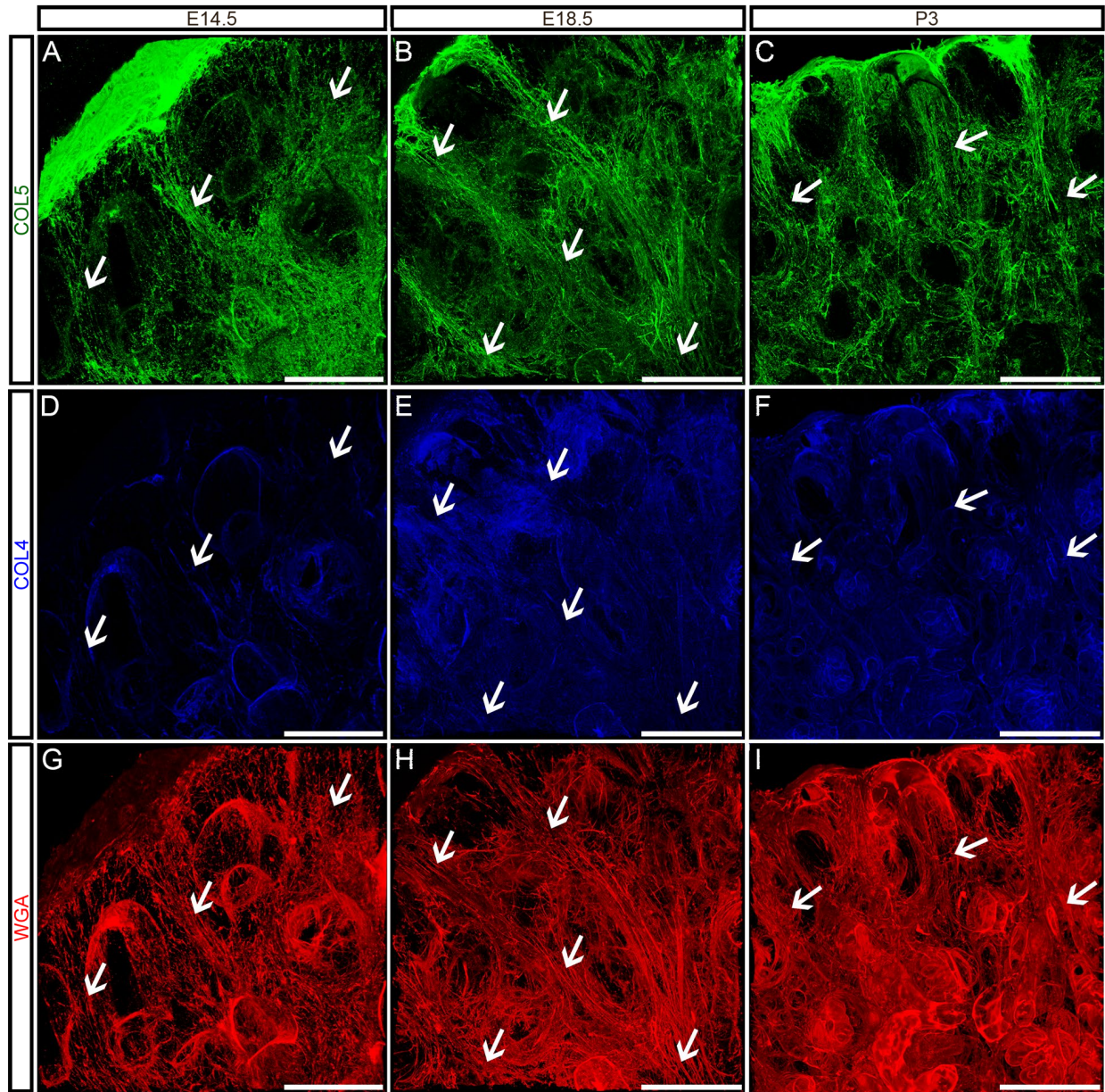


Figure S15: COL5+ vertical fibers were observed in the cortex. E14.5, E18.5, and P3 vertical fibers (arrows) ran parallel to, and emanated from, the tubules to the capsule in vertical fibers (green = COL5; blue = COL4; red = WGA). Dimensions of 40× confocal z-stacks $354 \times 354 \times 45 \mu\text{m}$ ($x \times y \times z$). Representative image from $n = 3$ biological replicates.

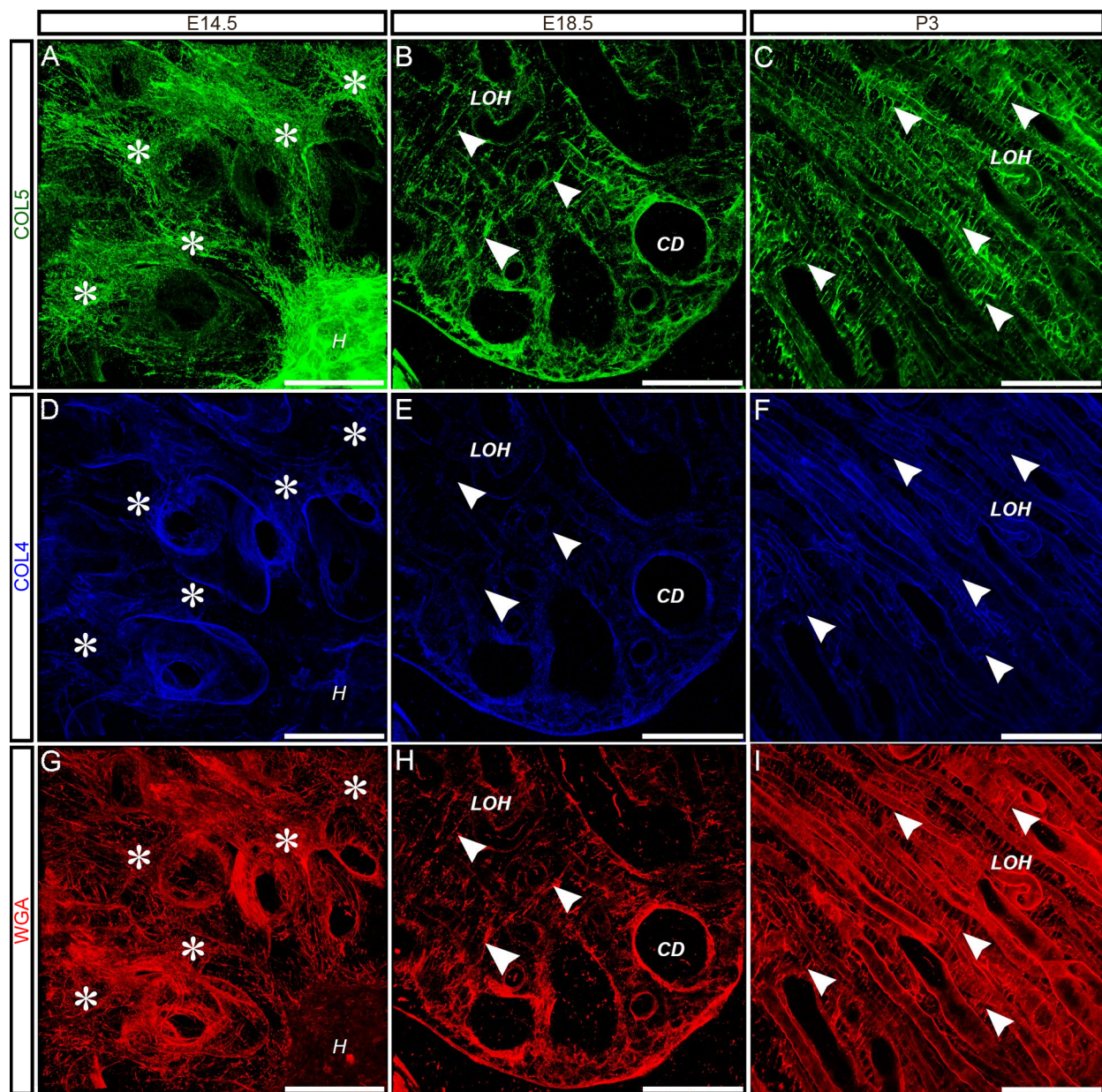


Figure S16: COL5+ “rungs of a ladder” fibers were observed in the medulla. (A, B, G) Some fibers (arrows) extended from the developing kidney hilum (*H*) at E14.5. **(B, C, E, F, H, I)** “Rungs of a ladder” appearance of the interstitial matrix (arrowheads) at E18.5 and P3 between loop of Henle (*LOH*) and collecting duct (*CD*) tubules. Scale bars = 100 μm . Dimensions of 40 \times confocal z-stacks in A, D, G: 354 \times 354 \times 45 μm ($x \times y \times z$); B, C, E, F, H, I: 354 \times 354 \times 11 μm . Representative image from $n = 3$ biological replicates.

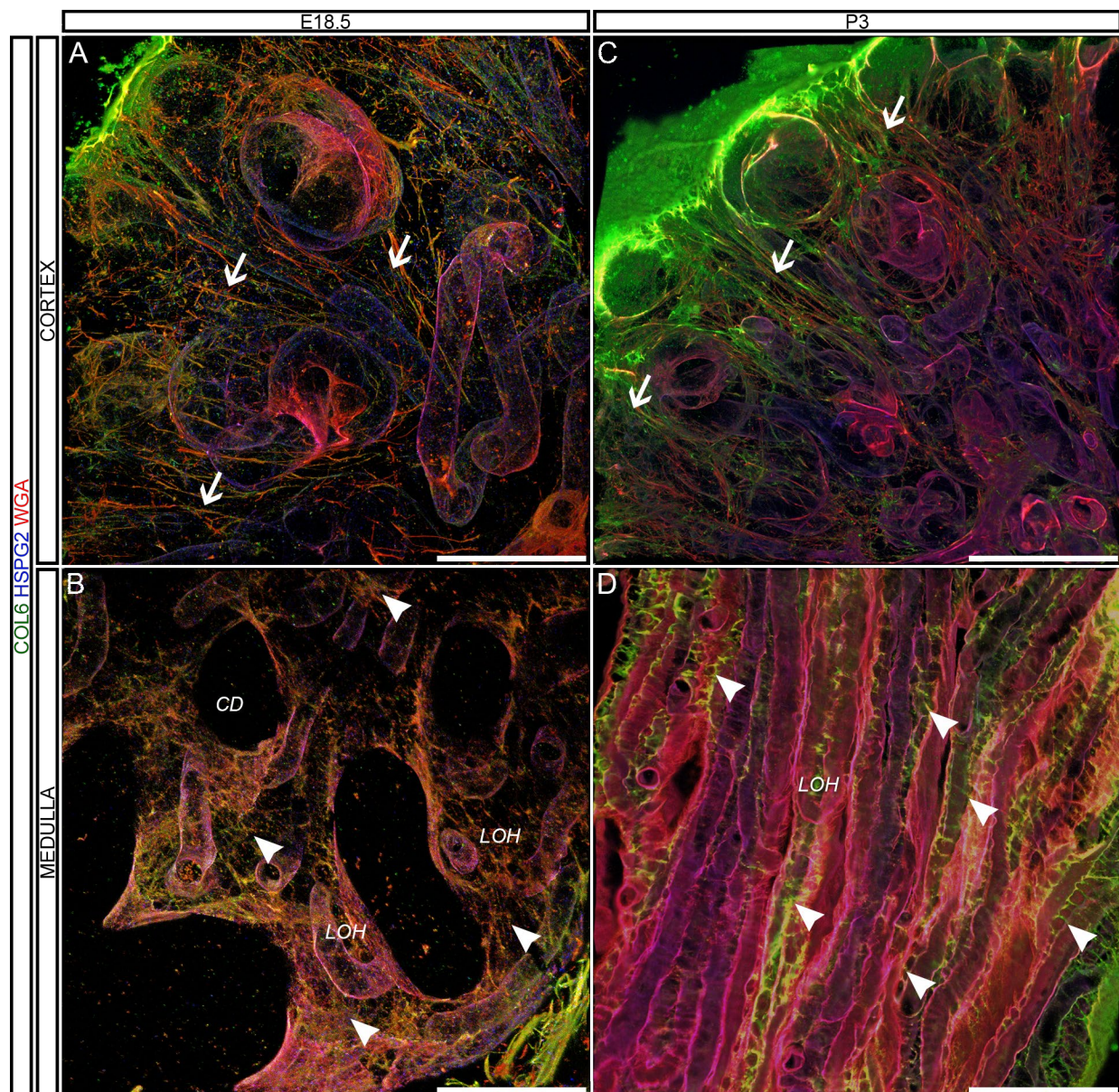


Figure S17: The morphology of interstitial fibers was distinct between cortex and medulla for COL6. (A, C) E18.5, and P3 vertical fibers (arrows) ran parallel to, and emanated from, the tubules to the capsule in vertical fibers (green = COL6; blue = HSPG2; red = WGA). (B-D) “Rungs of a ladder” appearance of the interstitial matrix (arrowheads) at E18.5 and P3 between loop of Henle (*LOH*) and collecting duct (*CD*) tubules. Scale bars = 100 μm. Dimensions of 40× confocal

z-stacks in A, C: $354 \times 354 \times 45 \text{ }\mu\text{m}$ ($x \times y \times z$); B, D: $354 \times 354 \times 11 \text{ }\mu\text{m}$. Representative image from $n = 3$ biological replicates.

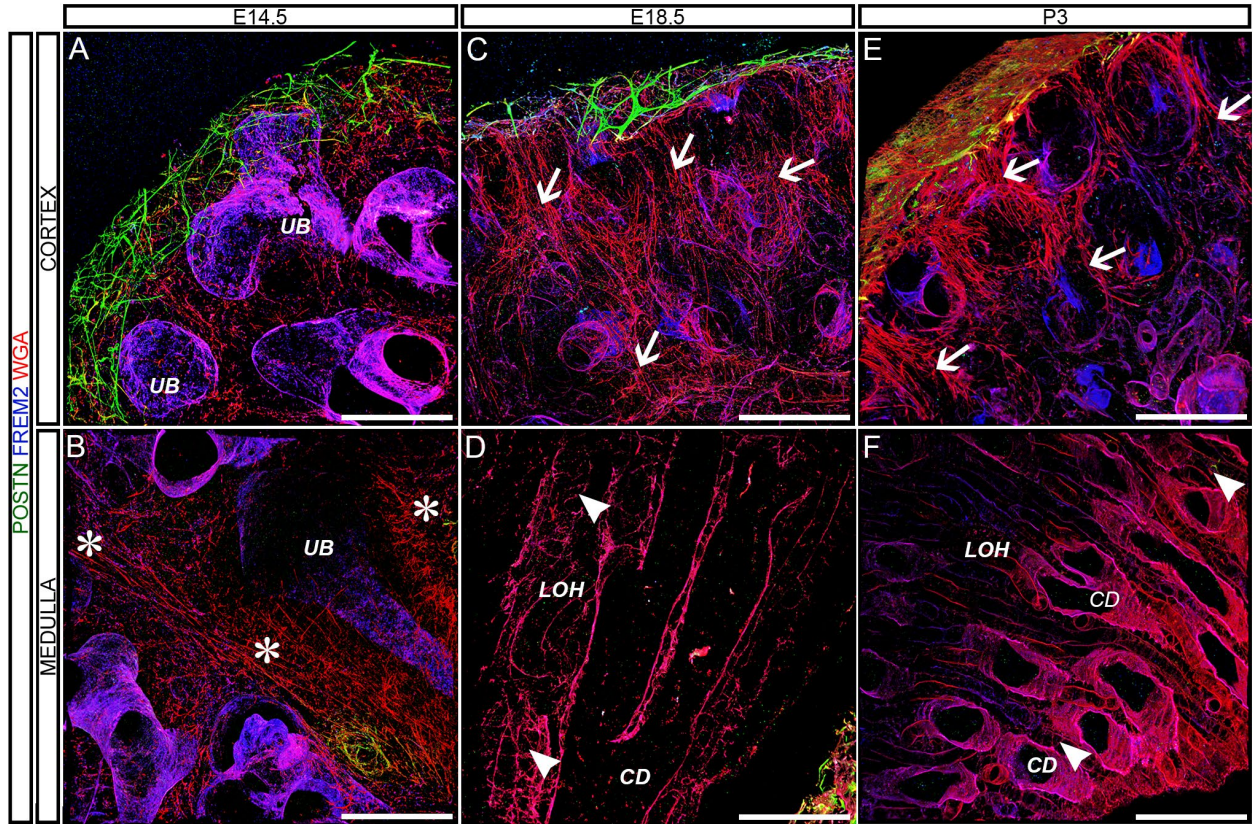


Figure S18: The morphology of interstitial fibers was distinct between the cortex and medulla. (A, C, E) E14.5, E18.5, and P3 POSTN+ fibers (green) were observed in the capsule but not in the vertical fibers (arrows) around the developing ureteric bud (UB) and nephrogenic zone (blue = FREM2; red = WGA). (B) Some E14.5 fibers (*) ran circumferentially and in parallel to the ureteric bud (UB). (D, F) “Rungs of a ladder” appearance of the interstitial matrix (closed arrowheads) at E18.5 and P3 between loop of Henle (LOH) and collecting duct (CD) tubules. Scale bars = 100 μm . Dimensions of 25 \times confocal z-stacks in A, B, C, E: $345 \times 345 \times 57 \mu\text{m}$ ($x \times y \times z$) and D and F: $345 \times 345 \times 14 \mu\text{m}$. Representative image from $n = 3$ biological replicates.

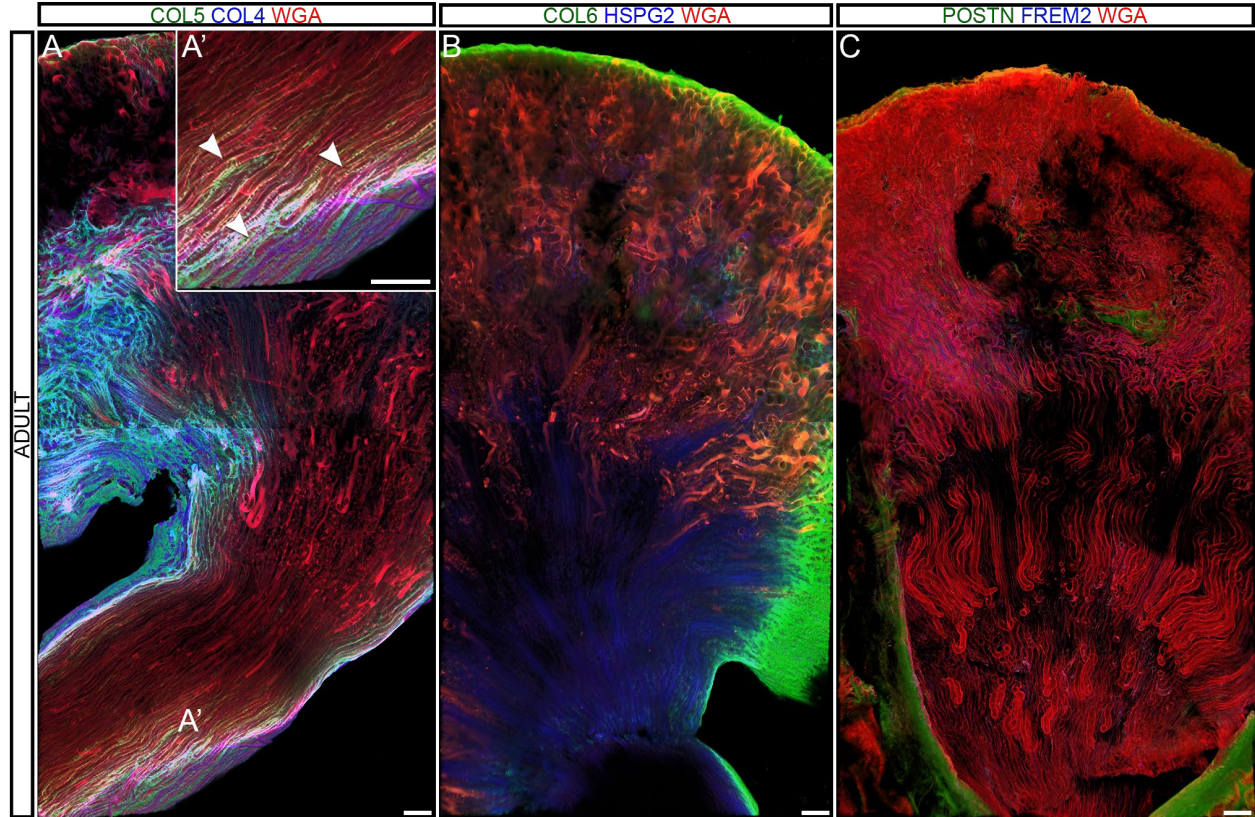


Figure S19: Interstitial accumulations were not observed in the adult mouse kidney. (A, B) Adult kidneys stained for COL5, COL4, and WGA (A), COL6, HSPG2, and WGA (B), POSTN, FREM2, and WGA (C) do not show accumulations of interstitial matrix as observed at developmental timepoints. POSTN+ interstitial matrix corresponding to the perivascular fibers (open arrow) were observed. (A') "Rungs of a ladder" fibers (arrowhead) in the papilla. Scale bars = 100 μm . 10 \times confocal z-stacks in A, B: 2.8 mm \times 1.4 mm \times 100 μm ($x \times y \times z$) and (C): 10 \times confocal z-stacks 1.48 mm \times 2.80 mm \times 148 μm ($x \times y \times z$). Representative image from $n = 3$ biological replicates.

References:

1. Saleh, AM, Jacobson, KR, Kinzer-Ursem, TL, Calve, S: Dynamics of non-canonical amino acid-labeled intra- and extracellular proteins in the developing mouse. *Cel Mol Bioeng*, 12, 2019.
2. Naba, A, Clauser, KR, Hynes, RO: Enrichment of extracellular matrix proteins from tissues and digestion into peptides for mass spectrometry analysis. *J Vis Exp*, 2015.
3. Cox, J, Mann, M: MaxQuant enables high peptide identification rates, individualized p.p.b.-range mass accuracies and proteome-wide protein quantification. *Nat Biotechnol*, 26: 1367-1372, 2008.
4. Cox, J, Hein, MY, Lubner, CA, Paron, I, Nagaraj, N, Mann, M: Accurate proteome-wide label-free quantification by delayed normalization and maximal peptide ratio extraction, termed MaxLFQ. *Mol Cell Proteomics*, 13: 2513-2526, 2014.
5. Acuna, A, Drakopoulos, MA, Leng, Y, Goergen, CJ, Calve, S: Three-dimensional visualization of extracellular matrix networks during murine development. *Dev Biol*, 435: 122-129, 2018.
6. Speller, AM, Moffat, DB: Tubulo-vascular relationships in the developing kidney. *J Anat*, 123: 487-500, 1977.
7. Schindelin, J, Arganda-Carreras, I, Frise, E, Kaynig, V, Longair, M, Pietzsch, T, Preibisch, S, Rueden, C, Saalfeld, S, Schmid, B, Tinevez, JY, White, DJ, Hartenstein, V, Eliceiri, K, Tomancak, P, Cardona, A: Fiji: an open-source platform for biological-image analysis. *Nat Methods*, 9: 676-682, 2012.
8. Miura, K, Rueden, C, Hiner, M, Schindelin, J, Rietdorf, J: ImageJ plugin CorrectBleach V2.0.2. Zenodo. 10.5281/zenodo.30769, 2014.
9. Schmid, B, Schindelin, J, Cardona, A, Longair, M, Heisenberg, M: A high-level 3D visualization API for Java and ImageJ. *BMC Bioinformatics*, 11: 274, 2010.
10. Ocken, AR, Ku, MM, Kinzer-Ursem, TL, Calve, S: Perlecan knockdown significantly alters extracellular matrix composition and organization during cartilage development. *Mol Cell Proteomics*, 2020.
11. Goeminne, LJE, Argentini, A, Martens, L, Clement, L: Summarization vs peptide-based models in label-free quantitative proteomics: Performance, pitfalls, and data analysis guidelines. *J Proteome Res*, 14: 2457-2465, 2015.
12. England, AR, Chaney, CP, Das, A, Patel, M, Malewska, A, Armendariz, D, Hon, GC, Strand, DW, Drake, KA, Carroll, TJ: Identification and characterization of cellular heterogeneity within the developing renal interstitium. *Development*, 147: dev190108, 2020.
13. Hum, S, Rymer, C, Schaefer, C, Bushnell, D, Sims-Lucas, S: Ablation of the renal stroma defines its critical role in nephron progenitor and vasculature patterning. *PLoS One*, 9: e88400, 2014.
14. Schumacher, K, Strehl, R, De Vries, U, Groene, HJ, Minuth, WW: SBA-positive fibers between the CD ampulla, mesenchyme, and renal capsule. *J Am Soc Nephrol*, 13: 2446-2453, 2002.
15. Marxer-Meier, A, Hegyi, I, Loffing, J, Kaissling, B: Postnatal maturation of renal cortical peritubular fibroblasts in the rat. *Anat Embryol*, 197: 143-153, 1998.
16. Maric, C, Ryan, GB, Alcorn, D: Embryonic and postnatal development of the rat renal interstitium. *Anat Embryol (Berl)*, 195: 503-514, 1997.
17. Cullen-McEwen, LA, Caruana, G, Bertram, JF: The where, what and why of the developing renal stroma. *Nephron Exp Nephrol*, 99: e1-8, 2005.

18. Byron, A, Humphries, JD, Humphries, MJ: Defining the extracellular matrix using proteomics. *Int J Exp Pathol*, 94: 75-92, 2013.
19. Lennon, R, Byron, A, Humphries, JD, Randles, MJ, Carisey, A, Murphy, S, Knight, D, Brenchley, PE, Zent, R, Humphries, MJ: Global analysis reveals the complexity of the human glomerular extracellular matrix. *J Am Soc Nephrol*, 25: 939-951, 2014.
20. Tsutsui, K, Machida, H, Morita, R, Nakagawa, A, Sekiguchi, K, Miner, JH, Fujiwara, H: Mapping the molecular and structural specialization of the skin basement membrane for inter-tissue interactions. *bioRxiv*: 2020.2004.2027.061952, 2020.
21. Votteler, M, Berrio, DAC, Horke, A, Sabatier, L, Reinhardt, DP, Nsair, A, Aikawa, E, Schenke-Layland, K: Elastogenesis at the onset of human cardiac valve development. *Development* 140: 2345-2353, 2013.
22. Sterzel, RB, Hartner, A, Schlotzer-Schrehardt, U, Voit, S, Hausknecht, B, Doliana, R, Colombatti, A, Gibson, MA, Braghetta, P, Bressan, GM: Elastic fiber proteins in the glomerular mesangium in vivo and in cell culture. *Kidney Int*, 58: 1588-1602, 2000.
23. Leimeister, C, Steidl, C, Schumacher, N, Erhard, S, Gessler, M: Developmental expression and biochemical characterization of Emu family members. *Dev Biol*, 249: 204-218, 2002.
24. McLaughlin, PJ, Chen, Q, Horiguchi, M, Starcher, BC, Stanton, JB, Broekelmann, TJ, Marmorstein, AD, McKay, B, Mecham, R, Nakamura, T, Marmorstein, LY: Targeted disruption of fibulin-4 abolishes elastogenesis and causes perinatal lethality in mice. *Mol Cell Biol*, 26: 1700-1709, 2006.
25. Halabi, CM, Broekelmann, TJ, Lin, M, Lee, VS, Chu, ML, Mecham, RP: Fibulin-4 is essential for maintaining arterial wall integrity in conduit but not muscular arteries. *Sci Adv*, 3: e1602532, 2017.
26. Schiavinato, A, Keene, DR, Imhof, T, Doliana, R, Sasaki, T, Sengle, G: Fibulin-4 deposition requires EMILIN-1 in the extracellular matrix of osteoblasts. *Sci Rep*, 7: 5526, 2017.
27. Kostka, G, Giltay, R, Bloch, W, Addicks, K, Timpl, R, Fassler, R, Chu, ML: Perinatal lethality and endothelial cell abnormalities in several vessel compartments of fibulin-1-deficient mice. *Mol Cell Biol*, 21: 7025-7034, 2001.
28. Hirani, R, Hanssen, E, Gibson, MA: LTBP-2 specifically interacts with the amino-terminal region of fibrillin-1 and competes with LTBP-1 for binding to this microfibrillar protein. *Matrix Biol*, 26: 213-223, 2007.
29. Isogai, Z, Ono, RN, Ushiro, S, Keene, DR, Chen, Y, Mazzieri, R, Charbonneau, NL, Reinhardt, DP, Rifkin, DB, Sakai, LY: Latent transforming growth factor beta-binding protein 1 interacts with fibrillin and is a microfibril-associated protein. *J Biol Chem*, 278: 2750-2757, 2003.
30. Noda, K, Dabovic, B, Takagi, K, Inoue, T, Horiguchi, M, Hirai, M, Fujikawa, Y, Akama, TO, Kusumoto, K, Zilberberg, L, Sakai, LY, Koli, K, Naitoh, M, von Melchner, H, Suzuki, S, Rifkin, DB, Nakamura, T: Latent TGF- β binding protein 4 promotes elastic fiber assembly by interacting with fibulin-5. *Proc Natl Acad Sci USA*, 110: 2852-2857, 2013.
31. Tsutsui, K, Manabe, R, Yamada, T, Nakano, I, Oguri, Y, Keene, DR, Sengle, G, Sakai, LY, Sekiguchi, K: ADAMTSL-6 is a novel extracellular matrix protein that binds to fibrillin-1 and promotes fibrillin-1 fibril formation. *J Biol Chem*, 285: 4870-4882, 2010.
32. Saito, M, Kurokawa, M, Oda, M, Oshima, M, Tsutsui, K, Kosaka, K, Nakao, K, Ogawa, M, Manabe, R, Suda, N, Ganjargal, G, Hada, Y, Noguchi, T, Teranaka, T, Sekiguchi, K, Yoneda, T, Tsuji, T: ADAMTSL6 β protein rescues fibrillin-1 microfibril disorder in a

- Marfan syndrome mouse model through the promotion of fibrillin-1 assembly. *J Biol Chem*, 286: 38602-38613, 2011.
33. Gordon, MK, Hahn, RA: Collagens. *Cell Tissue Res*, 339: 247-257, 2010.

Table S2: Classifications of proteins based on interstitial matrix, basement membrane, and other based on ¹⁻³ with additional re-annotations based on the literature (also see Figure S1).

PROTEIN NAME	Simple classifications	classifications based on ¹⁻³ with additional reannotation based on citations
AMELY	basement membrane	homology with AMELX
BGLAP	interstitial matrix	
ELSPBP1	interstitial matrix	
EYS	interstitial matrix	
FBN3	interstitial matrix	
KAL1	basement membrane	
LAMB4	basement membrane	
MFAP1	interstitial matrix	
MXRA5	interstitial matrix	
POMZP3	interstitial matrix	
PXDNL	interstitial matrix	by homology with PXDN
ZP4	basement membrane	
COL21A1	interstitial matrix	
5430419D17Rik	interstitial matrix	
ABI3BP	interstitial matrix	
ADIPOQ	interstitial matrix	
AEBP1	interstitial matrix	
AGRN	basement membrane	basement membrane ⁴
AMBN	interstitial matrix	
AMELX	basement membrane	
AW551984	interstitial matrix	
BGLAP2	interstitial matrix	
BGLAP3	interstitial matrix	
BMPER	interstitial matrix	
BSPH1	interstitial matrix	
BSPH2	interstitial matrix	
CDCP2	interstitial matrix	
CILP	interstitial matrix	
CILP2	interstitial matrix	
COCH	interstitial matrix	
COLQ	basement membrane	
COMP	interstitial matrix	interstitial matrix ⁵
CRELD1	interstitial matrix	
CRELD2	interstitial matrix	
CRIM1	interstitial matrix	
CRISPLD1	interstitial matrix	
CRISPLD2	interstitial matrix	
CTGF	interstitial matrix	
CTHRC1	interstitial matrix	
CYR61	interstitial matrix	
DDX26B	interstitial matrix	
DMBT1	interstitial matrix	
DMP1	interstitial matrix	
DPT	interstitial matrix	interstitial matrix ⁶

DSPP	interstitial matrix	
ECM1	basement membrane	basement membrane ⁷
ECM2	interstitial matrix	
EDIL3	interstitial matrix	
EFEMP1	<i>elastin-microfibril axis</i> ; interstitial matrix	<i>elastin-microfibril axis</i> ^{8,9} ; interstitial matrix ^{9,10}
EFEMP2	<i>elastin-microfibril axis</i> ; interstitial matrix	<i>elastin-microfibril axis</i> ^{9,11,12} ; interstitial matrix ^{9,11,12}
EGFEM1	interstitial matrix	
EGFLAM	basement membrane	
ELN	<i>elastin-microfibril axis</i> ; interstitial matrix	<i>elastin-microfibril axis</i> ; interstitial matrix ^{11,12} ;
EMID1	<i>elastin-microfibril axis</i> ; interstitial matrix	<i>elastin-microfibril axis</i> ¹³ ; interstitial matrix (COL26A1 homology) ¹³ .
EMILIN1	<i>elastin-microfibril axis</i> ; interstitial matrix	<i>elastin-microfibril axis</i> ^{9,14} interstitial matrix ^{14,15}
EMILIN2	<i>elastin-microfibril axis</i> ; interstitial matrix	<i>elastin-microfibril axis</i> ^{9,14,16} interstitial matrix ¹⁶
EMILIN3	<i>elastin-microfibril axis</i> ; interstitial matrix	<i>elastin-microfibril axis</i> ^{9,14,16} interstitial matrix ¹⁶
FBLN1	<i>elastin-microfibril axis</i> ; interstitial matrix	<i>elastin-microfibril axis</i> ¹⁷ ; interstitial matrix ¹⁸ basement membrane ¹⁹
FBLN2	<i>elastin-microfibril axis</i> ; interstitial matrix	<i>elastin-microfibril axis</i> ^{20,21} ; interstitial matrix ²¹
FBLN5	<i>elastin-microfibril axis</i> ; interstitial matrix	<i>elastin-microfibril axis</i> ; interstitial matrix ²²
FBLN7	<i>elastin-microfibril axis</i> ; interstitial matrix	by homology
FBN1	<i>elastin-microfibril axis</i> ; interstitial matrix	<i>elastin-microfibril axis</i> ; interstitial matrix ^{23,24}
FBN2	<i>elastin-microfibril axis</i> ; interstitial matrix	<i>elastin-microfibril axis</i> ; interstitial matrix ^{23,25}
FGA	other	
FGB	other	
FGG	other	
FGL1	interstitial matrix	
FGL2	interstitial matrix	
FN1	interstitial matrix	interstitial matrix ^{14,19}
FNDC1	interstitial matrix	
FNDC7	interstitial matrix	
FNDC8	interstitial matrix	
FRAS1	basement membrane	basement membrane ^{26,27}
GAS6	interstitial matrix	
GLDN	interstitial matrix	
HMCN1	basement membrane	
HMCN2	basement membrane	
IBSP	interstitial matrix	
IGFALS	interstitial matrix	
IGFBP1	other	
IGFBP2	other	
IGFBP3	other	
IGFBP4	other	
IGFBP5	other	
IGFBP6	other	
IGFBP7	other	other ^{18,28}
IGFBPL1	other	
IGSF10	other	

KCP	other	other ²⁹
LAMA1	basement membrane	basement membrane ³⁰
LAMA2	basement membrane	basement membrane ^{31,32}
LAMA3	basement membrane	basement membrane ³³
LAMA4	basement membrane	basement membrane ³⁴
LAMA5	basement membrane	basement membrane ³⁵
LAMB1	basement membrane	basement membrane ^{36,37}
LAMB2	basement membrane	basement membrane ³⁸
LAMB3	basement membrane	basement membrane ³⁹
LAMC1	basement membrane	basement membrane ⁴⁰
LAMC2	basement membrane	
LAMC3	basement membrane	
LGI1	interstitial matrix	
LGI2	interstitial matrix	
LGI3	interstitial matrix	
LGI4	interstitial matrix	
LRG1	interstitial matrix	
LTBP1	<i>elastin-microfibril axis</i> ; interstitial matrix	<i>elastin-microfibril axis</i> ⁴¹ ; interstitial matrix ⁴¹
LTBP2	<i>elastin-microfibril axis</i> ; interstitial matrix	<i>elastin-microfibril axis</i> ⁴² ; interstitial matrix ⁴²
LTBP3	<i>elastin-microfibril axis</i> ; interstitial matrix	<i>elastin-microfibril axis</i> ⁴³ ; interstitial matrix
LTBP4	<i>elastin-microfibril axis</i> ; interstitial matrix	<i>elastin-microfibril axis</i> ⁴⁴ ; interstitial matrix ⁴⁴
MATN1	interstitial matrix	interstitial matrix ⁴⁵
MATN2	interstitial matrix	interstitial matrix ⁴⁶
MATN3	interstitial matrix	interstitial matrix ⁴⁷
MATN4	interstitial matrix	interstitial matrix; by homology
MEPE	interstitial matrix	
MFAP1A	<i>elastin-microfibril axis</i> ; interstitial matrix	<i>elastin-microfibril axis</i> ; interstitial matrix (by homology)
MFAP1B	<i>elastin-microfibril axis</i> ; interstitial matrix	<i>elastin-microfibril axis</i> ; interstitial matrix (by homology)
MFAP2	<i>elastin-microfibril axis</i> ; interstitial matrix	<i>elastin-microfibril axis</i> ; interstitial matrix ⁴⁸
MFAP3	<i>elastin-microfibril axis</i> ; interstitial matrix	<i>elastin-microfibril axis</i> ; interstitial matrix (by homology)
MFAP4	<i>elastin-microfibril axis</i> ; interstitial matrix	<i>elastin-microfibril axis</i> ; interstitial matrix (by homology)
MFAP5	<i>elastin-microfibril axis</i> ; interstitial matrix	<i>elastin-microfibril axis</i> ⁴⁹ ; interstitial matrix (by homology)
MFGE8	interstitial matrix	
MGP	interstitial matrix	
MMRN1	<i>elastin-microfibril axis</i> ; interstitial matrix	<i>elastin-microfibril axis</i> ; interstitial matrix ⁵⁰
MMRN2	<i>elastin-microfibril axis</i> ; interstitial matrix	<i>elastin-microfibril axis</i> ; interstitial matrix ⁵⁰
NDNF	interstitial matrix	
NELL1	interstitial matrix	
NELL2	interstitial matrix	
NID1	basement membrane	basement membrane ⁵¹
NID2	basement membrane	basement membrane ⁵¹
NOV	interstitial matrix	
NPNT	basement membrane	basement membrane ^{52,53}

NTN1	basement membrane	
NTN3	basement membrane	
NTN4	basement membrane	
NTN5	basement membrane	
NTNG1	interstitial matrix	
NTNG2	interstitial matrix	
OIT3	interstitial matrix	
OTOG	interstitial matrix	
OTOGL	interstitial matrix	
OTOL1	interstitial matrix	
PAPLN	basement membrane	basement membrane ⁵⁴
PCOLCE	interstitial matrix	
PCOLCE2	interstitial matrix	
POSTN	interstitial matrix	interstitial matrix ^{22,55,56} basement membrane ¹⁹
PXDN	interstitial matrix	interstitial matrix ^{57,58} ; some basement membrane staining ⁵⁹
RELN	interstitial matrix	
RSPO1	interstitial matrix	
RSPO2	interstitial matrix	
RSPO3	interstitial matrix	
RSPO4	interstitial matrix	
SBSPON	interstitial matrix	
SLAMF6	interstitial matrix	
SLIT1	interstitial matrix	
SLIT2	interstitial matrix	
SLIT3	interstitial matrix	
SMOC1	basement membrane	basement membrane ⁵⁴
SMOC2	basement membrane	basement membrane ⁵⁴
SNED1	interstitial matrix	
SPARC	basement membrane	basement membrane ^{60 61}
SPARCL1	interstitial matrix	
SPON1	interstitial matrix	
SPON2	interstitial matrix	
SPP1	interstitial matrix	
SRPX	interstitial matrix	
SRPX2	interstitial matrix	
SSPO	interstitial matrix	
SVEP1	interstitial matrix	
TECTA	interstitial matrix	
TECTB	interstitial matrix	
TGFBI	interstitial matrix	interstitial matrix ²²
THBS1	interstitial matrix	interstitial matrix ⁶²
THBS2	interstitial matrix	
THBS3	interstitial matrix	
THBS4	interstitial matrix	
THSD4	<i>elastin-microfibril axis</i> ; interstitial matrix	<i>elastin-microfibril axis</i> ^{63,64} ; interstitial matrix ^{63,64}

TINAG	basement membrane	basement membrane ^{2,65,66}
TINAGL1	basement membrane	basement membrane ^{67 68}
TNC	interstitial matrix	interstitial matrix ⁶⁹
TNFAIP6	interstitial matrix	
TNN	interstitial matrix	
TNR	interstitial matrix	
TNXB	interstitial matrix	interstitial matrix ⁷⁰²³⁴
TSKU	interstitial matrix	
TSPEAR	basement membrane	
VIT	interstitial matrix	
VTN	interstitial matrix	interstitial matrix ^{19,71}
VWA1	basement membrane	basement membrane ⁷²
VWA2	basement membrane	basement membrane ⁷³
VWA3A	interstitial matrix	
VWA3B	interstitial matrix	
VWA5A	interstitial matrix	
VWA5B1	interstitial matrix	
VWA5B2	interstitial matrix	
VWA7	interstitial matrix	
VWA9	interstitial matrix	
VWCE	interstitial matrix	
VWDE	interstitial matrix	
VWF	interstitial matrix	
WISP1	interstitial matrix	
WISP2	interstitial matrix	
WISP3	interstitial matrix	
ZP1	interstitial matrix	
ZP2	interstitial matrix	
ZP3	interstitial matrix	
ZP3R	interstitial matrix	
ZPLD1	interstitial matrix	
COL10A1	interstitial matrix	interstitial matrix ⁷⁴
COL11A1	interstitial matrix	interstitial matrix ⁷⁴
COL11A2	interstitial matrix	interstitial matrix ⁷⁴
COL12A1	interstitial matrix	interstitial matrix ⁷⁵⁻⁷⁷ ; some basement membrane staining ^{76,78}
COL13A1	interstitial matrix	
COL14A1	interstitial matrix	interstitial matrix ^{79,80}
COL15A1	basement membrane	basement membrane ⁸¹
COL16A1	interstitial matrix	
COL17A1	basement membrane	
COL18A1	basement membrane	basement membrane ⁸²
COL19A1	interstitial matrix	
COL1A1	interstitial matrix	interstitial matrix ^{83 84}
COL1A2	interstitial matrix	interstitial matrix ^{83,84}
COL20A1	interstitial matrix	

COL22A1	interstitial matrix	
COL23A1	interstitial matrix	
COL24A1	interstitial matrix	
COL25A1	interstitial matrix	
COL26A1	<i>elastin-microfibril axis</i> ; interstitial matrix	<i>elastin-microfibril axis</i> ¹³ ; interstitial matrix ⁸⁵
COL27A1	interstitial matrix	
COL28A1	interstitial matrix	
COL2A1	interstitial matrix	interstitial matrix; with basement membrane components glomeruli ⁸⁶ , base of renal epithelial cells ⁸⁷ epithelium ^{74,88}
COL3A1	interstitial matrix	
COL4A1	basement membrane	basement membrane ⁸⁹
COL4A2	basement membrane	basement membrane
COL4A3	basement membrane	basement membrane ⁹⁰
COL4A4	basement membrane	basement membrane ⁹⁰
COL4A5	basement membrane	basement membrane ⁹⁰
COL4A6	basement membrane	basement membrane ⁹¹
COL5A1	interstitial matrix	interstitial matrix ⁹²
COL5A2	interstitial matrix	interstitial matrix ⁹²
COL5A3	interstitial matrix	interstitial matrix ⁹²
COL6A1	interstitial matrix	interstitial matrix ^{2,93} ; interacts with basement membrane ⁹⁴
COL6A2	interstitial matrix	interstitial matrix ^{2,93} interacts with basement membrane ⁹⁴
COL6A3	interstitial matrix	interstitial matrix ^{2,93,95} ; interacts with basement membrane ⁹⁴
COL6A4	interstitial matrix	interstitial matrix ⁹⁵
COL6A5	interstitial matrix	interstitial matrix ⁹⁵
COL6A6	interstitial matrix	interstitial matrix ⁹⁵
COL7A1	basement membrane	
COL8A1	basement membrane	
COL8A2	basement membrane	
COL9A1	interstitial matrix	interstitial matrix ⁷⁴
COL9A2	interstitial matrix	
COL9A3	interstitial matrix	
ACAN	interstitial matrix	interstitial matrix ⁹⁶
ASPN	interstitial matrix	interstitial matrix ⁹⁷
BCAN	interstitial matrix	
BGN	interstitial matrix	interstitial matrix ⁹⁸
CHAD	interstitial matrix	
CHADL	interstitial matrix	
DCN	interstitial matrix	interstitial matrix ^{22,99}
EPYC	interstitial matrix	
ESM1	interstitial matrix	

FMOD	interstitial matrix	
HAPLN1	interstitial matrix	interstitial matrix ¹⁰⁰
HAPLN2	interstitial matrix	
HAPLN3	interstitial matrix	
HAPLN4	interstitial matrix	
HSPG2	basement membrane	basement membrane ¹⁰¹
IMPG1	interstitial matrix	
IMPG2	interstitial matrix	
KERA	interstitial matrix	
LUM	interstitial matrix	interstitial matrix ⁹⁸
NCAN	interstitial matrix	
NEPN	interstitial matrix	
NYX	interstitial matrix	
OGN	interstitial matrix	interstitial matrix ¹⁰²
OMD	interstitial matrix	
OPTC	interstitial matrix	
PODN	interstitial matrix	
PODNL1	interstitial matrix	
PRELP	interstitial matrix	interstitial matrix ¹⁰³ , interacts with the basement membrane ¹⁰³
PRG2	interstitial matrix	
PRG3	interstitial matrix	
PRG4	interstitial matrix	
SPOCK1	interstitial matrix	
SPOCK2	interstitial matrix	
SPOCK3	interstitial matrix	
SRGN	interstitial matrix	
VCAN	interstitial matrix	interstitial matrix ¹⁰⁴
ANXA1	other	
ANXA10	other	
ANXA11	other	
ANXA13	other	
ANXA2	other	
ANXA3	other	
ANXA4	other	
ANXA5	other	
ANXA6	other	
ANXA7	other	
ANXA8	other	
ANXA9	other	
C1QA	other	
C1QB	other	
C1QC	other	
C1QL1	other	
C1QL2	other	
C1QL3	other	

C1QL4	other	
C1QTNF1	other	
C1QTNF2	other	
C1QTNF3	other	
C1QTNF4	other	
C1QTNF5	other	
C1QTNF6	other	
C1QTNF7	other	
C1QTNF9	other	
CD209A	other	
CD209B	other	
CD209D	other	
CLC	other	
CLEC10A	other	
CLEC11A	other	
CLEC12A	other	
CLEC12B	other	
CLEC14A	other	
CLEC18A	other	
CLEC1A	other	
CLEC1B	other	
CLEC2D	other	
CLEC2E	other	
CLEC2G	other	
CLEC2H	other	
CLEC2I	other	
CLEC2J	other	
CLEC2L	other	
CLEC3A	other	
CLEC3B	other	
CLEC4A1	other	
CLEC4A2	other	
CLEC4A3	other	
CLEC4A4	other	
CLEC4B1	other	
CLEC4B2	other	
CLEC4D	other	
CLEC4E	other	
CLEC4F	other	
CLEC4G	other	
CLEC4N	other	
CLEC5A	other	
CLEC7A	other	
CLEC9A	other	
COLEC10	other	
COLEC11	other	

COLEC12	other	
CSPG4	other	
CSPG5	other	
ELFN1	other	
ELFN2	other	
EMCN	other	
FCNA	other	
FCNB	other	
FREM1	basement membrane	basement membrane ^{26,27}
FREM2	basement membrane	basement membrane ^{26,27}
FREM3	basement membrane	basement membrane ¹⁰⁵
GM7534	other	
GM9573	other	
GPC1	other	
GPC2	other	
GPC3	other	
GPC4	other	
GPC5	other	
GPC6	other	
GREM1	other	
GRIFIN	other	
HPX	other	
ITLN1	other	
ITLNB	other	
LGALS1	other	
LGALS12	other	
LGALS2	other	
LGALS3	other	
LGALS4	other	
LGALS6	other	
LGALS7	other	
LGALS8	other	
LGALS9	other	
LGALSL	other	
LMAN1	other	
LMAN1L	other	
MBL1	other	
MBL2	other	
MUC1	other	
MUC13	other	
MUC15	other	
MUC16	other	
MUC19	other	
MUC2	other	
MUC20	other	

MUC3	other	
MUC4	other	
MUC5AC	other	
MUC5B	other	
MUC6	other	
MUCL1	other	
OVGP1	other	
PARM1	other	
PLXDC1	other	
PLXDC2	other	
PLXNA1	other	
PLXNA2	other	
PLXNA3	other	
PLXNA4	other	
PLXNB1	other	
PLXNB2	other	
PLXNB3	other	
PLXNC1	other	
PLXND1	other	
PROL1	other	
REG1	other	
REG2	other	
REG3A	other	
REG3B	other	
REG3D	other	
REG3G	other	
REG4	other	
SDC1	other	
SDC2	other	
SDC3	other	
SDC4	other	
SEMA3A	other	
SEMA3B	other	
SEMA3C	other	
SEMA3D	other	
SEMA3E	other	
SEMA3F	other	
SEMA3G	other	
SEMA4A	other	
SEMA4B	other	
SEMA4C	other	
SEMA4D	other	
SEMA4F	other	
SEMA4G	other	
SEMA5A	other	

SEMA5B	other	
SEMA6A	other	
SEMA6B	other	
SEMA6C	other	
SEMA6D	other	
SEMA7A	other	
SFTA2	other	
SFTPA1	other	
SFTPB	other	
SFTPC	other	
SFTPD	other	
1810010H24RIK	other	
2010005H15RIK	other	
8030411F24RIK	other	
9230104L09RIK	other	
A2M	other	
ADAM10	other	
ADAM11	other	
ADAM12	other	
ADAM15	other	
ADAM17	other	
ADAM18	other	
ADAM19	other	
ADAM1A	other	
ADAM1B	other	
ADAM2	other	
ADAM20	other	
ADAM21	other	
ADAM22	other	
ADAM23	other	
ADAM24	other	
ADAM25	other	
ADAM26A	other	
ADAM26B	other	
ADAM28	other	
ADAM29	other	
ADAM3	other	
ADAM30	other	
ADAM32	other	
ADAM33	other	
ADAM34	other	
ADAM39	other	
ADAM4	other	
ADAM5	other	
ADAM6A	other	
ADAM6B	other	

ADAM7	other	
ADAM8	other	
ADAM9	other	
ADAMDEC1	other	
ADAMTS1	other	
ADAMTS10	other	
ADAMTS12	other	
ADAMTS13	other	
ADAMTS14	other	
ADAMTS15	other	
ADAMTS16	other	
ADAMTS17	other	
ADAMTS18	other	
ADAMTS19	other	
ADAMTS2	other	
ADAMTS20	other	
ADAMTS3	other	
ADAMTS4	other	
ADAMTS5	other	
ADAMTS6	other	
ADAMTS7	other	
ADAMTS8	other	
ADAMTS9	other	
ADAMTSL1	other	
ADAMTSL2	other	
ADAMTSL3	other	
ADAMTSL4	other	
ADAMTSL5	other	
AGT	other	
AI182371	other	
AMBP	other	
ASTL	other	
BC048546	other	
BC051665	other	
BC100530	other	
BC117090	other	
BMP1	other	
CD109	other	
CELA1	other	
CELA2A	other	
CELA3B	other	
CPN2	other	
CST10	other	
CST11	other	
CST12	other	
CST13	other	

CST3	other	
CST6	other	
CST7	other	
CST8	other	
CST9	other	
CSTA1	other	
CSTB	other	
CSTL1	other	
CTS3	other	
CTS6	other	
CTS7	other	
CTS8	other	
CTSA	other	
CTSB	other	
CTSC	other	
CTSD	other	
CTSE	other	
CTSF	other	
CTSG	other	
CTSH	other	
CTSJ	other	
CTSK	other	
CTSL	other	
CTSLL3	other	
CTSM	other	
CTSO	other	
CTSQ	other	
CTSR	other	
CTSS	other	
CTSW	other	
CTSZ	other	
EGLN1	other	
EGLN2	other	
EGLN3	other	
ELANE	other	
F10	other	
F12	other	
F13A1	other	
F13B	other	
F2	other	
F7	other	
F9	other	
FAM20A	other	
FAM20B	other	
FAM20C	other	
GM10334	other	

GM13011	other	
GM4758	other	
GM4787	other	
GM5347	other	
GM5409	other	
GM5416	other	
GM5483	other	
GM5771	other	
HABP2	other	
HPSE	other	
HPSE2	other	
HRG	other	
HTRA1	other	
HTRA3	other	
HTRA4	other	
HYAL1	other	
HYAL2	other	
HYAL3	other	
HYAL4	other	
HYAL5	other	
HYAL6	other	
ITIH1	other	
ITIH2	other	
ITIH3	other	
ITIH4	other	
ITIH5	other	
KAZALD1	other	
KNG1	other	
KNG2	other	
KY	other	
LEPRE1	other	
LEPREL1	other	
LEPREL2	other	
LOX	other	
LOXL1	other	
LOXL2	other	
LOXL3	other	
LOXL4	other	
MASP1	other	
MASP2	other	
MEP1A	other	
MEP1B	other	
MMP10	other	
MMP11	other	
MMP12	other	
MMP13	other	

MMP14	other	
MMP15	other	
MMP16	other	
MMP17	other	
MMP19	other	
MMP1A	other	
MMP1B	other	
MMP2	other	
MMP20	other	
MMP21	other	
MMP23	other	
MMP24	other	
MMP25	other	
MMP27	other	
MMP28	other	
MMP3	other	
MMP7	other	
MMP8	other	
MMP9	other	
MUG2	other	
NGLY1	other	
OGFOD1	other	
OGFOD2	other	
P4HA1	other	
P4HA2	other	
P4HA3	other	
P4HTM	other	
PAMR1	other	
PAPPA	other	
PAPPA2	other	
PCSK5	other	
PCSK6	other	
PLAT	other	
PLAU	other	
PLG	other	
PLOD1	other	
PLOD2	other	
PLOD3	other	
PRSS1	other	
PRSS12	other	
PRSS2	other	
PRSS3	other	
PZP	other	
SERPINA10	other	
SERPINA11	other	

SERPINA12	other	
SERPINA1A	other	
SERPINA1B	other	
SERPINA1C	other	
SERPINA1D	other	
SERPINA1E	other	
SERPINA1F	other	
SERPINA3A	other	
SERPINA3B	other	
SERPINA3C	other	
SERPINA3F	other	
SERPINA3G	other	
SERPINA3K	other	
SERPINA3M	other	
SERPINA3N	other	
SERPINA5	other	
SERPINA6	other	
SERPINA7	other	
SERPINA9	other	
SERPINB10	other	
SERPINB11	other	
SERPINB12	other	
SERPINB13	other	
SERPINB1A	other	
SERPINB1B	other	
SERPINB1C	other	
SERPINB2	other	
SERPINB3A	other	
SERPINB3B	other	
SERPINB3C	other	
SERPINB3D	other	
SERPINB5	other	
SERPINB6A	other	
SERPINB6B	other	
SERPINB6C	other	
SERPINB6D	other	
SERPINB7	other	
SERPINB8	other	
SERPINB9	other	
SERPINB9B	other	
SERPINB9C	other	
SERPINB9D	other	
SERPINB9E	other	
SERPINB9F	other	
SERPINB9G	other	
SERPINC1	other	

SERPIND1	other	
SERPINE1	other	
SERPINE2	other	
SERPINE3	other	
SERPINF1	other	
SERPINF2	other	
SERPING1	other	
SERPINH1	other	
SERPINI1	other	
SERPINI2	other	
SLPI	other	
SPAM1	other	
SPINKL	other	
ST14	other	
STFA1	other	
STFA2	other	
STFA2L1	other	
STFA3	other	
SULF1	other	
SULF2	other	
TGM1	other	
TGM2	other	
TGM3	other	
TGM4	other	
TGM5	other	
TGM6	other	
TGM7	other	
TIMP1	other	
TIMP2	other	
TIMP3	other	
TIMP4	other	
TLL1	other	
TLL2	other	
TMPRSS15	other	
TPBPA	other	
TPBPB	other	
TRY10	other	
TRY4	other	
TRY5	other	
U06147	other	
AMH	other	
ANGPT1	other	
ANGPT2	other	
ANGPT4	other	
ANGPTL1	other	
ANGPTL2	other	

ANGPTL3	other	
ANGPTL4	other	
ANGPTL6	other	
ANGPTL7	other	
AREG	other	
ARTN	other	
BDNF	other	
BMP10	other	
BMP15	other	
BMP2	other	
BMP3	other	
BMP4	other	
BMP5	other	
BMP6	other	
BMP7	other	
BMP8A	other	
BMP8B	other	
BRINP2	other	
BRINP3	other	
BTC	other	
CBLN1	other	
CBLN2	other	
CBLN3	other	
CBLN4	other	
CCBE1	other	
CCL1	other	
CCL11	other	
CCL12	other	
CCL17	other	
CCL19	other	
CCL2	other	
CCL20	other	
CCL21A	other	
CCL21B	other	
CCL21C	other	
CCL22	other	
CCL24	other	
CCL25	other	
CCL26	other	
CCL27A	other	
CCL28	other	
CCL3	other	
CCL4	other	
CCL5	other	
CCL6	other	
CCL7	other	

CCL8	other	
CCL9	other	
CFC1	other	
CHRD	other	
CHRD1	other	
CHRD2	other	
CLCF1	other	
CNTF	other	
CRHBP	other	
CRLF1	other	
CRLF3	other	
CRNN	other	
CSF1	other	
CSF2	other	
CSF3	other	
CTF1	other	
CTF2	other	
CX3CL1	other	
CXCL1	other	
CXCL10	other	
CXCL11	other	
CXCL12	other	
CXCL13	other	
CXCL14	other	
CXCL15	other	
CXCL2	other	
CXCL3	other	
CXCL5	other	
CXCL9	other	
DHH	other	
EBI3	other	
EDA	other	
EGF	other	
EGFL6	other	
EGFL7	other	
EGFL8	other	
EPGN	other	
EPO	other	
EREG	other	
FAM132A	other	
FAM132B	other	
FASL	other	
FGF1	other	
FGF10	other	
FGF11	other	
FGF12	other	

FGF13	other	
FGF14	other	
FGF15	other	
FGF16	other	
FGF17	other	
FGF18	other	
FGF2	other	
FGF20	other	
FGF21	other	
FGF22	other	
FGF23	other	
FGF3	other	
FGF4	other	
FGF5	other	
FGF6	other	
FGF7	other	
FGF8	other	
FGF9	other	
FGFBP1	other	
FGFBP3	other	
FIGF	other	
FLG	other	
FLG2	other	
FLT3L	other	
FRZB	other	
FST	other	
FSTL1	other	
FSTL3	other	
GDF1	other	
GDF10	other	
GDF11	other	
GDF15	other	
GDF2	other	
GDF3	other	
GDF5	other	
GDF6	other	
GDF7	other	
GDF9	other	
GDNF	other	
GH	other	
GM13271	other	
GM13272	other	
GM13275	other	
GM13276	other	
GM13277	other	
GM13278	other	

GM13279	other	
GM13283	other	
GM13285	other	
GM13287	other	
GM13288	other	
GM13289	other	
GM13290	other	
GM13306	other	
GM5849	other	
HBEGF	other	
HCFC1	other	
HCFC2	other	
HGF	other	
HGFAC	other	
HHIP	other	
HRNR	other	
IFNA1	other	
IFNA11	other	
IFNA12	other	
IFNA13	other	
IFNA14	other	
IFNA15	other	
IFNA16	other	
IFNA2	other	
IFNA4	other	
IFNA5	other	
IFNA6	other	
IFNA7	other	
IFNA9	other	
IFNAB	other	
IFNB1	other	
IFNE	other	
IFNG	other	
IFNK	other	
IFNZ	other	
IGF1	other	
IGF2	other	
IHH	other	
IL10	other	
IL11	other	
IL12A	other	
IL12B	other	
IL13	other	
IL15	other	
IL16	other	
IL17A	other	

IL17B	other	
IL17C	other	
IL17D	other	
IL17F	other	
IL18	other	
IL19	other	
IL1A	other	
IL1B	other	
IL1F10	other	
IL1F5	other	
IL1F6	other	
IL1F8	other	
IL1F9	other	
IL1RN	other	
IL2	other	
IL20	other	
IL22	other	
IL23A	other	
IL24	other	
IL25	other	
IL3	other	
IL34	other	
IL4	other	
IL5	other	
IL6	other	
IL7	other	
IL9	other	
INHA	other	
INHBA	other	
INHBB	other	
INHBC	other	
INHBE	other	
INS1	other	
INS2	other	
INSL3	other	
INSL5	other	
INSL6	other	
ISM1	other	
ISM2	other	
KITL	other	
LEFTY1	other	
LEFTY2	other	
LEP	other	
LIF	other	
LTA	other	
LTB	other	

MDK	other	
MEGF10	other	
MEGF11	other	
MEGF6	other	
MEGF8	other	
MEGF9	other	
MST1	other	
MSTN	other	
NGF	other	
NODAL	other	
NRG1	other	
NRG2	other	
NRG3	other	
NRG4	other	
NRTN	other	
NTF3	other	
NTF5	other	
OSM	other	
PDGFA	other	
PDGFB	other	
PDGFC	other	
PDGFD	other	
PF4	other	
PGF	other	
PIK3IP1	other	
PPBP	other	
PRL	other	
PRL2A1	other	
PRL2B1	other	
PRL2C1	other	
PRL2C2	other	
PRL2C3	other	
PRL2C4	other	
PRL2C5	other	
PRL3A1	other	
PRL3B1	other	
PRL3C1	other	
PRL3D1	other	
PRL3D2	other	
PRL3D3	other	
PRL4A1	other	
PRL5A1	other	
PRL6A1	other	
PRL7A1	other	
PRL7A2	other	
PRL7B1	other	

PRL7C1	other	
PRL7D1	other	
PRL8A1	other	
PRL8A2	other	
PRL8A6	other	
PRL8A8	other	
PRL8A9	other	
PSPN	other	
PTN	other	
RPTN	other	
S100A1	other	
S100A10	other	
S100A11	other	
S100A13	other	
S100A14	other	
S100A16	other	
S100A2	other	
S100A3	other	
S100A4	other	
S100A5	other	
S100A6	other	
S100A7A	other	
S100A8	other	
S100A9	other	
S100B	other	
S100G	other	
S100Z	other	
SCUBE1	other	
SCUBE2	other	
SCUBE3	other	
SFRP1	other	
SFRP2	other	
SFRP4	other	
SFRP5	other	
SHH	other	
TCHH	other	
TCHHL1	other	
TDGF1	other	
TGFA	other	
TGFB1	other	
TGFB2	other	
TGFB3	other	
THPO	other	
TNF	other	
TNFSF10	other	
TNFSF11	other	

TNFSF12	other	
TNFSF12TNFSF13	other	
TNFSF13	other	
TNFSF13B	other	
TNFSF14	other	
TNFSF15	other	
TNFSF18	other	
TNFSF4	other	
TNFSF8	other	
TNFSF9	other	
TPO	other	
VEGFA	other	
VEGFB	other	
VEGFC	other	
VWC2	other	
VWC2L	other	
WFIKKN1	other	
WFIKKN2	other	
WIF1	other	
WNT1	other	
WNT10A	other	
WNT10B	other	
WNT11	other	
WNT16	other	
WNT2	other	
WNT2B	other	
WNT3	other	
WNT3A	other	
WNT4	other	
WNT5A	other	
WNT5B	other	
WNT6	other	
WNT7A	other	
WNT7B	other	
WNT8A	other	
WNT8B	other	
WNT9A	other	
WNT9B	other	
XCL1	other	
1110031102RIK	other	
CCL16-PS	other	
E030019B13RIK	other	
GM13286	other	
GM13308	other	
GM5065	other	
GM8080	other	

IFNA10	other	
ITIH5L-PS	other	
MUC12	other	
SERPINA3H	other	
SERPINA4-PS1	other	
TNXA	other	
ZFP91-CNTF	other	
ZP4-PS	other	

References:

1. Byron, A, Humphries, JD, Humphries, MJ: Defining the extracellular matrix using proteomics. *Int J Exp Pathol*, 94: 75-92, 2013.
2. Lennon, R, Byron, A, Humphries, JD, Randles, MJ, Carisey, A, Murphy, S, Knight, D, Brenchley, PE, Zent, R, Humphries, MJ: Global analysis reveals the complexity of the human glomerular extracellular matrix. *J Am Soc Nephrol*, 25: 939-951, 2014.
3. Tsutsui, K, Machida, H, Morita, R, Nakagawa, A, Sekiguchi, K, Miner, JH, Fujiwara, H: Mapping the molecular and structural specialization of the skin basement membrane for inter-tissue interactions. *bioRxiv*: 2020.2004.2027.061952, 2020.
4. Harvey, SJ, Jarad, G, Cunningham, J, Rops, AL, van der Vlag, J, Berden, JH, Moeller, MJ, Holzman, LB, Burgess, RW, Miner, JH: Disruption of glomerular basement membrane charge through podocyte-specific mutation of agrin does not alter glomerular permselectivity. *Am J Pathol*, 171: 139-152, 2007.
5. Svensson, L, Aszodi, A, Heinegard, D, Hunziker, EB, Reinholt, FP, Fassler, R, Oldberg, A: Cartilage oligomeric matrix protein-deficient mice have normal skeletal development. *Mol Cell Biol*, 22: 4366-4371, 2002.
6. Krishnaswamy, VR, Korrapati, PS: Role of dermatopontin in re-epithelialization: implications on keratinocyte migration and proliferation. *Sci Rep*, 4: 7385, 2014.
7. Fan, W, Liu, T, Chen, W, Hammad, S, Longerich, T, Hausser, I, Fu, Y, Li, N, He, Y, Liu, C, Zhang, Y, Lian, Q, Zhao, X, Yan, C, Li, L, Yi, C, Ling, Z, Ma, L, Zhao, X, Xu, H, Wang, P, Cong, M, You, H, Liu, Z, Wang, Y, Chen, J, Li, D, Hui, L, Dooley, S, Hou, J, Jia, J, Sun, B: ECM1 Prevents Activation of Transforming Growth Factor β , Hepatic Stellate Cells, and Fibrogenesis in Mice. *Gastroenterology*, 157: 1352-1367.e1313, 2019.
8. McLaughlin, PJ, Bakall, B, Choi, J, Liu, Z, Sasaki, T, Davis, EC, Marmorstein, AD, Marmorstein, LY: Lack of fibulin-3 causes early aging and herniation, but not macular degeneration in mice. *Hum Mol Genet*, 16: 3059-3070, 2007.
9. Votteler, M, Berrio, DAC, Horke, A, Sabatier, L, Reinhardt, DP, Nsair, A, Aikawa, E, Schenke-Layland, K: Elastogenesis at the onset of human cardiac valve development. *Development* 140: 2345-2353, 2013.
10. Nandhu, MS, Hu, B, Cole, SE, Erdreich-Epstein, A, Rodriguez-Gil, DJ, Viapiano, MS: Novel paracrine modulation of Notch-DLL4 signaling by fibulin-3 promotes angiogenesis in high-grade gliomas. *Cancer research*, 74: 5435-5448, 2014.
11. McLaughlin, PJ, Chen, Q, Horiguchi, M, Starcher, BC, Stanton, JB, Broekelmann, TJ, Marmorstein, AD, McKay, B, Mecham, R, Nakamura, T, Marmorstein, LY: Targeted disruption of fibulin-4 abolishes elastogenesis and causes perinatal lethality in mice. *Mol Cell Biol*, 26: 1700-1709, 2006.
12. Halabi, CM, Broekelmann, TJ, Lin, M, Lee, VS, Chu, ML, Mecham, RP: Fibulin-4 is essential for maintaining arterial wall integrity in conduit but not muscular arteries. *Sci Adv*, 3: e1602532, 2017.
13. Leimeister, C, Steidl, C, Schumacher, N, Erhard, S, Gessler, M: Developmental expression and biochemical characterization of Emu family members. *Dev Biol*, 249: 204-218, 2002.
14. Sterzel, RB, Hartner, A, Schlotzer-Schrehardt, U, Voit, S, Hausknecht, B, Doliana, R, Colombatti, A, Gibson, MA, Braghetta, P, Bressan, GM: Elastic fiber proteins in the glomerular mesangium in vivo and in cell culture. *Kidney Int*, 58: 1588-1602, 2000.
15. Louzao-Martinez, L, van Dijk, CGM, Xu, YJ, Korn, A, Bekker, NJ, Brouwhuis, R, Nicese, MN, Demmers, JAA, Goumans, M-JTH, Masereeuw, R, Duncker, DJ, Verhaar, MC, Cheng, C: A proteome comparison between human fetal and mature renal extracellular matrix identifies EMILIN1 as a regulator of renal epithelial cell adhesion. *Matrix Bio Plus*, 4, 2019.
16. Schiavinato, A, Keene, DR, Imhof, T, Doliana, R, Sasaki, T, Sengle, G: Fibulin-4 deposition requires EMILIN-1 in the extracellular matrix of osteoblasts. *Sci Rep*, 7: 5526, 2017.
17. Kostka, G, Giltay, R, Bloch, W, Addicks, K, Timpl, R, Fassler, R, Chu, ML: Perinatal lethality and endothelial cell abnormalities in several vessel compartments of fibulin-1-deficient mice. *Mol Cell Biol*, 21: 7025-7034, 2001.
18. Uhlén, M, Fagerberg, L, Hallström, BM, Lindskog, C, Oksvold, P, Mardinoglu, A, Sivertsson, Å, Kampf, C, Sjöstedt, E, Asplund, A, Olsson, I, Edlund, K, Lundberg, E, Navani, S, Szgyarto, CA-K, Odeberg, J, Djureinovic, D, Takanen, JO, Hober, S, Alm, T, Edqvist, P-H, Berling, H, Tegel, H, Mulder, J, Rockberg, J, Nilsson, P, Schwenk, JM, Hamsten, M, von Feilitzen, K, Forsberg, M, Persson, L, Johansson, F, Zwahlen, M, von Heijne, G, Nielsen, J, Pontén, F: Tissue-based map of the human proteome. *Science*, 347: 1260419, 2015.
19. Fujiwara, H, Ferreira, M, Donati, G, Marciano, DK, Linton, JM, Sato, Y, Hartner, A, Sekiguchi, K, Reichardt, LF, Watt, FM: The basement membrane of hair follicle stem cells is a muscle cell niche. *Cell*, 144: 577-589, 2011.
20. Yanagisawa, H, Davis, EC, Starcher, BC, Ouchi, T, Yanagisawa, M, Richardson, JA, Olson, EN: Fibulin-5 is an elastin-binding protein essential for elastic fibre development in vivo. *Nature*, 415: 168-171, 2002.

21. Nakamura, T, Lozano, PR, Ikeda, Y, Iwanaga, Y, Hinek, A, Minamisawa, S, Cheng, CF, Kobuke, K, Dalton, N, Takada, Y, Tashiro, K, Ross, J, Jr., Honjo, T, Chien, KR: Fibulin-5/DANCE is essential for elastogenesis in vivo. *Nature*, 415: 171-175, 2002.
22. Rickelt, S, Hynes, RO: Antibodies and methods for immunohistochemistry of extracellular matrix proteins. *Matrix Biology*, 71-72: 10-27, 2018.
23. Quondamatteo, F, Reinhardt, DP, Charbonneau, NL, Pophal, G, Sakai, LY, Herken, R: Fibrillin-1 and fibrillin-2 in human embryonic and early fetal development. *Matrix Biol*, 21: 637-646, 2002.
24. Hartner, A, Schaefer, L, Porst, M, Cordasic, N, Gabriel, A, Klanke, B, Reinhardt, DP, Hilgers, KF: Role of fibrillin-1 in hypertensive and diabetic glomerular disease. *Am J Physiol-Renal*, 290: F1329-F1336, 2006.
25. Arteaga-Solis, E, Gayraud, B, Lee, SY, Shum, L, Sakai, L, Ramirez, F: Regulation of limb patterning by extracellular microfibrils. *J Cell Biol*, 154: 275-281, 2001.
26. Petrou, P, Pavlakakis, E, Dalezios, Y, Chalepakakis, G: Basement membrane localization of Frem3 is independent of the Fras1/Frem1/Frem2 protein complex within the sublamina densa. *Matrix Biol*, 26: 652-658, 2007.
27. Kiyozumi, D, Sugimoto, N, Sekiguchi, K: Breakdown of the reciprocal stabilization of QBRICK/Frem1, Fras1, and Frem2 at the basement membrane provokes Fraser syndrome-like defects. *Proc Natl Acad Sci U S A*, 103: 11981-11986, 2006.
28. Tomimaru, Y, Eguchi, H, Wada, H, Kobayashi, S, Marubashi, S, Tanemura, M, Umeshita, K, Kim, T, Wakasa, K, Doki, Y, Mori, M, Nagano, H: IGFBP7 downregulation is associated with tumor progression and clinical outcome in hepatocellular carcinoma. *International Journal of Cancer*, 130: 319-327, 2012.
29. Lin, J, Patel, SR, Cheng, X, Cho, EA, Levitan, I, Ullenbruch, M, Phan, SH, Park, JM, Dressler, GR: Kielin/chordin-like protein, a novel enhancer of BMP signaling, attenuates renal fibrotic disease. *Nat Med*, 11: 387-393, 2005.
30. Ning, L, Kurihara, H, de Vega, S, Ichikawa-Tomikawa, N, Xu, Z, Nonaka, R, Kazuno, S, Yamada, Y, Miner, JH, Arikawa-Hirasawa, E: Laminin $\alpha 1$ regulates age-related mesangial cell proliferation and mesangial matrix accumulation through the TGF- β pathway. *Am J Pathol*, 184: 1683-1694, 2014.
31. Cosgrove, D, Rodgers, K, Meehan, D, Miller, C, Bovard, K, Gilroy, A, Gardner, H, Kotelianski, V, Gotwals, P, Amatucci, A, Kalluri, R: Integrin $\alpha 1 \beta 1$ and Transforming Growth Factor- $\beta 1$ Play Distinct Roles in Alport Glomerular Pathogenesis and Serve as Dual Targets for Metabolic Therapy. *The American Journal of Pathology*, 157: 1649-1659, 2000.
32. KASHTAN, CE, KIM, Y, LEES, GE, THORNER, PS, VIRTANEN, I, MINER, JH: Abnormal Glomerular Basement Membrane Laminins in Murine, Canine, and Human Alport Syndrome: Aberrant Laminin $\alpha 2$ Deposition Is Species Independent. *Journal of the American Society of Nephrology*, 12: 252-260, 2001.
33. Abrass, CK, Berfield, AK, Ryan, MC, Carter, WG, Hansen, KM: Abnormal development of glomerular endothelial and mesangial cells in mice with targeted disruption of the lama3 gene. *Kidney Int*, 70: 1062-1071, 2006.
34. Abrass, CK, Hansen, KM, Patton, BL: Laminin alpha4-null mutant mice develop chronic kidney disease with persistent overexpression of platelet-derived growth factor. *Am J Pathol*, 176: 839-849, 2010.
35. Miner, JH, Li, C: Defective glomerulogenesis in the absence of laminin alpha5 demonstrates a developmental role for the kidney glomerular basement membrane. *Dev Biol*, 217: 278-289, 2000.
36. .
37. Miner, JH, Li, C, Mudd, JL, Go, G, Sutherland, AE: Compositional and structural requirements for laminin and basement membranes during mouse embryo implantation and gastrulation. *Development*, 131: 2247-2256, 2004.
38. Zenker, M, Aigner, T, Wendler, O, Tralau, T, Muntefering, H, Fenski, R, Pitz, S, Schumacher, V, Royer-Pokora, B, Wuhl, E, Cochat, P, Bouvier, R, Kraus, C, Mark, K, Madlon, H, Dotsch, J, Rascher, W, Maruniak-Chudek, I, Lennert, T, Neumann, LM, Reis, A: Human laminin beta2 deficiency causes congenital nephrosis with mesangial sclerosis and distinct eye abnormalities. *Hum Mol Genet*, 13: 2625-2632, 2004.
39. Vijayakumar, S, Dang, S, Marinkovich, MP, Lazarova, Z, Yoder, B, Torres, VE, Wallace, DP: Aberrant expression of laminin-332 promotes cell proliferation and cyst growth in ARPKD. *Am J Physiol Renal Physiol*, 306: F640-654, 2014.
40. Willem, M, Miosge, N, Halfter, W, Smyth, N, Jannetti, I, Burghart, E, Timpl, R, Mayer, U: Specific ablation of the nidogen-binding site in the laminin gamma1 chain interferes with kidney and lung development. *Development*, 129: 2711-2722, 2002.
41. Isogai, Z, Ono, RN, Ushiro, S, Keene, DR, Chen, Y, Mazzieri, R, Charbonneau, NL, Reinhardt, DP, Rifkin, DB, Sakai, LY: Latent transforming growth factor beta-binding protein 1 interacts with fibrillin and is a microfibril-associated protein. *J Biol Chem*, 278: 2750-2757, 2003.
42. Hirani, R, Hanssen, E, Gibson, MA: LTBP-2 specifically interacts with the amino-terminal region of fibrillin-1 and competes with LTBP-1 for binding to this microfibrillar protein. *Matrix Biol*, 26: 213-223, 2007.

43. Dabovic, B, Chen, Y, Colarossi, C, Obata, H, Zambuto, L, Perle, MA, Rifkin, DB: Bone abnormalities in latent TGF-[beta] binding protein (Ltbp)-3-null mice indicate a role for Ltbp-3 in modulating TGF-[beta] bioavailability. *J Cell Biol*, 156: 227-232, 2002.
44. Noda, K, Dabovic, B, Takagi, K, Inoue, T, Horiguchi, M, Hirai, M, Fujikawa, Y, Akama, TO, Kusumoto, K, Zilberberg, L, Sakai, LY, Koli, K, Naitoh, M, von Melchner, H, Suzuki, S, Rifkin, DB, Nakamura, T: Latent TGF- β binding protein 4 promotes elastic fiber assembly by interacting with fibulin-5. *Proc Natl Acad Sci USA*, 110: 2852-2857, 2013.
45. Nicolae, C, Ko, YP, Miosge, N, Niehoff, A, Studer, D, Enggist, L, Hunziker, EB, Paulsson, M, Wagener, R, Aszodi, A: Abnormal collagen fibrils in cartilage of matrilin-1/matrilin-3-deficient mice. *J Biol Chem*, 282: 22163-22175, 2007.
46. Zhang, S, Peng, J, Guo, Y, Javidiparsijani, S, Wang, G, Wang, Y, Liu, H, Liu, J, Luo, J: Matrilin-2 is a widely distributed extracellular matrix protein and a potential biomarker in the early stage of osteoarthritis in articular cartilage. *Biomed Res Int*, 2014: 986127, 2014.
47. Klatt, AR, Nitsche, DP, Kobbe, B, Morgelin, M, Paulsson, M, Wagener, R: Molecular structure and tissue distribution of matrilin-3, a filament-forming extracellular matrix protein expressed during skeletal development. *J Biol Chem*, 275: 3999-4006, 2000.
48. Weinbaum, JS, Broekelmann, TJ, Pierce, RA, Werneck, CC, Segade, F, Craft, CS, Knutsen, RH, Mecham, RP: Deficiency in microfibril-associated glycoprotein-1 leads to complex phenotypes in multiple organ systems. *J Biol Chem*, 283: 25533-25543, 2008.
49. Combs, MD, Knutsen, RH, Broekelmann, TJ, Toennies, HM, Brett, TJ, Miller, CA, Kober, DL, Craft, CS, Atkinson, JJ, Shipley, JM, Trask, BC, Mecham, RP: Microfibril-associated glycoprotein 2 (MAGP2) loss of function has pleiotropic effects in vivo. *J Biol Chem*, 288: 28869-28880, 2013.
50. Colombatti, A, Spessotto, P, Doliana, R, Mongiat, M, Bressan, GM, Esposito, G: The EMILIN/Multimerin family. *Front Immunol*, 2: 93, 2011.
51. Bader, BL, Smyth, N, Nedbal, S, Miosge, N, Baranowsky, A, Mokkalapati, S, Murshed, M, Nischt, R: Compound genetic ablation of nidogen 1 and 2 causes basement membrane defects and perinatal lethality in mice. *Mol Cell Biol*, 25: 6846-6856, 2005.
52. Muller-Deile, J, Dannenberg, J, Schroder, P, Lin, MH, Miner, JH, Chen, R, Brasen, JH, Thum, T, Nystrom, J, Staggs, LB, Haller, H, Fiedler, J, Lorenzen, JM, Schiffer, M: Podocytes regulate the glomerular basement membrane protein nephronection by means of miR-378a-3p in glomerular diseases. *Kidney Int*, 92: 836-849, 2017.
53. Zimmerman, SE, Hiremath, C, Tsunozumi, J, Yang, Z, Finney, B, Marciano, DK: Nephronection Regulates Mesangial Cell Adhesion and Behavior in Glomeruli. *J Am Soc Nephrol*, 29: 1128-1140, 2018.
54. Manabe, R, Tsutsui, K, Yamada, T, Kimura, M, Nakano, I, Shimono, C, Sanzen, N, Furutani, Y, Fukuda, T, Oguri, Y, Shimamoto, K, Kiyozumi, D, Sato, Y, Sado, Y, Senoo, H, Yamashina, S, Fukuda, S, Kawai, J, Sugiura, N, Kimata, K, Hayashizaki, Y, Sekiguchi, K: Transcriptome-based systematic identification of extracellular matrix proteins. *Proc Natl Acad Sci U S A*, 105: 12849-12854, 2008.
55. Kudo, A: *Periostin*, Singapore : Springer Singapore : Imprint: Springer, 2019.
56. Sorocos, K, Kostoulas, X, Cullen-McEwen, L, Hart, AH, Bertram, JF, Caruana, G: Expression Patterns and Roles of Periostin During Kidney and Ureter Development. *The Journal of Urology*, 186: 1537-1544, 2011.
57. Peterfi, Z, Donko, A, Orient, A, Sum, A, Prokai, A, Molnar, B, Vereb, Z, Rajnavolgyi, E, Kovacs, KJ, Muller, V, Szabo, AJ, Geiszt, M: Peroxidasin is secreted and incorporated into the extracellular matrix of myofibroblasts and fibrotic kidney. *Am J Pathol*, 175: 725-735, 2009.
58. Jones-Paris, CR, Paria, S, Berg, T, Saus, J, Bhav, G, Paria, BC, Hudson, BG: Embryo implantation triggers dynamic spatiotemporal expression of the basement membrane toolkit during uterine reprogramming. *Matrix Biology*, 57-58: 347-365, 2017.
59. Bhav, G, Colon, S, Ferrell, N: The sulfilimine cross-link of collagen IV contributes to kidney tubular basement membrane stiffness. *Am J Physiol-Renal*, 313: F596-F602, 2017.
60. Fitzgerald, MC, Schwarzbauer, JE: Importance of the basement membrane protein SPARC for viability and fertility in *Caenorhabditis elegans*. *Curr Biol*, 8: 1285-1288, 1998.
61. Morrissey, MA, Jayadev, R, Miley, GR, Blebea, CA, Chi, Q, Ihara, S, Sherwood, DR: SPARC Promotes Cell Invasion In Vivo by Decreasing Type IV Collagen Levels in the Basement Membrane. *PLoS Genet*, 12: e1005905, 2016.
62. Sun, D, Ma, Y, Han, H, Yin, Z, Liu, C, Feng, J, Zhou, X, Li, X, Xiao, A, Yu, R: Thrombospondin-1 short hairpin RNA suppresses tubulointerstitial fibrosis in the kidney of ureteral obstruction by ameliorating peritubular capillary injury. *Kidney Blood Press Res*, 35: 35-47, 2012.

63. Tsutsui, K, Manabe, R, Yamada, T, Nakano, I, Oguri, Y, Keene, DR, Sengle, G, Sakai, LY, Sekiguchi, K: ADAMTSL-6 is a novel extracellular matrix protein that binds to fibrillin-1 and promotes fibrillin-1 fibril formation. *J Biol Chem*, 285: 4870-4882, 2010.
64. Saito, M, Kurokawa, M, Oda, M, Oshima, M, Tsutsui, K, Kosaka, K, Nakao, K, Ogawa, M, Manabe, R, Suda, N, Ganjargal, G, Hada, Y, Noguchi, T, Teranaka, T, Sekiguchi, K, Yoneda, T, Tsuji, T: ADAMTSL6 β protein rescues fibrillin-1 microfibril disorder in a Marfan syndrome mouse model through the promotion of fibrillin-1 assembly. *J Biol Chem*, 286: 38602-38613, 2011.
65. Miyazato, H, Yoshioka, K, Hino, S, Aya, N, Matsuo, S, Suzuki, N, Suzuki, Y, Sinohara, H, Maki, S: The target antigen of anti-tubular basement membrane antibody-mediated interstitial nephritis. *Autoimmunity*, 18: 259-265, 1994.
66. Butkowski, RJ, Kleppel, MM, Katz, A, Michael, AF, Fish, AJ: Distribution of tubulointerstitial nephritis antigen and evidence for multiple forms. *Kidney Int*, 40: 838-846, 1991.
67. Li, D, Mukai, K, Suzuki, T, Suzuki, R, Yamashita, S, Mitani, F, Suematsu, M: Adrenocortical zonation factor 1 is a novel matricellular protein promoting integrin-mediated adhesion of adrenocortical and vascular smooth muscle cells. *Febs j*, 274: 2506-2522, 2007.
68. Wex, T, Lipyansky, A, Brömme, NC, Wex, H, Guan, XQ, Brömme, D: TIN-ag-RP, a novel catalytically inactive cathepsin B-related protein with EGF domains, is predominantly expressed in vascular smooth muscle cells. *Biochemistry*, 40: 1350-1357, 2001.
69. Truong, LD, Foster, SV, Barrios, R, D'Agati, V, Verani, RR, Gonzalez, JM, Suki, WN: Tenascin is an ubiquitous extracellular matrix protein of human renal interstitium in normal and pathologic conditions. *Nephron*, 72: 579-586, 1996.
70. Gbadegesin, RA, Brophy, PD, Adeyemo, A, Hall, G, Gupta, IR, Hains, D, Bartkowiak, B, Rabinovich, CE, Chandrasekharappa, S, Homstad, A, Westreich, K, Wu, G, Liu, Y, Holanda, D, Clarke, J, Lavin, P, Selim, A, Miller, S, Wiener, JS, Ross, SS, Foreman, J, Rotimi, C, Winn, MP: TNXB mutations can cause vesicoureteral reflux. *J Am Soc Nephrol*, 24: 1313-1322, 2013.
71. Lopez-Guisa, JM, Rassa, AC, Cai, X, Collins, SJ, Eddy, AA: Vitronectin accumulates in the interstitium but minimally impacts fibrogenesis in experimental chronic kidney disease. *Am J Physiol Renal Physiol*, 300: F1244-1254, 2011.
72. Allen, JM, Brachvogel, B, Farlie, PG, Fitzgerald, J, Bateman, JF: The extracellular matrix protein WARP is a novel component of a distinct subset of basement membranes. *Matrix Biol*, 27: 295-305, 2008.
73. van der Ven, AT, Kobbe, B, Kohl, S, Shril, S, Pogoda, HM, Imhof, T, Ityel, H, Vivante, A, Chen, J, Hwang, DY, Connaughton, DM, Mann, N, Widmeier, E, Taglienti, M, Schmidt, JM, Nakayama, M, Senguttuvan, P, Kumar, S, Tasic, V, Kehinde, EO, Mane, SM, Lifton, RP, Soliman, N, Lu, W, Bauer, SB, Hammerschmidt, M, Wagener, R, Hildebrandt, F: A homozygous missense variant in VWA2, encoding an interactor of the Fraser-complex, in a patient with vesicoureteral reflux. *PLoS One*, 13: e0191224, 2018.
74. Chen, Z, Huang, J, Liu, Y, Dattilo, LK, Huh, S-H, Ornitz, D, Beebe, DC: FGF signaling activates a Sox9-Sox10 pathway for the formation and branching morphogenesis of mouse ocular glands. *Development*, 141: 2691-2701, 2014.
75. Veit, G, Hansen, U, Keene, DR, Bruckner, P, Chiquet-Ehrismann, R, Chiquet, M, Koch, M: Collagen XII interacts with avian tenascin-X through its NC3 domain. *J Biol Chem*, 281: 27461-27470, 2006.
76. Bader, HL, Keene, DR, Charvet, B, Veit, G, Driever, W, Koch, M, Ruggiero, F: Zebrafish collagen XII is present in embryonic connective tissue sheaths (fascia) and basement membranes. *Matrix Biology*, 28: 32-43, 2009.
77. Zou, Y, Zwolanek, D, Izu, Y, Gandhi, S, Schreiber, G, Brockmann, K, Devoto, M, Tian, Z, Hu, Y, Veit, G, Meier, M, Stetefeld, J, Hicks, D, Straub, V, Voermans, NC, Birk, DE, Barton, ER, Koch, M, Bonnemann, CG: Recessive and dominant mutations in COL12A1 cause a novel EDS/myopathy overlap syndrome in humans and mice. *Hum Mol Genet*, 23: 2339-2352, 2014.
78. Thierry, L, Geiser, AS, Hansen, A, Tesche, F, Herken, R, Miosge, N: Collagen types XII and XIV are present in basement membrane zones during human embryonic development. *J Mol Histol*, 35: 803-810, 2004.
79. Ansoorge, HL, Meng, X, Zhang, G, Veit, G, Sun, M, Klement, JF, Beason, DP, Soslowsky, LJ, Koch, M, Birk, DE: Type XIV Collagen Regulates Fibrillogenesis: PREMATURE COLLAGEN FIBRIL GROWTH AND TISSUE DYSFUNCTION IN NULL MICE. *J Biol Chem*, 284: 8427-8438, 2009.
80. Berthod, F, Germain, L, Guignard, R, Lethias, C, Garrone, R, Damour, O, van der Rest, M, Auger, FA: Differential Expression of Collagens XII and XIV in Human Skin and in Reconstructed Skin. *Journal of Investigative Dermatology*, 108: 737-742, 1997.
81. Muona, A, Eklund, L, Vaisanen, T, Pihlajaniemi, T: Developmentally regulated expression of type XV collagen correlates with abnormalities in Col15a1(-/-) mice. *Matrix Biol*, 21: 89-102, 2002.

82. Lin, Y, Zhang, S, Rehn, M, Itaranta, P, Tuukkanen, J, Heljasvaara, R, Peltoketo, H, Pihlajaniemi, T, Vainio, S: Induced repatterning of type XVIII collagen expression in ureter bud from kidney to lung type: association with sonic hedgehog and ectopic surfactant protein C. *Development*, 128: 1573-1585, 2001.
83. Alexakis, C, Maxwell, P, Bou-Gharios, G: Organ-specific collagen expression: implications for renal disease. *Nephron Exp Nephrol*, 102: e71-75, 2006.
84. Tsukahara, Y, Tanaka, M, Miyajima, A: TROP2 Expressed in the Trunk of the Ureteric Duct Regulates Branching Morphogenesis during Kidney Development. *PLOS ONE*, 6: e28607, 2011.
85. Ratzinger, S, Eble, JA, Pasoldt, A, Opolka, A, Rogler, G, Grifka, J, Grässel, S: Collagen XVI induces formation of focal contacts on intestinal myofibroblasts isolated from the normal and inflamed intestinal tract. *Matrix Biology*, 29: 177-193, 2010.
86. Sandberg, MM, Hirvonen, HE, Elima, KJ, Vuorio, EI: Co-expression of collagens II and XI and alternative splicing of exon 2 of collagen II in several developing human tissues. *Biochem J*, 294 (Pt 2): 595-602, 1993.
87. Kolpakova-Hart, E, Nicolae, C, Zhou, J, Olsen, BR: Col2-Cre recombinase is co-expressed with endogenous type II collagen in embryonic renal epithelium and drives development of polycystic kidney disease following inactivation of ciliary genes. *Matrix Biol*, 27: 505-512, 2008.
88. Rockich, BE, Hrycaj, SM, Shih, HP, Nagy, MS, Ferguson, MAH, Kopp, JL, Sander, M, Wellik, DM, Spence, JR: Sox9 plays multiple roles in the lung epithelium during branching morphogenesis. *Proceedings of the National Academy of Sciences*: 201311847, 2013.
89. Chen, Z, Migeon, T, Verpont, M-C, Zaidan, M, Sado, Y, Kerjaschki, D, Ronco, P, Plaisier, E: HANAC syndrome Col4a1 mutation causes neonate glomerular hyperpermeability and adult glomerulocystic kidney disease. *J Am Soc Nephrol*, 27: 1042-1054, 2016.
90. Abrahamson, DR, St John, PL, Stroganova, L, Zelenchuk, A, Steenhard, BM: Laminin and type IV collagen isoform substitutions occur in temporally and spatially distinct patterns in developing kidney glomerular basement membranes. *J Histochem Cytochem*, 61: 706-718, 2013.
91. Murata, T, Katayama, K, Ohashi, T, Jahnukainen, T, Yonezawa, T, Sado, Y, Ishikawa, E, Nomura, S, Tryggvason, K, Ito, M: COL4A6 is dispensable for autosomal recessive Alport syndrome. *Sci Rep*, 6: 29450, 2016.
92. Hsu, H-H, Murasawa, Y, Qi, P, Nishimura, Y, Wang, P-C: Type V collagen fibrils in mouse metanephroi. *Biochemical and Biophysical Research Communications*, 441: 649-654, 2013.
93. Tonelotto, V, Trapani, V, Bretaude, S, Heumüller, SE, Wagener, R, Ruggiero, F, Bonaldo, P: Spatio-temporal expression and distribution of collagen VI during zebrafish development. *Scientific Reports*, 9: 19851, 2019.
94. Kuo, HJ, Maslen, CL, Keene, DR, Glanville, RW: Type VI collagen anchors endothelial basement membranes by interacting with type IV collagen. *J Biol Chem*, 272: 26522-26529, 1997.
95. Gara, SK, Grumati, P, Squarzone, S, Sabatelli, P, Urciuolo, A, Bonaldo, P, Paulsson, M, Wagener, R: Differential and restricted expression of novel collagen VI chains in mouse. *Matrix Biol*, 30: 248-257, 2011.
96. Dupuis, LE, Nelson, EL, Hozik, B, Porto, SC, Rogers-DeCotes, A, Fosang, A, Kern, CB: Adamts5^{-/-} Mice Exhibit Altered Aggrecan Proteolytic Profiles That Correlate With Ascending Aortic Anomalies. *Arteriosclerosis, Thrombosis, and Vascular Biology*, 39: 2067-2081, 2019.
97. Rochette, A, Boufaied, N, Scarlata, E, Hamel, L, Brimo, F, Whitaker, HC, Ramos-Montoya, A, Neal, DE, Dragomir, A, Aprikian, A, Chevalier, S, Thomson, AA: Asporin is a stromally expressed marker associated with prostate cancer progression. *British Journal of Cancer*, 116: 775-784, 2017.
98. Schaefer, L, Grone, HJ, Raslik, I, Robenek, H, Ugorcakova, J, Budny, S, Schaefer, RM, Kresse, H: Small proteoglycans of normal adult human kidney: distinct expression patterns of decorin, biglycan, fibromodulin, and lumican. *Kidney Int*, 58: 1557-1568, 2000.
99. Fetting, JL, Guay, JA, Karolak, MJ, Iozzo, RV, Adams, DC, Maridas, DE, Brown, AC, Oxburgh, L: FOXD1 promotes nephron progenitor differentiation by repressing decorin in the embryonic kidney. *Development*, 141: 17-27, 2014.
100. Sonntag, M, Blosa, M, Schmidt, S, Reimann, K, Blum, K, Eckrich, T, Seeger, G, Hecker, D, Schick, B, Arendt, T, Engel, J, Morawski, M: Synaptic coupling of inner ear sensory cells is controlled by brevican-based extracellular matrix baskets resembling perineuronal nets. *BMC Biol*, 16: 99, 2018.
101. van den Born, J, van den Heuvel, LP, Bakker, MA, Veerkamp, JH, Assmann, KJ, Berden, JH: Monoclonal antibodies against the protein core and glycosaminoglycan side chain of glomerular basement membrane heparan sulfate proteoglycan: characterization and immunohistological application in human tissues. *J Histochem Cytochem*, 42: 89-102, 1994.
102. Jazbutyte, V, Fiedler, J, Kneitz, S, Galuppo, P, Just, A, Holzmann, A, Bauersachs, J, Thum, T: MicroRNA-22 increases senescence and activates cardiac fibroblasts in the aging heart. *AGE*, 35: 747-762, 2013.

103. Bengtsson, E, Mörgelin, M, Sasaki, T, Timpl, R, Heinegård, D, Aspberg, A: The leucine-rich repeat protein PRELP binds perlecan and collagens and may function as a basement membrane anchor. *J Biol Chem*, 277: 15061-15068, 2002.
104. Bode-Lesniewska, B, Dours-Zimmermann, MT, Odermatt, BF, Briner, J, Heitz, PU, Zimmermann, DR: Distribution of the large aggregating proteoglycan versican in adult human tissues. *J Histochem Cytochem*, 44: 303-312, 1996.
105. Chiotaki, R, Petrou, P, Giakoumaki, E, Pavlakis, E, Sitaru, C, Chalepakis, G: Spatiotemporal distribution of Fras1/Frem proteins during mouse embryonic development. *Gene Expr Patterns*, 7: 381-388, 2007.